Evaluation of Cellulose Nanocrystals as a Green "Smart Water" Additive in Enhanced Oil Recovery from Sandstone Reservoirs

Doctoral Thesis by

Silje Nedland Molnes

Thesis submitted in partial fulfilment of
the requirements for degree of
PHILOSOPHIAE DOCTOR
(Ph.D.)

FACULTY OF SCIENCE AND TECHNOLOGY

DEPARTMENT OF PETROLEUM ENGINEERING

2017

University of Stavanger
N-4036 Stavanger
NORWAY
www.uis.no

ISBN: 978-82-7644-715-6

ISSN: 1890-1387

PhD: Thesis UiS no. 348

Preface

This thesis is submitted in partial fulfilment of the requirements for the degree of Philosophiae Doctor (Ph.D.) at the University of Stavanger (UiS) and consists of three papers. The work presented in this thesis was mainly performed at the Ugelstad Laboratory at the Department of Chemical Engineering, NTNU, at the Smart Water Laboratory facility at the Department of Petroleum Engineering, UiS, and at the NTNU NanoLab/NorFab facility. The project has been fully funded through the NORCEL Project (The NORwegian NanoCELlulose Technology Platform), initiated and led by The Paper and Fibre Research Institute (PFI) in Trondheim and funded by the Research Council of Norway through the NANO2021 Program, grant number 228147. The work has been supervised by Associate Professor Dr. Skule Strand (UiS), and co-supervised by Associate Professor Dr. Kristofer G. Paso (NTNU) and Professor II/Senior Research Scientist Dr. Kristin Syverud (NTNU/PFI).

I completed my Master of Science in Biotechnology with a specialisation in biochemistry and biopolymer chemistry at the Department of Biotechnology at NTNU in June 2013. I was accepted as a Ph.D. candidate at the Department of Petroleum Engineering, UiS in April 2014.

Acknowledgements

Writing a Ph. D. is a daunting task, and I could not have pulled through without the guidance, help and support from a large and diverse group of people over the last three years.

First and foremost, I would like to express my thanks and gratitude to my supervisors, especially Associate Professor Skule Strand (Ph.D), and Senior Research Scientist, Kristin Syverud (Dr.Ing), for their thorough guidance and assistance throughout this project. Thanks should also be extended to Associate Professor Kristofer G. Paso (Ph.D.) for always being available for counselling.

Second, I would like to thank colleagues, staff and friends from the Smart Water group at UiS, The Ugelstad Laboratory at NTNU, and PFI, for general guidance and help in the lab, and for interesting discussions over coffees and beers over the years. Particularly, I would like to mention the assistance I got from Ivan D. P. Torrijos and Aleksandr Mamonov when performing the core flooding experiments at UiS. I could not have done it without your help and patience.

The Research Council of Norway should also be thanked for the full financial support of the NORCEL initiative, through the NANO2021 project. I also owe my thanks to PFI and Kristin Syverud for initiating NORCEL and taking me in on the project as one of three Ph. D. students

I would like to thank my friends and family in Trondheim, Moss, Ålesund and Stavanger for always believing in me, although it has not always been clear to you what I actually do. Specifically I would like to thank my parents, Tonje N. Molnes and Tore L. Molnes for letting me have my old room back and allowing me to live at home in Stavanger for extended periods of time, as well as their unlimited support and love. I want to thank my brothers, Torje and Sindre J. Molnes for their cheerful support, and my grandfather Christian Nedland for always being genuinely interested in hearing about my work, and for inspiring conversations over the years.

Last, but not at all least, I want to thank my fiancée Sigurd Rolland Pettersen for his unconditional love, patience and support. You keep my feet on the ground and my head out of the skies, and it means the world to me. I love you.

Abstract

Petroleum reservoir production is frequently supported by using flooding fluids, and offshore this fluid will very often be seawater. The efficiency of this water injection is affected by various factors, such as the wettability of the reservoir rock and the mobility ratio between reservoir oil and injected fluid phase. These factors again influence sweep efficiency, which is the fraction of the total reservoir oil volume in contact with injected fluid during oil recovery. Addition of nanoparticles can affect the sweep efficiency on both a macroscopic and microscopic level by increasing the volume of petroleum in contact with the flooding fluid, and divert the flow of water to lesser flooded parts of the reservoir.

In this thesis work, cellulose nanocrystals (CNC) have been investigated as a potential green additive alternative for enhanced oil recovery (EOR), in combination with the Smart Water low saline brine technology. Presented in this thesis are studies investigating the effects of different physical and chemical environments that low concentration CNC dispersions may be subjected to at oil reservoir conditions. First, various concentrations of CNC dispersed in de-ionized water and in a 1000 ppm NaCl brine were subjected to variations in salinity, pH and temperature, and the results confirmed that the dispersions remained stable within the salinities known to affect the wettability of sandstone, as well as the pH range expected in sandstone oil reservoirs. Stable dispersions were also observed when heated to temperatures ranging from 50 to 90 °C. At extended heat aging at 90 °C and 120 °C for seven days, beginning degradation was observed for both types of CNC dispersions, with viscosity increase and pH decrease as the most important indicators. CNC dispersed in 1000 ppm NaCl brine was generally more heat tolerant than the CNC dispersed in de-ionized water. A fluid that increases its viscosity with heat and time will be easier to inject due to a low initial viscosity, and when the viscosity increases in the porous reservoir, this effect could lead to increased sweep efficiency and better oil recovery.

The injectivity of CNC into a high-permeable sandstone core has been investigated by performing flooding experiments on 100 % water saturated cores, using increasing concentrations of CNC and increasing temperature.

These investigations confirmed that most of the viscosity generating CNC particles travelled through the cores at all the tested temperatures and CNC concentrations. Oil recovery experiments showed that when CNC-LS brine was used in tertiary mode, an increase in ultimate recovery was observed. During tertiary CNC-LS injection, the CNC particles increased fluctuations in differential pressure, which could be linked to log jamming in pore throats and remobilisation of oil in the pore space. These results indicate that CNC particles may have potential as a green flooding fluid additive, but that further investigations are needed.

List of publications

I. Silje Nedland Molnes, Iván D. Piñerez Torrijos, Kristofer G. Paso, Skule Strand, Kristin Syverud. ***"Sandstone injectivity and salt stability of cellulose nanocrystals (CNC) dispersions – Premises for use of CNC in enhanced oil recovery",*** *Industrial Crops and Products, 2016. Vol. 93, 152 – 160.*

II. Silje Nedland Molnes, Kristofer G. Paso, Skule Strand, Kristin Syverud. ***"The effects of pH, time and temperature on the stability and viscosity of cellulose nanocrystal (CNC) dispersions – Implications for use in enhanced oil recovery"***, *Submitted to Cellulose, 03.02.2017.*

III. Silje Nedland Molnes, Aleksandr Mamonov, Kristofer G. Paso, Skule Strand, Kristin Syverud. ***"Investigation of a new application for cellulose nanocrystals – A study of the enhanced oil recovery potential from sandstone by use of a green additive"***, *Submitted to Cellulose, 21.03.2017.*

Poster and conference contributions

Poster at 249th ACS National Meeting and Exposition – Chemistry of Natural Resources

Title: *Sandstone Core-flooding using Low-Saline Water and Crystalline Nanocellulose.*
Authors: Silje Nedland Molnes, Ivan D. Piñerez Torrijos, Kristofer G. Paso, Skule Strand, Kristin Syverud.
Date: 22 – 26th March, 2015
Location: Denver, CO, USA

Talk at TAPPI Nano's 2016 International Conference on Nanotechnology for Renewable Materials

Title: *Sandstone Injectivity of Cellulose Nanocrystals - A Premise for use in Enhanced Oil Recovery.*
Comment: 20 minute talk
Authors: Silje Nedland Molnes, Ivan D. Piñerez Torrijos, Kristofer G. Paso, Skule Strand, Kristin Syverud.
Date: 13 – 16th June, 2016
Location: Grenoble, France

Talk at PFI's 6th Research Seminar: Recent advances in cellulose nanotechnology research – Production, characterization and applications

Title: *Sandstone Injectivity of Cellulose Nanocrystals - A Premise for use in Enhanced Oil Recovery.*
Comment: 10 minute talk
Authors: Silje Nedland Molnes, Ivan D. Piñerez Torrijos, Kristofer G. Paso, Skule Strand, Kristin Syverud.
Date: 19 – 20th October, 2016
Location: Trondheim, Norway

Contents

List of figures

List of tables

Abbreviations and nomenclature

$1/\kappa$	Debye length
AFM	Atomic force microscopy
AGU	Anhydroglucose unit
AN	Acid number
BN	Base number
CBR	Crude oil-brine-rock (system)
CEC	Cation exchange capacity
CMC	carboxymethyl cellulose
CNC	Cellulose nanocrystals
CNC-DI	CNC dispersed in DI water
CNC-LS	CNC dispersed in LS brine
CNF	Cellulose nanofibrils
d_5FW	Formation water diluted 5 times
DI	De-ionised (water)
DP	Degree of polymerisation
E	Global displacement efficiency
E	Strength of the electric field
E_D	Microscopic displacement efficiency
EDL	Electrical double layer
EOR	Enhanced oil recovery
ε	Dielectric constant
ε_0	Permittivity of free space
ε_r	Dielectric constant of dispersing medium
η	Viscosity
E_V	Macroscopic (volumetric) displacement efficiency
φ	Porosity
φ_c	Minimum overlap concentration
FPL	Forest Products Laboratory
FW	Formation water
g	Gravitational acceleration constant
g_c	Conversion factor
H	Height of column
HCl	Hydrochloric acid
HEC	Hydroxyethyl cellulose
HPAM	Hydrolysed polyacrylamide
HP-β-CD	hydroxypropyl-β-cyclodextrin
H_2SO_4	Sulphuric acid
I_{AH}	Amott-Harvey index

IFT	Interfacial tension
I_o	Oil wetting indice
I_w	Water wetting indice
IOR	Improved oil recovery
J	Surface curvature
k	Permeability
k_{rw}	Relative permeability of water
L	Length of capillary tube
LDV	Laser Doppler velocimetry
λ_D	Mobility of displacing fluid
λ_d	Mobility of displaced fluid
LPG	Liquid petroleum gas
LS	Low salinity (brine), 1000 ppm NaCl
LSE	Low salinity effect
M	Mobility ratio
mM	Milli-molar
mΩ	Milli-Ohm
MIE	Multi-component ion exchange
meq	Milli-equivalents
μ	Viscosity
μ_E	Electrophoretic mobility
μM	Micro-molar
μS	Micro-Sievert
mS	Milli-Sievert
NaCMC	Sodium carboxymethyl cellulose
NaOH	Sodium hydroxide
N_c	Capillary number
NOK	Norwegian kroner
NPD	Norwegian Petroleum Directorate
OED	Olje- og Energidepartementet
OOIP	Original oil in place
ORD	Oxidative/reductive depolymerisation
OSPAR	Oslo-Paris Commission
ΔP	Pressure difference
Pa	Pascal
PAC	Polyanionic cellulose
PANI	Polyaniline
P_b	Bubble point pressure
P_c	Capillary pressure
P_{res}	Reservoir pressure
Π	Disjoining pressure

PLONOR	(Chemical) posing little or no risk (to the environment)
ppb	Parts per billion
ppm	Parts per million
PV	Pore volume
r	Pore radius
RO	Reverse osmosis
ρ	Density
σ	Interfacial tension
ΔS_{ws}	Change in water saturation, spontaneous imbibition
ΔS_{wf}	Change in water saturation, forced imbibition
ΔS_{os}	Change in oil saturation, spontaneous imbibition
ΔS_{of}	Change in oil saturation, forced imbibition
SDS	Sodium dodecyl sulphate
S_{oi}	Initial oil saturation
S_{or}	Residual oil saturation
S_{wi}	Initial water saturation
S_{wr}	Irreducible water saturation
TDS	Total dissolved solids
TGA	Thermogravimetric analysis
TOC	Total organic content
θ	Contact angle
v	Velocity
VDW	van der Waals (forces)
wt. %	Weight percent
ζ	Zeta potential
Å	Angstrom

1 Motivation and Outline

The average oil recovery from mature oilfields around the world seldom reach above 40 % of the original oil in place (OOIP), thus leading to at least 60 % of the oil remaining in the reservoirs after conventional oil recovery methods are spent. Even with the situation the world is currently going through, with relatively low oil prices, an oil recovery increase of only a few percent of OOIP would mean that it could be economically viable to employ enhanced oil recovery technology instead of developing new oilfields. Many of the unexplored fields remaining today are located in remote and/or environmentally vulnerable areas, making it more demanding, expensive, and maybe ethically questionable to perform exploration and test-drilling (Muggeridge et al., 2014). The Åm committee was appointed by the Norwegian Ministry of Petroleum and Energy (OED), and in 2010 they concluded that an increase in oil recovery of only 1 % from the Norwegian Shelf was worth 270 billion NOK (Åm et al., 2010). Seven years later, this sum is probably smaller due to the decline in oil prices, but still a considerable amount of money.

Developing and applying economically viable and environmentally friendly enhanced oil recovery (EOR) methods is therefore of crucial importance. The effect of implementing low salinity flooding brines in oil recovery has been known for almost 20 years, and in this thesis work, the aim was to combine low salinity flooding with a new potential biopolymer nanoparticle additive, namely cellulose nanocrystals (CNC). Due to its renewable source material and the absence of dangerous breakdown products makes CNC a safe and green alternative to existing technologies.

The thesis work has been divided into two separate parts; characterization of the cellulosic material under physical conditions that is encountered in oil reservoirs; and core flooding studies, where first the injectivity of brines containing CNC was studied to determine suitable polymer concentrations and temperature performance, and at last enhanced oil recovery tests; all at laboratory scale.

2 Introduction to Nanocellulose

2.1 Cellulose

Cellulose is a polymeric biomaterial, and it is the most abundant material produced by the biosphere, with 1.5 x 10^{12} tons of estimated annual production (Klemm et al., 2005). Cellulose-based materials have been in use as engineering materials for thousands of years, and still are today, with a huge market and industries for forest products and their derivatives. Today, the largest consumer of cellulose is the paper and cardboard industry (Dufresne, 2013a). In 1838, Anselme Payen first used the term "cellulose", and he established through purification of plant tissue that the fibrous content of plant cells has a unique chemical structure (Payen, 1838). In 1913, Willstätter and Zechmeister established the basic cellulose formula (Willstätter & Zechmeister, 1913).

Cellulose is found in the protective cell walls of plants, bacteria, fungi and certain animals (tunicates), and is an important element for maintaining their structural integrity. It is composed of D-glucopyranose rings linked together through β-1,4 glycosidic bonds. Adjacent rings are arranged in such a way so the glucosidic oxygens points in opposite directions, and the repeating unit of cellulose is named cellobiose, as indicated in Figure 2.1.

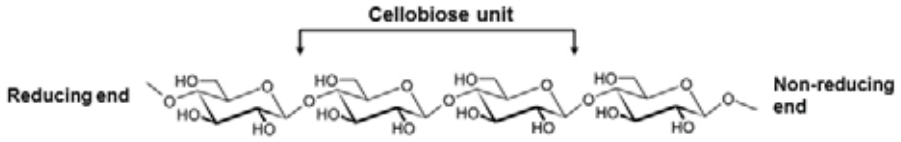

Figure 2.1: The chemical structure of cellulose.

The cellobiose units covalently link to form a linear homopolymer consisting of between 2000 and 27000 residues, and the degree of polymerization (DP) depends on the cellulose source, with wood cellulose having a DP of approximately 10000 glucopyranose units (Sjöström, 1981). As glucose units

are 0.515 nm (5.15 Å) long, stretched glucose chains may be between 1 and 14 µm. Each cellulose monomer has three hydroxyl groups, which governs crystalline packing and other characteristic properties of the material through their hydrogen bonding abilities. This forms a network of intra- and intermolecular hydrogen bonds. A network of van der Waals connections are also created between the chain layers (French et al., 1993), and together these allow the formation of crystalline structures. This is the base for cellulose nanofibrils (CNF), whose crystallinity, width, length and shape vary with source, although they almost always have a high aspect ratio. Due to confinement during biosynthesis, the crystalline structure of nanofibrils is distorted at given intervals, producing non-crystalline amorphous regions on the fibrils. In most plant fibres, the CNF is found in the middle layer of the secondary cell wall (S2), as shown in Figure 2.2 (Dufresne, 2013a).

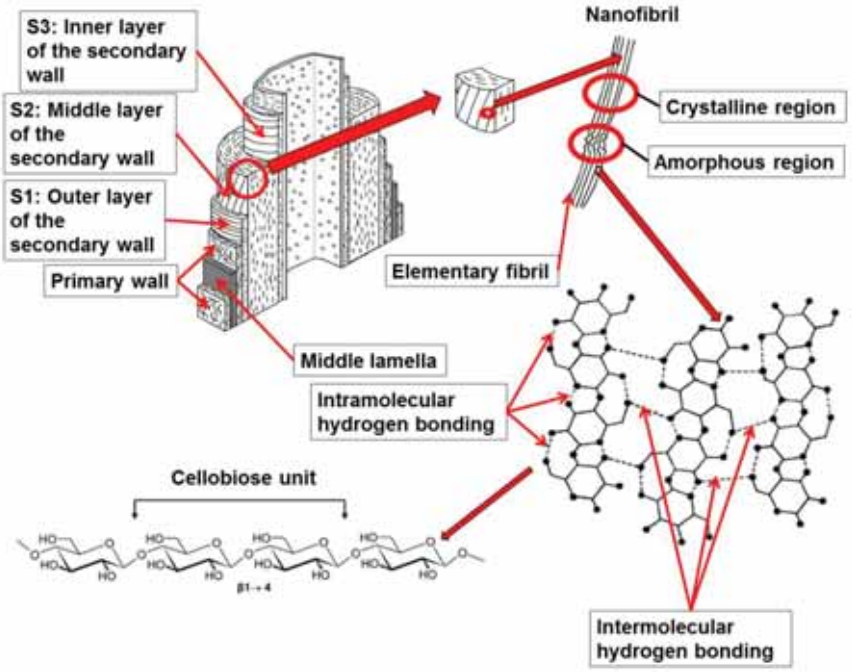

Figure 2.2: Schematic structure of cellulose, from plant cell walls to single cellulose chains, consisting of repeating cellobiose units. Adapted from (Tsuchikawa, 2007).

2.2 Cellulose nanocrystals (CNC)

Cellulose nanocrystals (CNC) is a sub-entity of cellulose fibres and are produced "top-down" through acid hydrolysis of the cellulose, where the amorphous regions of the fibres are dissolved.

2.2.1 Background

As mentioned, preparation of CNC is not a synthesis, but a "top-down" process where fibrous cellulose material is split up into crystalline entities. This phenomenon was first observed by Nickerson and Habrle, when boiling of cellulose fibres in acidic solution led to a degradation limit after a certain time of hydrolysis treatment (Nickerson & Habrle, 1947). This work inspired Rånby and his co-workers at the University of Uppsala to investigate the preparation of stable colloidal suspensions of, among others, wood cellulose, through controlled hydrolysis with sulphuric acid. An example of an aqueous CNC dispersion is shown in Figure 2.3.

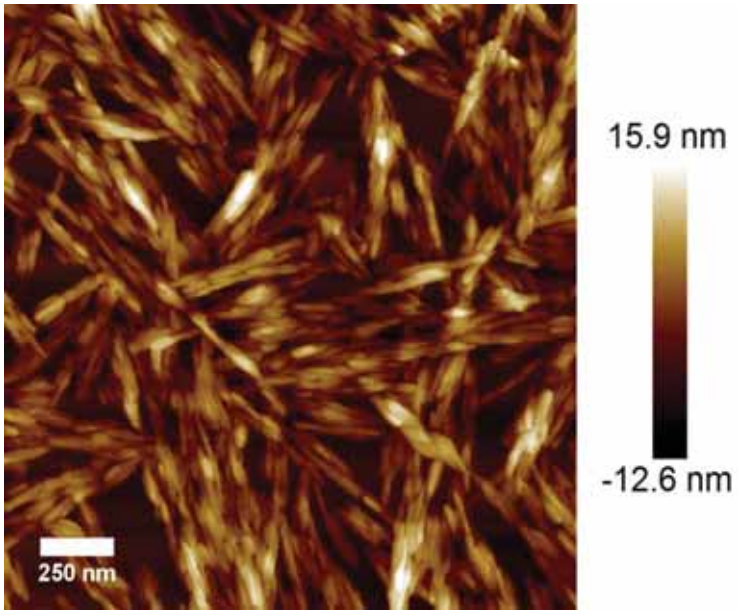

Figure 2.3: CNC in aqueous dispersion pictured with atomic force microscopy (AFM).

Rånby suggested that "micellar strings" (crystalline regions) were the building blocks of wood and cotton cellulose, and that these could exist in a free form or in aggregates, and have a constant width of ~7 nm. These building blocks could be set free by ultrasonic (mechanical) treatment, and hydrolysis would cut these strings into "micelles", or short fragments (Rånby, 1949, 1951, 1952).

2.2.2 Production

Since the 1950s, the production of wood CNC has become relatively standardised. The fibres are usually hydrolysed using either sulphuric acid (H_2SO_4) or hydrochloric acid (HCl), which produces crystallites with slightly different properties. Since the cellulose must be directly hydrolysed, a few pre-treatment steps are necessary. The general procedure is given in Figure 2.4.

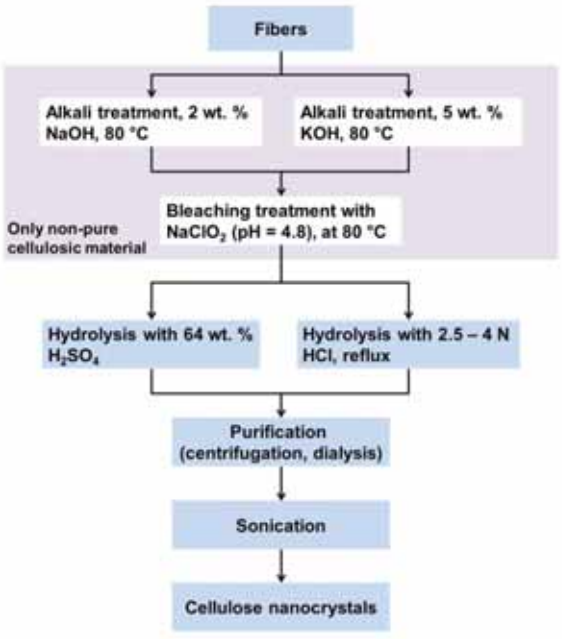

Figure 2.4: General production procedure for CNC. Adapted from (Dufresne, 2013b).

First, if the mass is untreated, the biomass is dewaxed by using toluene and ethanol, or benzene and ethanol (2:1). Then follows an alkali extraction, and after that a bleaching step. The alkali treatment is performed to solubilise the pectins and hemicelluloses in the material, and the bleaching step removes residual phenolic compounds like lignin (polyphenols) and proteins. This extraction method has been relatively standardised since the 1940s (Wise et al., 1946). The extraction and bleaching processes may be repeated several times, and filtration and washing with distilled water is performed between each step. If the starting biomass is bleached from the producer, this step can be omitted.

The next step is to hydrolyse the amorphous domains of the fibres. These regions are randomly organised and have a lower density compared to the nanocrystalline parts (Brown Jr & Saxena, 2000; de Souza Lima & Borsali, 2004). A number of different strong acids have been proposed, and shown to degrade cellulose fibres, but H_2SO_4 and HCl have been most extensively used. Sulphuric acid hydrolysis is the most studied method, and also seems to be the most effective. One of the main reasons for this is the dispersability properties of the finished product. Cellulose hydrolysed using HCl tends to flocculate in aqueous dispersion and is generally unstable. Sulphuric acid hydrolysis introduces anionic sulphate half-esters ($-OSO_3^-$) randomly distributed on the crystalline surface through an esterification reaction of the hydroxyl groups, as shown in Figure 2.5. The amount of half ester groups grafted onto the surfaces, as well as the crystallite length can be tuned by varying reaction time and temperature (Beck-Candanedo et al., 2005; X. Dong et al., 1998). The lengths of CNC produced from plant celluloses is usually in the range of 100 – 250 nm, with widths from 5 – 70 nm (Klemm et al., 2011).

These negatively charged surface groups create an electrostatic double layer (EDL) around the particle, which promotes its dispersability in water. The electrostatic repulsions between the EDLs of individual particles are the main causes of the dispersion stability of sulphuric acid hydrolysed CNC (Dufresne, 2013b).

2.2.3 Colloidal behaviour of cellulose nanocrystals

When dispersed in DI-water, cellulose nanocrystals form colloidal dispersions. For a dispersion to be termed "colloidal", the dispersed particles must have a size range between 1 nm and 1 μm. The stability of such dispersions depends on a number of different parameters; particle dimension, size polydispersity and the surface charge. Cellulose nanocrystals produced using sulphuric acid will be stable in an aqueous dispersion, due to the negatively charged half ester sulphate groups created on the surface during the hydrolysis step (Figure 2.5). These causes an EDL to form around the particles and thus the particles are electrostatically stabilised (Araki et al., 1998).

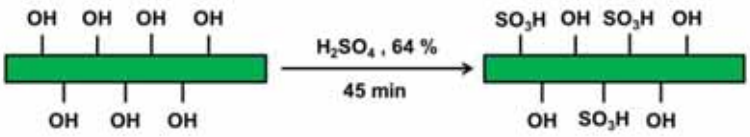

Figure 2.5: Schematic of acid hydrolysis of CNC (not to scale).

Being rod-like particles, cellulose nanocrystals exhibit a tendency to align along a directing vector. As native cellulose has a strong birefringence, the rod-alignment of cellulose nanocrystals produces a macroscopic birefringence that can be observed by the use of crossed polarisers. This effect was first reported by Marchessault et al. in 1959. When dispersed in low concentrations, CNC particles are randomly oriented and form an isotropic phase. When the particle concentration is increased above a critical concentration (4.5 wt. %, according to (X. Dong et al., 1998)), the dispersion separates into two phases, one isotropic and one anisotropic, as shown in Figure 2.6. The latter is characterised by the self-orientation of the CNC particles in the same direction along a directing vector, which results in a nematic liquid crystalline alignment. The chiral nematic pitch, P, is the distance it takes for the crystalline particles to take a full 360° twist. In Figure 2.6, this is given as P/2, indicating that the crystallites are only twisting 180°. P can be tuned by altering the temperature of the dispersion or by adding other molecules, like salts. When the pitch is in the same order as the wavelength of

visible light, it can reflect polarised light (de Vries, 1951; Kopp et al., 1998). If the concentration is further increased, the dispersion reaches a critical concentration, where the CNC may form a chiral nematic ordered phase, which will display typical cholesteric liquid crystal optical properties (X. M. Dong et al., 1996; Marchessault et al., 1961; Marchessault et al., 1959; Revol et al., 1992; Revol et al., 1994).

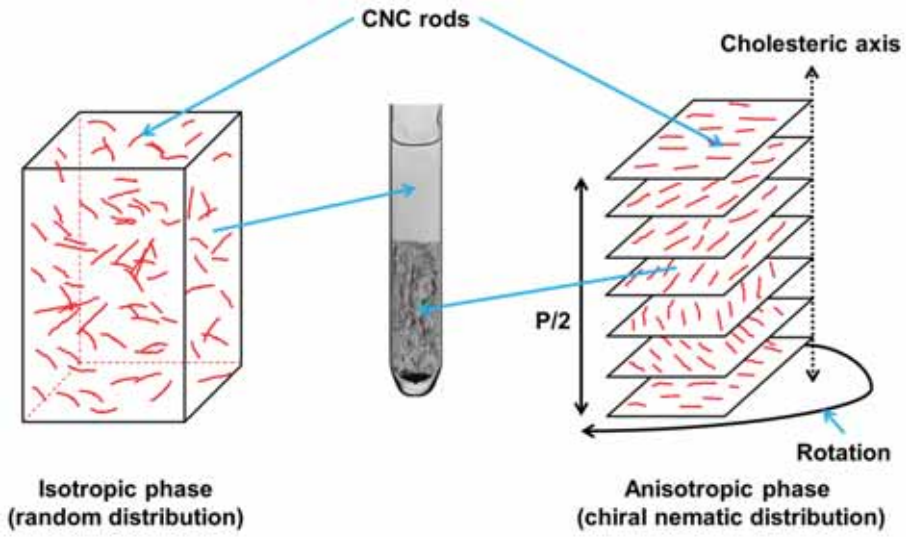

Figure 2.6: Illustration of a biphasic dispersion of CNC in water, as it would look through crossed polarisers. The isotropic phase is shown on the left and anisotropic phase is shown on the right. Photograph of biphasic CNC dispersion from (X. Dong et al., 1998).

The colloidal stability of charged nanoparticles like CNC in dispersion is mainly governed by the zeta potential (ζ) (Leong & Ong, 2003; S. C. Wang & Wei, 2001). It is affiliated with the distribution of charged entities in the bilayer that surrounds the particle, and controls the electrokinetic properties of dispersed particles (Sarkar & Nicholson, 1996; Will et al., 2001). When a charged particle is dispersed in a medium with high dielectric constant, an EDL will form around it. If there is shear or movement in the dispersion, a slipping plane will form between the stationary layer around the particle and the diffuse layer/bulk medium, as indicated in Figure 2.7. The counter-ions in the stationary layer are associated with the particle surface and moves with the

particle, while the free counterions in the diffuse layer/bulk medium do not. The electrokinetic potential thus formed in the slipping plane is known as the zeta potential, normally given in mV. A high zeta potential, either negative positive, indicates a strong electrostatic repulsion between the particles involved. Surface forces will be more thoroughly described in Chapter 4.2.

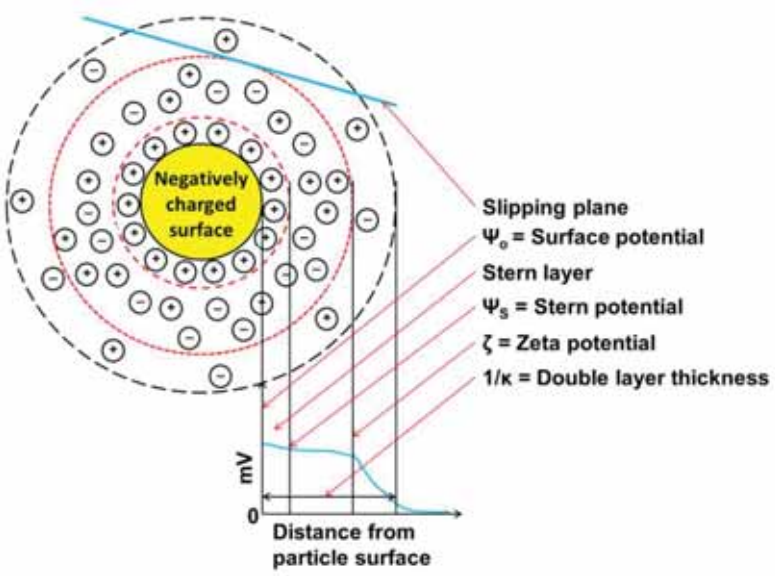

Figure 2.7: Graphic presentation of the electrical double layer of a negatively charged particle.

The repulsion inhibits agglomeration and settling of the dispersed particles, and leads to a stable dispersion. In Table 2.1 the colloidal stability of dispersions with increasing zeta potential is given (Hanaor et al., 2012; Hunter, 1981; Salopek et al., 1992).

Table 2.1: Colloidal stability of dispersions with increasing zeta potential. Adapted from (Salopek et al., 1992).

Zeta potential (mV)	Colloidal stability
0 to ± 5	Rapid flocculation/coagulation
± 5 to ± 30	Incipient stability
± 30 to ± 40	Moderate stability
± 40 to ± 60	Good stability
> ±60	Excellent stability

2.2.4 Rheology

The ability of CNC to form ordered liquid crystalline phases, makes it a good model system to study the rheological and ordering behaviour of long rigid rods. The particles are strongly influenced by shear rate, and in 1961, Marchessault demonstrated that the hydrodynamic properties of CNC are directly related to the size distribution of the crystallites in dispersion (Marchessault et al., 1961). CNC exhibits a shear dependent viscosity profile that can be split up into three distinct regions, which is a characteristic rheological behaviour for liquid crystalline polymers in dispersions (Onogi & Asada, 1980). A typical viscosity profile for CNC in dispersion is illustrated in Figure 2.8.

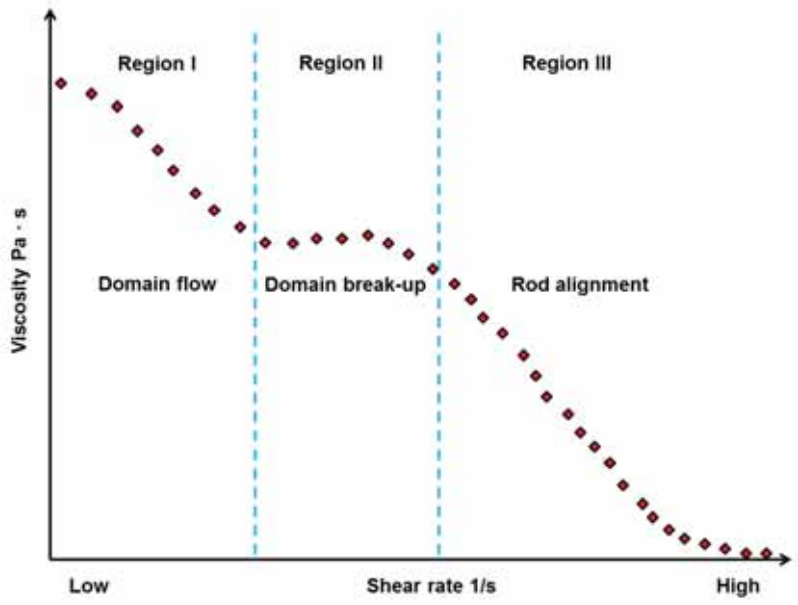

Figure 2.8: Shear rate dependency illustrated for a CNC dispersion. The different shear regions are indicated with blue dashed lines. Adapted from (Shafiei Sabet, 2013).

Region I appear at low shear rates, representing a constant decrease in viscosity, due to the material flowing in domains. In region II, these domains are starting to break up, and this forms a plateau in the flow curve, as

indicated in Figure 2.8. When approaching region III, with high shear rate, the dispersion is exhibiting a second shear thinning behaviour, due to the now individual rods aligning with the direction of flow. Thus, when the shear rate disrupts the chiral nematic phase of CNC nano-rods, they exhibit nematic ordering, with axes aligned parallel to the flow direction. Orts et al. (1998) studied this effect on CNC from black spruce bleached Kraft pulp, using small angle neutron scattering (SANS) (Orts et al., 1998). Similar results have been obtained for cotton linter CNC (de Souza Lima & Borsali, 2004).

The shear dynamics of a CNC dispersion will also be dependent on the concentration of dispersed CNC. Bercea and Navard (2000) divided this behaviour into two different regimes; isotropic-at-rest (0 – 0.85 wt. %, dilute and semi-dilute regimes) and anisotropic-at-rest (1 – 3.5 wt. %, concentrated regime). For the isotropic regime, the viscosity profile exhibited two plateaus. At low shear, the dispersion showed a true Newtonian viscosity, with rods in random orientation independent of the shear rate, and at high shear, the plateau indicated rods well oriented in a steady state fashion, and thus no change in viscosity was observed. The dispersions in the anisotropic regime (c > 1.0 wt. %) exhibited the same behaviour as observed in the Orts study (1998) and Lima & Borsali (2004), with a plateau region surrounded by two shear thinning regions as seen in Figure 2.8 (Bercea & Navard, 2000).

Electroviscous effects must also be taken into consideration when looking at shear dynamics of charged particles. These effects causes charged particles to have higher low-shear viscosity than non-charged particles (Russel, 1978; Wierenga & Philipse, 1997). Charged Brownian particles experience EDL deformation under shear (primary electroviscous effect), as well as overlapping of the double layers (secondary electroviscous effect), which contributes to the higher low-shear viscosity (Conway & Dobry-Duclaux, 1960; Hunter, 1981). When the ionic strength of the dispersing medium is increased, the contribution from the electroviscous effects is reduced. NaCl reduces the size of the EDL, and a smaller double layer leads to less distortion under shear and reduces overlapping and interactions between the particles, resulting in a lower viscosity (Boluk et al., 2011).

2.3 Cellulose products in the oil industry

The use of cellulose nanocrystals for oil related purposes is not a completely new idea. As they are derived from completely renewable sources (plants and trees), and do not produce any harmful degradation products, they are regarded as a green chemical according to the OSPAR Commission's (Oslo-Paris) PLONOR list (chemical posing little, or no risk to the environment) (OSPAR, 2016). Currently, no reports are found on CNC being applied in oilfields for recovery purposes, but investigations on laboratory scale are currently being performed, both using sandstone core flooding (Aadland et al., 2016; Molnes et al., 2016) and laser-etched glass models (Wei et al., 2016).

In the field, CNC is being used as a cement strengthener, by adding it to well fluids, and it has also been used as a viscosity modifier in water-based fluids intended for fracturing and gravel packing (Rae & Johnston, 1996; Rincon-Torres & Hall, 2015). The effect of replacing solid content in bentonite drilling fluids with CNC and/or CNF has also been explored, with an aim to improve cost efficiency, eco-friendliness and safety of such fluids. Addition of CNF/CNC to the bentonite-based drilling fluids improved both the rheological and filtration performance of the fluids (Song et al., 2016).

A selection of different cellulose derivatives have also been investigated and utilised for different petroleum industry related applications. Among these are polyanionic cellulose (PAC) (Mahto & Sharma, 2004) and sodium carboxymethyl cellulose (NaCMC) (Dolz et al., 2007), which were tested as a rheology modifier in drilling fluids. CMC has also been used to dope polyaniline (PANI) for use as a liquid petroleum gas (LPG) sensor with promising results (Ravikiran et al., 2014).

For oil recovery purposes, different hydrophobically and/or hydrophobically modified hydroxyethyl cellulose (HEC) varieties has been investigated (Wever et al., 2011). By varying the modification of the parent cellulosic structure, the rheological properties of the polymer dispersions can be tuned, for example by adding surfactants like sodium dodecyl sulphate (SDS) or hydroxypropyl-β-cyclodextrin (HP-β-CD) (Kjøniksen et al., 2008).

3 Basic Concepts of Oil Recovery

3.1 Introduction

Petroleum, or crude oil, is a mineral substance that is derived from decomposed organic matter that has been subjected to elevated temperature and pressure by Mother Nature for millions of years. It has a complex hydrocarbon mixture, with properties varying with composition, and it can exist in a gaseous, liquid or semi-liquid state. Components and physical characteristics of crude oil come in a wide variety, but the elemental composition is rather uniform, and is given in Table 3.1.

Table 3.1: Elemental composition of crude oil (Gary et al., 2007; Speight, 2014).

Element	Percentage (in wt. %)
Carbon (C)	84 – 87
Hydrogen (H)	11 – 14
Sulphur (S)	0 – 5
Nitrogen (N)	0 – 2
Oxygen (O)	0.05 – 1.50

Crude oils contain both acidic and basic components, which are quantified through their respective acid and base numbers (AN and BN, respectively). Both values are reported in mg KOH/g, and the AN indicates the amount of KOH (in mg) needed to neutralise the acidic components in 1 g of crude oil. For BN, mg KOH represents the equal amount of basic material that is present in 1 g of crude oil. Carboxylic groups (-COOH) is the main acidic component present in crude oil, and are mostly bound to large molecules in the heavy fractions of the hydrocarbons, like resins and asphaltenes. Nitrogen is part of most of the basic components in the form of aromatic molecules (R_3N). Usually, BN >> AN, due to carboxylic groups decomposing over geological time, especially at higher temperatures (S Strand et al., 2016).

Hydrocarbons are formed in sedimentary rocks which are rich in organic matter, like coals, shales or carbon-rich limestone, called *source rocks*. This rock type is able to release very large amounts of liquid and gaseous hydrocarbons. The origin of petroleum has been debated since the 1860s

(Speight, 2014), and many hypotheses have been presented over the years. The one that is currently in favour asserts that oil and gas is derived from the organic residues of marine phytoplankton as well as some foraminifera and algae (Skinner et al., 2013).

Phytoplankton and bacteria is the main organic matter in marine basins, buried in clay and mud in the seafloor. Here the sediments are slowly converted to shale due to the burial pressure, and the geothermal heat transforms the organic matter into *petroleum*. The temperature most favourable for hydrocarbon generation is called the *oil window*, and ranges from around 60 to 175 °C. Above this temperature gas formation is dominant, and if it becomes warmer than 225 °C, the petroleum generation capacity is lost (Selley & Morill, 1991). The chemical reactions that are involved in crude petroleum generation is called *maturation* (Zolotukhin & Ursin, 2000a).

There are two types of evidence that supports the hypothesis that crude oil is a product of decomposition of organic material, derived from living organisms: First, oil has the same optical properties as hydrocarbons that are known to originate from organic matter, and second, it contains nitrogen, as well as other compounds, like metalloporphyrin pigments, that can only be derived from organic matter (Ali et al., 1993; Skinner et al., 2013).

Maturated petroleum can only be accumulated if certain criteria are met, which is the unique combination of source rock and condition suitable to trap the produced hydrocarbons. Crude oil is less dense than water, and if released from the source rock into a neighbouring porous rock, the oil will migrate upwards until it reaches minimum pressure, either by escape through the ground surface, or meet a barrier, also called a *trap*. The hydrocarbons accumulate in the trap formation by expelling the pre-existing pore water from the pore matrix. This hydrocarbon-containing part of the trap is called a *petroleum reservoir*, and the hydraulically connected water-bearing part is called an *aquifer*, as indicated in Figure 3.1.

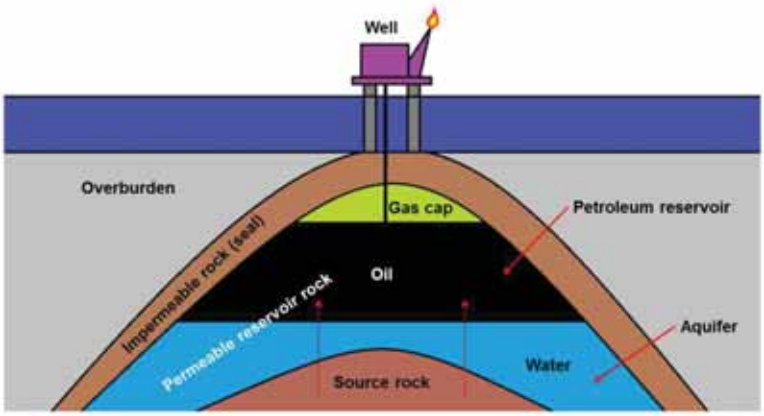

Figure 3.1: Typical anticlinal petroleum trap (simplified, not to scale). The oil migrates from the source rock through the permeable rock into the oil reservoir above the water line.

The oil reservoir rock must be sufficiently porous and permeable to allow the hydrocarbons to accumulate, and the porosity is usually between 5 and 30 % (Speight, 2014).

Petroleum traps exist in different forms, but they can be roughly divided into *structural traps* (tectonic structure of the rock) and *stratigraphic traps* (sealing effects by unconformities and rock type). The trap type illustrated in Figure 3.1 is an *anticlinal trap*, which is a tectonic structure that is formed by a localised uplift and/or folding of sedimentary rock. *Faults* (as shown in Figure 3.2) are stratigraphic traps, and are usually created through two different geological mechanisms; *clay smear*, where clay is smeared onto the fault plane, due to shear forces during movement, which provides a seal; or *juxtaposition*, where the faulting has caused an impermeable rock to be juxtaposed against the reservoir rock (Jahn et al., 2008c).

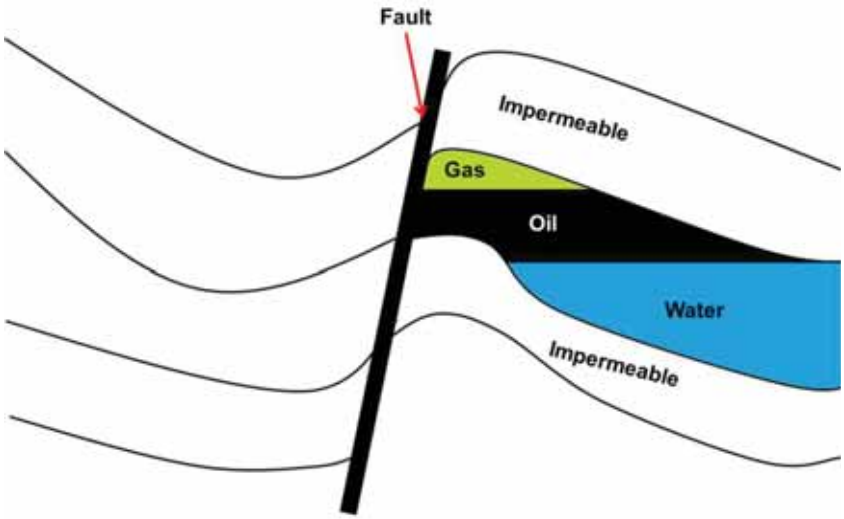

Figure 3.2: Hydrocarbon accumulation due to a fault structure.

Faults and domes/anticlines are the two most typical forms of traps on the Norwegian Continental Shelf (*Petroleum Resources: Norwegian Continental Shelf*, 1993; Zolotukhin & Ursin, 2000a).

3.2 Mineralogical description of sandstones

The mineralogy of an oil reservoir is of great importance when it comes to wetting properties and other parameters which may have implications for the oil recovery process. The main focus of this thesis work is oil recovery from sandstones, and here follows a short review of the most important aspects of sandstone mineralogy.

Sandstones are *sedimentary* rocks, and are formed through *lithification* ("turned into rock") due to deposition of *clastic* material (Gr. "klastos" = "broken") or *detritus* (Lat., "worn down"). Clastics and detritus is the result of weathering, fragmentation and erosion of older rock types. Some of the clastics may be *bioclastics*, meaning they are derived from shells or skeletal parts of dead organisms. Sediments are transported, via water (rivers, sea currents), wind (in deserts) and ice (glaciers). The type of transport determines the energy available for component movement, and governs the size, shape and sorting of sediment grains. Sorting is a very important aspect

of reservoir quality, as it controls parameters such as *porosity* and *permeability*, which is illustrated for porosity in Figure 3.3 (Jahn et al., 2008c; Zolotukhin & Ursin, 2000a).

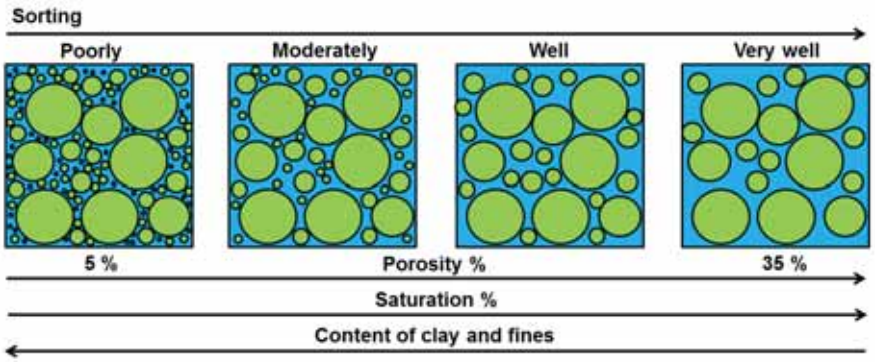

Figure 3.3: Sorting impact on reservoir porosity. Adapted from (Jahn et al., 2008c).

Sediments deposited on land surface or seabed, is buried, compressed and cemented through a chemical process called *diagenesis*, over geological time (Zolotukhin & Ursin, 2000a).

According to the Udden-Wentworth scale, the clast sizes for sandstones vary from 63 μm to 2 mm (Udden, 1914; Wentworth, 1922). Sandstones and conglomerates constitute 20 – 25 % of sedimentary rocks.

A large number of different minerals can occur in sandstones, but the most common are quartz, feldspars, micas and clay minerals. A common characteristic of these is that they all are stable under surface conditions (Nichols, 2009).

3.2.1 Quartz

Quartz is the chemically simplest of the silicate minerals, with formula SiO_2, and is the most common mineral species found in sandstones, contributing from 60 – 70 %. The cause of this prevalence is its high resistance to weathering and other disintegrating mechanisms, having a hardness of 7 on *Mohs' scale*. It is common in rock types such as granite, gneiss and schist. Sandstone is broadly divided into arenites and wacke, according to the Dott

classification diagram (Dott Jr, 1964), which displays the relative proportions of clasts and matrix (silt and clay material). If the amount of matrix is < 15 %, the rock is classified as an *arenite*, and if the matrix content is between 15 – 75 %, it is called a *wacke*. These rock types also have several sub-classifications, according to the presence of other mineral grains (Nichols, 2009; Pettijohn et al., 1987).

3.2.2 Micas

Micas are *phyllosilicates* and are relatively abundant in sandstone as detrital grains, and are derived from igneous, metamorphic and sedimentary rock formations. The two most common forms are white mica, *muscovite*, and the brown mica, *biotite*. They have a distinctive, platy shape, and have a tendency to be concentrated in bands on bedding planes (Nichols, 2009; Pettijohn, 1975).

3.2.3 Feldspars

Feldspar is a large silicate mineral component of igneous rocks, and is thus released in large quantities when rock types such as granites is broken down. It is softer than quartz and hence more susceptible to degradation and chemical alteration during transport and other processes. Its base components are silicon and oxygen, but calcium, sodium and potassium may also be present, and the type of feldspar is controlled by the relative amount of these ions. They are the main initial minerals species in clay formation through a hydration process, for which the chemistry is based on cation exchange mechanisms, as described in Equation 3.1 (Velde & Meunier, 2008).

$$\text{feldspar} + \text{hydrogen ions} \rightarrow \text{clay} + \text{cations, solids, water} \qquad (3.1)$$

Feldspar usually constitutes between 10 – 15 % of the sandstone, and is thus less prevalent than quartz, due to their higher susceptibility to weathering and degradation. There are two main families of feldspars, with potash feldspars (microcline) being the most prevalent, due to a higher resistance to degradation mechanisms. Potash feldspars ($KAlSi_3O_8$) consist of orthoclase, which is very common in grains of sedimentary rocks, and the slightly less

common microcline; while the plagioclase feldspars are albite ($NaAlSi_3O_8$), and anorthite ($CaAl_2Si_2O_8$) (Crundwell, 2015; Nichols, 2009).

3.2.4 Clays

Clay minerals are usually a product of the breakdown of silicate minerals like feldspars, and can be described chemically as aluminium silicates. They are similar to micas, with a layered, crystalline structure, and are essentially composed of silica, alumina and water. They frequently contain large quantities of magnesium and iron, as well as lesser amounts of sodium and potassium. There are two patterns of layering occurring in clays found in sandstone reservoirs, and these consist of two building units; the first one is tetrahedral silica sheets, and the second on is layers of octahedral aluminium. The building units are linked together in planar layers, by sharing oxygen ions between Si^{4+} and Al^{3+} ions, and the first type of layering has two layers, and is called the *kandite group*, while the second layering type has three layers, and is called the *smectite group*. Although the Si^{4+} and Al^{3+} ions are the main occupants of the space between the tetrahedral and octahedral layers, other cations will also be present to ensure charge balance (Nichols, 2009; Worden & Morad, 2003). The four most common clay minerals occurring in sedimentary rocks are given in Figure 3.4 (Tucker, 2013).

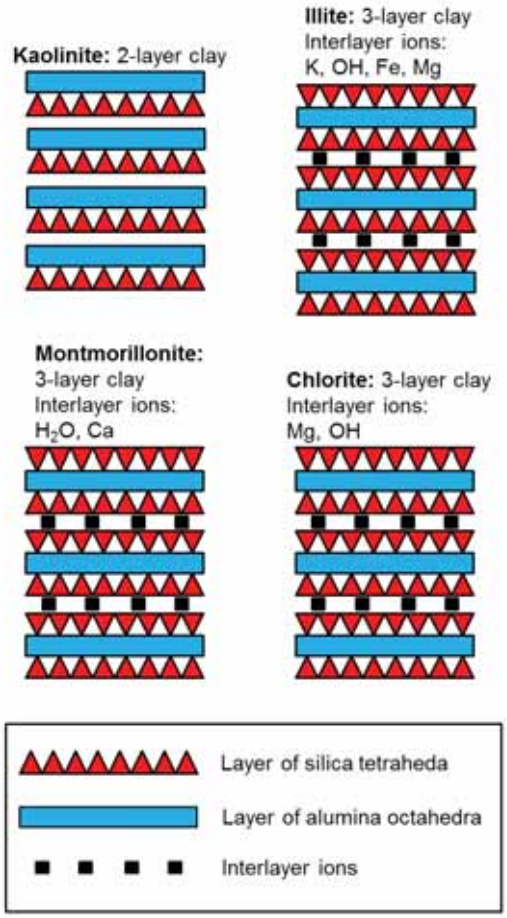

Figure 3.4: Crystal lattice structures for the most common clay minerals. Adapted from (Nichols, 2009).

Kaolinite is the most common member of the kandite group, and has the chemical formula $Al_2Si_2O_5(OH)_4$. It is comprised of one tetrahedral layer linked to on octahedral layer through O-H-O bonds, and thus termed a 1:1 layer structure. Kaolinite is described as booklet pages resistant to chemical treatment, and is generally formed from granite bedrock lithologies leached by acidic waters. *Montmorillonite* is a clay mineral in the smectite group and is known as a swelling clay, due to its ability to absorb water within its structure. It is a 2:1 clay, which means it has one octahedral sheet sandwiched

between two tetrahedral sheets. *Illite* is also a 3-layer smectic clay rich in potassium. As montmorillonite, it is a 2:1 structure and thus comprised of one octahedral layer between two tetrahedral layers, where opposing tetrahedral layers are bound together with O-K-O bonds. This is a very strong bond, and prevents the clay mineral from swelling. *Chlorite* has a 2:1:1 structure, which consists of a 2:1 layer (tetrahedral-octahedral-tetrahedral) which is negatively charged, and interlayered with a positively charged octahedral layer with cations and hydroxyl ions (Nichols, 2009; Worden & Morad, 2003).

Clay materials have one very characteristic property, which distinguishes them from other silicate materials, and this is the occurrence of negative charges that are located at the edges/ends of the unit cells. These charges may cause the substitution of cations, or interactions with the surrounding media to stabilise the charges. This situation depends on the pH conditions, and these groups are therefore named variable charges. Permanent charges depend on cation substitution within the layers, but both charge types contribute to the cation exchange capacity (CEC) of a clay mineral (Velde & Meunier, 2008).

CEC is a measure of a clay mineral's ability to attract and bind cations from the surrounding medium and is denominated milli-equivalents (meq) per 100 g of sample. It is defined as the quantity of exchangeable cations that the clay can hold at a given pH (usually pH 7) (Bergaya et al., 2006). Cations can be organised in series, based on how strong their replacing power is, but the definite position is governed by the type of clay and the size of the ion that is replaced. The degree of attraction for different cations towards clay materials is shown below (Yong et al., 2012),

$$Li^{+} < Na^{+} < K^{+} < Mg^{2+} < Ca^{2+} < Sr^{2+} < Ba^{2+} < Cu^{2+} < H^{+}$$

This series of replacing power thus implies that when equal concentrations of Na^{+} and Ca^{+} exists, the Ca^{+} cations will be better at displacing Na^{+} from the clay surface than Na^{+} will be at displacing Ca^{+}. If the concentration of a low replacing power cation is high enough, relative to the concentration of the higher replacing power cation, the high replacing power cation may be displaced (RezaeiDoust, 2011).

The key properties of the most common clay minerals are collected in Table 3.2.

Table 3.2: Properties of the most common clay minerals (*Technical Manual for Drilling, Completion and Workover Fluids*, 1982) .

Property	Kaolinite	Illite	Chlorite	Montmorillonite
Structure	1:1	2:1	2:1:1	2:1
Particle size (µm)	0.5 – 5	Large sheets up to 0.5	0.1 – 5	0.1 – 2
CEC (meq/100 g)	3 – 15	10 – 40	10 – 40	80 – 150
Surface area BET (m^2/g)	15 – 25	50 – 110	140	30 – 80

3.3 Oil recovery mechanisms

The life of an oil reservoir consists of several phases. First and foremost, access is gained after thoroughly evaluation of technical, economic, political, social and environmental aspects of the considered region. The follows the *exploration* phase, where oil and gas is sought after by geologists and geophysicists, for example by the use of seismic surveys both on- and offshore. This process may last for years. Then follows the *evaluation* phase, where the potential oilfield is more thoroughly investigated through the drilling of test wells, and a decision is taken whether to develop the field or not. In the *development* phase, the complete production is planned, a field development plan (FDP) is drawn up, and plants, facilities and infrastructure are built. At last, the *production* can begin, and this phase can last for 10 – 40 years, sometimes even longer, depending on the oilfield. The timeline consists of a build-up period, a plateau period and a decline period (which is usually the longest one. This is the phase where the oil recovery takes place, and is usually divided into three main stages; primary, secondary and tertiary oil recovery; given a conventional oil reservoir. Depending on the characteristics of the oil reservoir, the order of these processes can be altered, and also skipped (Green & Willhite, 1998a). Figure 3.5 shows an overview of typical application sequence of the different oil recovery phases. An oil field is

decommissioned when the net economical income is lower than the operation costs (Jahn et al., 2008b; Wintershall, 2017).

3.3.1 Primary recovery

Primary oil recovery concerns the part of the oil production where no external force is added to the production process (like fluid injection). Thus the only reason hydrocarbons are produced is a natural reduction in pressure in the reservoir. There are different natural driving mechanisms, and the general performance of an oil reservoir is determined by what kind of energy that produces the oil. Basically, these driving mechanisms can be divided into six different types (Ahmed, 2010b; Ahmed & McKinney, 2005):

Rock and liquid expansion drive: This situation occurs when the pressure in the reservoir exceeds the bubble point, and the oil reservoir is *undersaturated*. When the pressure in the reservoir is reduced, the rock and fluids (connate water and crude oil) will expand, with the crude oil expansion being the main driving force, as it is typically 10 times larger than the water/brine expansion.

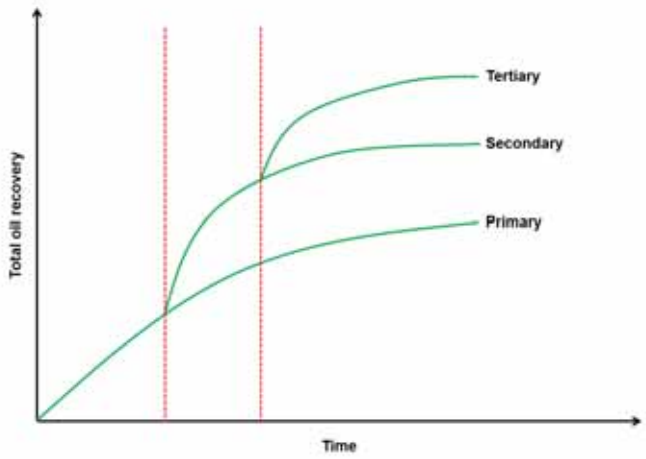

Figure 3.5: Oil recovery mechanism sequence. Adapted from (Ahmed, 2010c).

Solution gas (depletion) drive: Natural production by solution gas drive is caused by gas liberation from the crude oil when the reservoir pressure is

reduced below the bubble-point pressure. Gas bubbles will be liberated into the microscopic pore spaces and expand, and in this way force the oil out of the pore spaces.

Gas-cap drive: Reservoirs with gas-caps generally show slow decline in reservoir pressure, due to the gas cap's ability to expand. The available forces to produce oil in gas cap drive are expansion of the gas-cap gas and liberated solution gas.

Water drive: Regardless of water source, this natural drive effect is caused by water migrating into the pore spaces of the oil, displacing it.

Gravity drainage: This mechanism occurs as a result of the different densities of the reservoir fluids.

Combination drive: The most common natural drive mechanism, where both water and gas are available to displace oil towards the wells. Two types of combination driving forces are usually present in this type of reservoir: 1) Solution gas drive and weak water drive, or 2) Solution gas drive with small gas-cap and weak water drive.

The total oil recovery from primary recovery mechanisms is usually in the range of 5 – 40 % OOIP, but for certain exceptional reservoirs the ultimate recovery may reach 75 % OOIP (water drive) and 80 % OOIP (gravity drainage) (Ahmed & McKinney, 2005).

3.3.2 Secondary recovery

The term secondary oil recovery refers to the processes that are started when the natural driving forces (primary oil recovery) are not sufficient; and the most common methods are water and gas injection (Ahmed, 2010c). These methods are applied to displace crude oil towards the production wells and maintain the pressure in the reservoir (Green & Willhite, 1998a). Oil production under secondary recovery can be up to 70 % OOIP at very good oil reservoir conditions, but due to unfavourable reservoir conditions (reservoir heterogeneity), like fractures, permeability differences, adverse wettability conditions and capillary entrapment, the average oil recovery in

secondary mode is usually in the range of 20 – 40 % OOIP (Green & Willhite, 1998a; Muggeridge et al., 2014).

3.3.3 Tertiary recovery – Enhanced oil recovery

Tertiary, or enhanced oil recovery (EOR) is a term that comprises all the methods that are put to use to recover the residual oil (S_{or}) that is left after primary and secondary oil recovery methods are spent. EOR processes n involves the injection of agents that are not normally present in an oil reservoir, like a fluid or gas, with and without added heat. The injected agents will interact with the oil-rock system, and can cause several different effects, among others: Lower the interfacial tension (IFT), oil viscosity reduction, wettability alteration or increase the oil mobility (Bavière, 1991; Green & Willhite, 1998a). All EOR methods have a common target of increasing the volumetric (macroscopic) sweep efficiency and improving the displacement (microscopic) efficiency. The volumetric sweep is increased by reducing the mobility ratio between the displacing and the displaced fluid, while the microscopic entrapment could be lowered when the interfacial tension (IFT) between the displacing and displaced fluids is reduced. This gives a lower S_{or} and thus a higher ultimate oil recovery (Zolotukhin & Ursin, 2000b).

EOR can be looked upon as a subset of improved oil recovery (IOR), which implies increasing the recovered amount of oil by any means, including secondary recovery (water-flooding, gas injection), infill drilling, conformance control or horizontal wells (Stosur et al.; Thomas, 2008).

3.3.4 General description and characterisation of EOR processes

A large number of different EOR methods have been employed over the years, with a varying degree of success. EOR methods can be utilised for most crude oil qualities, be it light crude, heavy crude or tar sands. The EOR technique applied must match the reservoir geology and fluid properties it is supposed to recover. A general overview of different EOR methods is given in Figure 3.6, and as can be seen, they are roughly divided into two groups; thermal methods and non-thermal methods; with several subset categories.

Thermal methods have been utilised and developed since the 1950s, and are thus the most advanced and field applied methods. They work best for recovery of crudes with a low API gravity value, like heavy crude oils (10 – 20° API) and tar sands (≤ 10° API). API (American Petroleum Institute) is a dimensionless (given in degrees) value measuring how heavy an oil product is relative to water; when it is higher than 10, it is lighter than and will float on water, and below 10 it will sink (Ernest et al., 1959). Thermal methods supply heat to the reservoir, and thus lead to crude oil viscosity decrease, and further a better mobility ratio. Other effects present can be compaction, rock and fluid expansion, and steam distillation (Thomas, 2008).

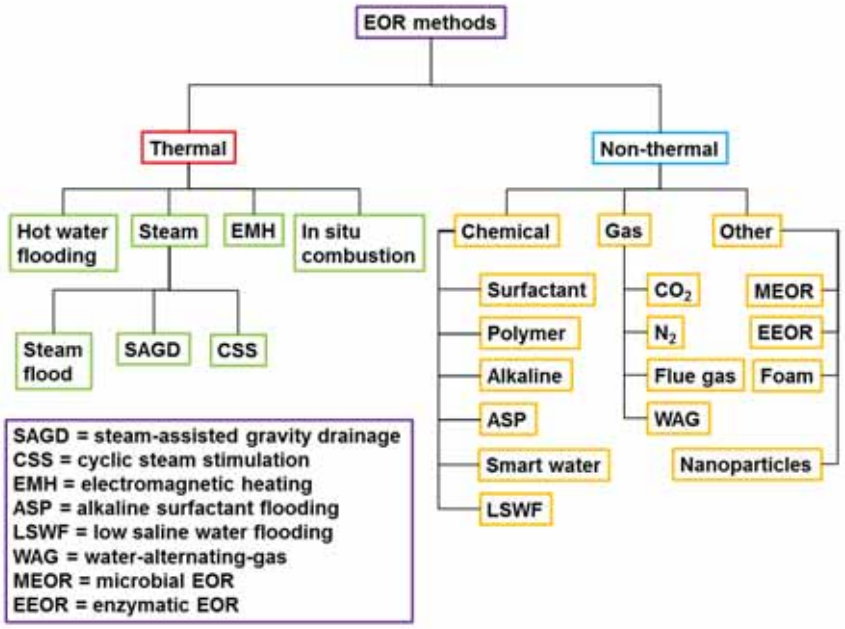

Figure 3.6: Schematic classification of EOR methods. Adapted from (Thomas, 2008).

Non-thermal methods are better suited for lighter crude oils, which have relatively low viscosities and thus higher API values (> 20° API) (Speight, 2014). The two main objectives for non-thermal techniques are 1) Lowering the IFT, and 2) improve the mobility ratio (Thomas, 2008). A third approach

is to change the reservoir wettability, a method that is aiming to desorb crude oil from the pore surfaces of the oil reservoir (N. R. Morrow, 1990).

Based on studies on cationic surfactants in carbonate rocks, Standnes et al. was able to develop a new method for changing the wetting properties in reservoir rock, only by modifying the chemical composition of the flooding fluid. The result was named "Smart Water", and the method comprises wettability alteration without lowering the capillary forces significantly, which may increase oil production. The composition of the flooding fluid can be tailored after reservoir and crude oil properties, and the method is economically viable, as preparation is simple and no expensive chemicals needs to be added (Tor Austad, 2013; Standnes & Austad, 2003; Skule Strand et al., 2003). This is very advantageous, as many EOR methods are limited by their high application costs. Smart Water may also have potential in combination with other flooding agents/methods, especially in sandstone formations.

4 Fundamentals of Porous Systems, Surface and Colloid Chemistry

Water, oil and gas flooding inside a porous material will be subject to several different forces, the most important ones being capillary forces, viscous forces and gravity forces. The wetting properties and surface forces must also be taken into consideration when planning a waterflood. In this section, these main factors will be described in relation to EOR using SmartWater.

4.1 Displacement forces

During an EOR process, the overall displacement can be described on both the microscopic and the macroscopic scale. At the microscopic scale, wettability of the porous material, the viscosity of its fluids and interfacial tension will be very important parameters to assess when applying a certain EOR method. All these parameters control the residual oil saturation (S_{or}) after a waterflood. At macroscale, reservoir heterogeneity, conformance control or gravity forces may have an impact on the recovery efficiency. The following sections will describe these parameters.

4.1.1 Displacement efficiency

The oil recovery from any displacement process is dependent on the reservoir volume that is in contact with the injected fluid. The volumetric displacement (sweep) efficiency (E_V) is a quantitative measure of this contact. It can also be termed macroscopic efficiency and is defined as the reservoir fraction pore volume (PV) in contact with the fluid injected. E_V in a displacement process is thus a function of time (Green & Willhite, 1998c).

The overall or global displacement efficiency (E) in any oil displacement from the reservoir is defined as the product of the macroscopic and the microscopic displacement efficiencies, and is given in Equation 4.1,

$$E = E_D E_V \tag{4.1}$$

Where E is the global displacement efficiency, E_D the microscopic displacement efficiency and E_V is the macroscopic, or volumetric, displacement efficiency. To obtain an as high as possible global displacement efficiency, it is important that the product of E_D and E_V approaches 1. An ideal displacing fluid would therefore remove the oil from all contacted pores ($S_{or} \rightarrow 0$) and be in contact with the total reservoir volume.

Microscopic displacement (E_D) efficiency is related to mobilisation of oil at the pore scale, and thus depends on how efficient the displacing fluid is at mobilisation of the oil it contacts in the porous rock. The magnitude of the residual oil saturation (S_{or}) in the regions flooded by the displacing fluid reflects the E_D. The macroscopic displacement efficiency (E_V), or sweep efficiency, is related to how effective the displacing fluid is in sweeping the reservoir, both from an area and vertical point of view. How fast the displacing fluid moves the mobilised oil towards the wellbore is also taken into consideration.

All EOR processes have a common goal of minimalizing the S_{or} value by increasing the efficiency of the microscopic displacement. How efficient E_D is controlled by the physical and chemical interactions that occur when a displacing fluid in injected into a porous media, the most common ones being interfacial tension, wettability alteration and oil volume expansion. If these parameters are taken well into consideration when preparing the displacing fluid, the S_{or}-values will be lower, causing a large E_D, as described in Equation 4.2:

$$E_D = \frac{S_{oi} - S_{or}}{S_{oi}} \tag{4.3}$$

Where

S_{oi} Initial oil saturation
S_{or} Residual oil saturation

The E_V on the other hand, is affected by features on a larger scale, like reservoir structure, density differences and viscosity ratios, and there are several parameters that can have an adverse effect on the sweep efficiency of a displacing fluid. Such restrictions may be unfavourable reservoir geology,

large density differences and poor mobility ratios, leading to viscous fingering effects, and under- or overriding of the displacing fluid, and thus a low E_V (Green & Willhite, 1998b).

4.1.2 Fluid flow in porous media

The fluid flow through porous media is a key parameter in oil recovery. Darcy's law (Darcy, 1856) is a mathematical relationship applicable to non-fractured reservoirs, and it describes the mobility of a fluid phase flowing in a porous medium. The Darcy equation relates the viscosity of a displacing fluid, its flow rate through porous media and the pressure drop the fluid creates over a given distance, and is given in Equation 4.4:

$$u = -A\frac{k}{\mu}\frac{dP}{dx} \tag{4.4}$$

Where

u	Superficial (Darcy) velocity of the displacing fluid (m^3/s)
k	The effective permeability of the displacing fluid (D)
μ	Viscosity of the displacing fluid (cp)
P	Pressure (atm)
x	Length (cm)
A	Cross-sectional area of the filter medium perpendicular to flow (cm^2)

The minus sign only indicates that the pressure decreases in the direction of flow, giving a *negative* pressure gradient in the x-direction. Normally the absolute value of ΔP is used in calculations, giving the flow rate a non-negative value.

The permeability, k, in the Darcy equation is a *proportionality coefficient*, and does not present a readily quantifiable characteristic of the porous medium, but rather its bulk physical characteristics, which controls its fluid transmission capacity. A definition of permeability as a physical unit can be derived by the rearrangement of Equation 4.4:

$$k = \frac{\mu\Delta x}{A}\frac{u}{\Delta P} \tag{4.5}$$

Equation 4.5 implies that one unit permeability equals the permeability of a given porous medium with 1 cm length, and 1 cm^2 cross-sectional area that is able to transmit a fluid with a viscosity of 1 cp, at a differential pressure of 1 atm, and a flow rate of 1 cm^3/s. The permeability of such a porous unit is called 1 D (Darcy) (Zolotukhin & Ursin, 2000c).

In a displacement process, where two phases co-exist, the mobility ratio, *M*, is given by the relationship between the mobility of the *displacing* fluid phase (λ_D), and the mobility of the *displaced* fluid phase (λ_d). The mobility of a fluid is given in Equation 4.6, and the mobility ratio is shown in Equation 4.7:

$$\lambda = \frac{k}{\mu} \tag{4.6}$$

Where k is the permeability of the porous medium and μ is the viscosity of the fluid.

$$M = \frac{\lambda_D}{\lambda_d} \tag{4.7}$$

M is a dimensionless quantity, and a very important parameter in all displacement processes, including reservoir water-flooding. It affects both areal and vertical sweep efficiency, where increasing *M* means a decrease in sweep efficiency. The mobility ratio also affects the displacement process stability, with unstable flow resulting in viscous fingering at $M > 1.0$. Thus an *M* value > 1.0 is deemed unfavourable mobility ratio, while a value < 1.0 is favourable. For a waterflood with oil as the displaced fluid, where one can assume a piston-like flow (only water flowing behind the front and only oil flowing ahead), Equation 4.7 can be extended to

$$M = \frac{\lambda_D}{\lambda_d} = \frac{\lambda_w}{\lambda_o} = \frac{\left(\frac{k_{rw}}{\mu_w}\right)_{S_{or}}}{\left(\frac{k_{ro}}{\mu_o}\right)_{S_{wi}}} \tag{4.8}$$

Where

λ_w Mobility of water (D/cp)
λ_o Mobility of oil (D/cp)
k_{rw} Relative permeability of water (D)
μ_w Water viscosity (cp)
k_{ro} Relative permeability of oil (D)
μ_o Oil viscosity (cp)
S_{or} Residual oil saturation
S_{wi} Irreducible water saturation

The relative permeabilities k_{rw} and k_{ro} are measured at residual oil saturation and irreducible water saturation, respectively (Green & Willhite, 1998c).

4.1.3 Capillary forces

Phase trapping and mobilisation of fluid in a porous media is governed by capillary forces. These again are dependent on the interplay of surface/interfacial tension (IFT) between rock and fluids, geometry and size of pore throats, and the wettability properties of the system. Capillary pressure (P_c) is defined as the pressure difference at the curvature between two immiscible fluids. P_c is formed due to the interfacial tension between the immiscible fluids and is dependent on the curvature of the interface (Ahmed, 2010a; Green & Willhite, 1998d). The interface will always be convex towards the wetting fluid, because its internal pressure will be higher. The relationship between the pressure difference, $\Delta p = P_c$ and the curvature of the interface is given by the Laplace equation:

$$P_c = \sigma\left(\frac{1}{R_1} - \frac{1}{R_2}\right) \tag{4.9}$$

Where

σ Interfacial tension (N/m)
R_1, R_2 Radii of the interface curvature (m)

If the meniscus is hemispherical, or if the system in question is a spherical oil droplet equal to the pore size, $R_1 = R_2 = r$ and $\Delta p = 2\sigma/r$. For a planar interface (no meniscus) the relationship will be $R_1 = R_2 = \infty$ and $\Delta p = 0$.

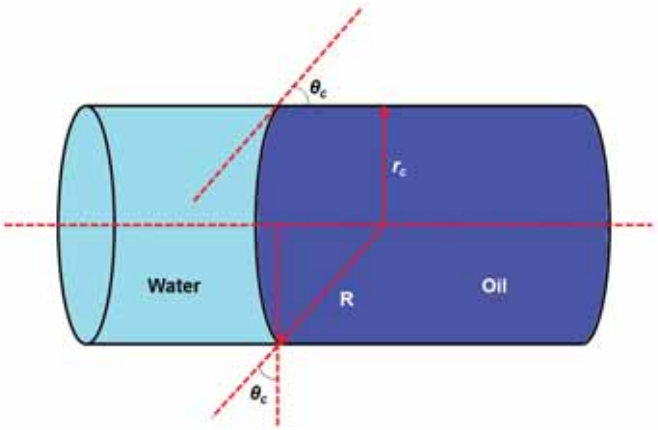

Figure 4.1: Simplified and idealised model of a pore channel containing a water phase and an oil phase, with a meniscal interface. R is the curvature radius, r_c is the capillary radius and θ_c is the wetting angle. Adapted from (Zolotukhin & Ursin, 2000d).

If two immiscible liquids (like water and oil) are confined in a capillary tube or a pipe with a capillary radius r_c, as shown in Figure 4.1, the pressure difference across the meniscal interface can be written from Equation 4.9:

$$p_o - p_w = \sigma_{ow}\left(\frac{1}{R_1} - \frac{1}{R_2}\right) \tag{4.10}$$

The principal radii of the interface curvature are averaged as R, θ_c is the wetting angle and r_c is the radius of the capillary tube. When $R_1 = R_2 = R$, and R can be written as Equation 4.11:

$$R = \frac{r_c}{\cos\theta_c} \tag{4.11}$$

The expression for the capillary pressure can be given as:

$$P_c = p_o - p_w = \sigma_{ow}\left(\frac{1}{R_1} - \frac{1}{R_2}\right) = \frac{2\sigma_{ow}\cos\theta_c}{r_c} \tag{4.12}$$

Where

p_o	Pressure in the oil phase at interface (Pa)
p_w	Pressure in the water phase at interface (Pa)
σ_{ow}	Interfacial tension at o/w interface (N/m)
θ_c	Contact angle between the phases (°)
r_c	Pore radius of capillary (m)

Capillary forces can, depending on the type of system, act for or against oil production. In a fractured, or heterogeneous reservoir, they can improve the oil recovery efficiency due to spontaneous imbibition, while in a homogeneous reservoir (like most sandstone reservoirs) strong capillary forces lead to trapping of oil and high S_{or} (Anderson, 1987; Zolotukhin & Ursin, 2000d).

4.1.4 Gravity forces

Gravity forces are important in oil recovery processes, as gravity segregation will occur when there are large density differences between the displacing fluid ρ_D and the displaced fluid ρ_d. If this difference is large enough, a significant fluid flow in the vertical direction may be induced, even when the main direction of the fluid flow is in the horizontal plane. This may have an impact on the vertical sweep efficiency, due gravitational over- or underride. When the displacing fluid is less dense than the displaced fluid, gravity segregation causes override. Gravity segregation also occurs when the injected fluid is denser than the displaced fluid, as can be the case in water-flooding, and the result is underride of the displaced fluid, as shown in Figure 4.2. Gravity segregation can lead to early breakthrough of the injected fluid and thus lead to decreased vertical sweep efficiency (Green & Willhite, 1998c).

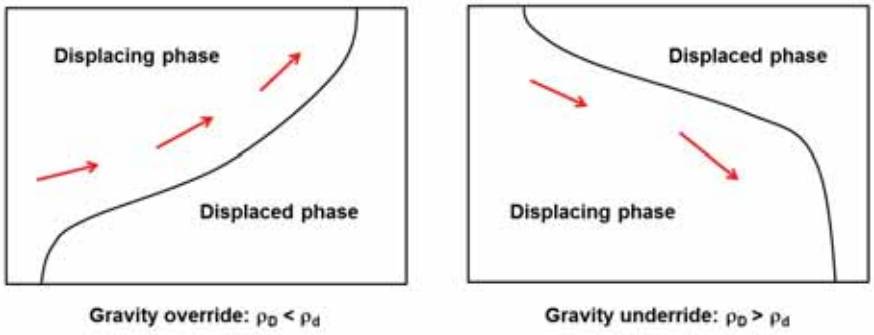

Figure 4.2: Gravity segregation in displacement processes. Adapted from (Green & Willhite, 1998c).

Conditions with low oil/water interfacial tension may also lead to gravity segregation (T Austad & Milter, 1997). Due to the fluids' immiscibility, the less dense fluid phase will always be subject to a buoyancy force, as described in Equation 4.13:

$$\Delta P_g = \Delta \rho g H \tag{4.13}$$

Where

ΔP_g Pressure difference over the o/w interface due to gravity (Pa)
$\Delta \rho$ Density difference for the two phases (kg/m^3)
g The gravitational acceleration constant (9.81 m/s^2)
H Column height (m)

4.1.5 Viscous forces

The viscous forces of a porous medium is revealed as the size of the pressure drop that results from fluid flow through the material, and the viscous force must be higher than the capillary force for the fluid to flow through a given pore throat. If the porous medium is regarded as a bundle of parallel capillary tubes, the pressure drop for laminar flow through a single tube is given by Poiseuille's law (Green & Willhite, 1998d):

$$\Delta P = -\frac{8\mu L\bar{v}}{r^2 g_c} \tag{4.14}$$

Where

ΔP	Difference in pressure over capillary tube (Pa)
μ	Viscosity (Pa·s)
L	Capillary length (m)
$\bar{v}$	Average flow velocity in the capillary (m/s)
r	Radius of the capillary (m)
g_c	Conversion factor

4.1.6 Interrelation of forces

Capillary forces acting within porous networks cause entrapment of one fluid phase by another during displacement processes. The trapped fluid phase, e.g. the oil can be recovered if the viscous forces acting on the system exceeds the capillary forces trapping the oil (Chatzis & Morrow, 1984). After a water-flood where the porous system in question is water-wet, the oil will exist primarily as a discontinuous phase of droplets at S_{or}, due to trapping and isolation of droplets by the displacing fluid. The fluid distribution at S_{or} will be different if the system is oil-wet. At this point in the water-flood, the displacing fluid will have entered a sufficient number of pore throats to stop the oil flow. The result of this is that the remaining oil will exist as a film around the sand grains, and in smaller pore throats it may occupy the void space completely. If the residual oil saturation in a water-wet system is to be mobilised, it is required that the discontinued oil spheres are connected to form a flow channel. If the system is oil-wet, the oil film around the sand grains must be displaced to pore-throats and connected into a continuous before mobilisation. Mobilisation of oil is controlled by the pressure gradient (viscous forces) and the forces of interfacial tension existing in the sand-oil-water system. Several studies on the effects of viscous and interfacial tension forces on trapping and mobilisation of residual oil has been performed, and thus revealed a correlation between the dimensionless parameter named the *capillary number*, N_c, and the fraction of recovered oil. N_c is the ratio of viscous forces to interfacial tension forces, and is given in Equation 4.15:

$$N_c = \frac{v_o \mu_w}{\sigma_{ow}} = \frac{K_0 \Delta P}{\varphi \sigma_{ow} L} \tag{4.15}$$

Where

v	Darcy velocity (m/s)
μ_w	Viscosity of the displacing fluid (Pa·s)
σ_{ow}	Displaced/displacing fluid interfacial tension (N/m)
K_0	Effective permeability of displaced phase (D)
φ	Porosity (%)
$\Delta P/L$	Pressure drop associated with Darcy velocity (Pa/m)

$N_c > 10^{-5}$ is necessary for mobilization of unconnected oil droplets. The capillary number will increase when the viscous forces increase or the interfacial forces decrease (Terry, 2001).

4.2 Surface forces

In order to understand the mechanisms behind wettability, it is important to first gain some insight in the forces at work between charged surfaces in aqueous dispersions. There are four types of forces that are considered to operate between particles or surfaces in liquids:

1. Monotonically attractive van der Waals forces, that occur between all molecules
2. Repulsive "double layer forces", that are of electrostatic origin, due to ionisable surfaces with a net electric charge
3. Solvation forces, that arises due to structuring or ordering of liquid molecules that are tightly confined between two surfaces, and can be attractive, repulsive or oscillatory.
4. Repulsive entropic forces, that are caused either by thermal motions of protruding surface groups (steric forces; polymers etc.), or by thermal fluctuations of flexible, fluid-like surfaces (fluctuation forces; lipid bilayers etc.)

In liquids, all these forces operate simultaneously, and it can be difficult to identify their separate contributions to a dispersion system (Israelachvili &

McGuiggan, 1988). In the next two sections, short descriptions of van der Waals and electrostatic forces and how they relate to each other will be given.

4.2.1 Electrical double layer (EDL)

There are only a few, very simple systems were van der Waals (VDW) forces act alone, like interactions in vacuum or non-polar wetting films on surfaces. In more complex systems, long-range electrostatic forces must also be taken into consideration. As mentioned previously, VDW forces are always attractive, and if acting alone, these forces would cause all dispersed particles to stick together and precipitate. Usually, this is not the case though, as all particles dispersed in liquids with high dielectric constants usually are charged, and thus prevented from coalescing through electrostatic repulsive forces. Surfaces in liquids can be charged in three different ways:

1. Ionization or dissociation of surface groups, like dissociation of protons, which leaves a negatively charged surface.
2. Through adsorption/binding of ions from the dispersion onto an originally uncharged surface, called *ion exchangeable surfaces*.
3. By a *charge exchanging mechanism* between two chemically different surfaces located close together.

Independent on type of charge mechanism, the final surface charge of *co-ions* will be balanced by oppositely charged *counter-ions* in equal amount (Israelachvili, 2011). How the counterions are distributed close to a charged surface may be described using Stern-Gouy-Chapman theory, which divides the surface charge of a particle into two distinct layers; a compact inner layer and a diffuse outer layer (Riley, 2010). The latter was described independently by Gouy and Chapman (Chapman, 1913; Gouy, 1910), who developed a model for how the surface charge of a particle is balanced by a diffuse outer layer of ions, containing an excess of ions of opposite charge. The compact inner layer, first described by (Stern, 1924), consist of transiently bound counter-ions, and is known as the Stern layer, as indicated in Figure 2.7. Together these layers form what is known as the *electrical double layer* (EDL). As two charged particles approach each other in a liquid medium, their diffuse outer layers will begin to overlap, causing a repulsive force, which may outweigh the attractive VDW force. The distribution of ions

in the EDL depend on different factors, like concentration of electrolyte, formal charge of ions, solvent, and the potential at the boundary between the ion-packed inner layer and the diffuse outer layer. Under flow, a shear plane is created in this boundary, giving a potential known as the zeta (ζ) potential, which was described for cellulose nanocrystals in Chapter 2.2.3 (Israelachvili, 2011; Riley, 2010). The extension of the diffuse layer in dispersion is characterised by the Debye length ($1/\kappa$), which can be used to assess the decay of the ζ-potential, which is determined by the reciprocal of the Debye length, and referred to as the double layer thickness. This defines how far the "atmosphere" of counter-ions extends from a charged particle, and is governed by the ionic strength of the dispersing medium (Eastman, 2010). The effect of the ionic strength on the thickness of the EDL is shown in **Figure 4.3**.

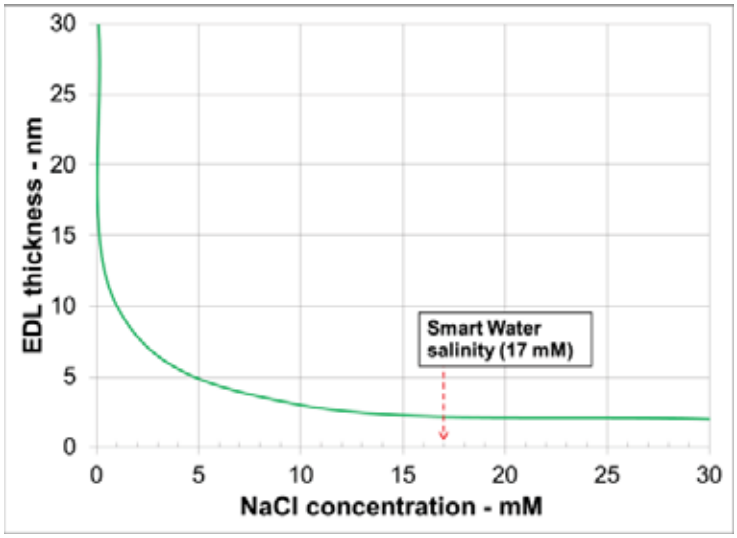

Figure 4.3: EDL thickness as a function of the salinity of the dispersing medium. Adapted from (Eastman, 2010).

4.2.2 DLVO theory

The DLVO theory is named after the scientists who developed it (Derjaguin & Landau, 1941; Verwey & Overbeek, 1955) and is based on the linear addition of electrostatic and VDW forces. It describes the total interaction potential

(Ψ_T) between any two surfaces and relates the attractive forces (Ψ_A) to the repulsive forces (Ψ_R) through Equation 4.16 (Eastman, 2010):

$$\Psi_T = \Psi_R + \Psi_A \tag{4.16}$$

The VDW interaction potential is usually insensitive to parameters like ionic strength and pH (unlike the electrostatic interactions), and may thus be considered as fixed. Also, since it is a power-law interaction, it must always exceed the electrostatic repulsion at small enough distances (Israelachvili, 2011). Figure 4.4 schematically depicts a classical DLVO interaction, where the total potential energy Ψ_T is given as a function of surface separation between two surfaces interacting in an aqueous salt dispersion through an attractive VDW force and a repulsive EDL force.

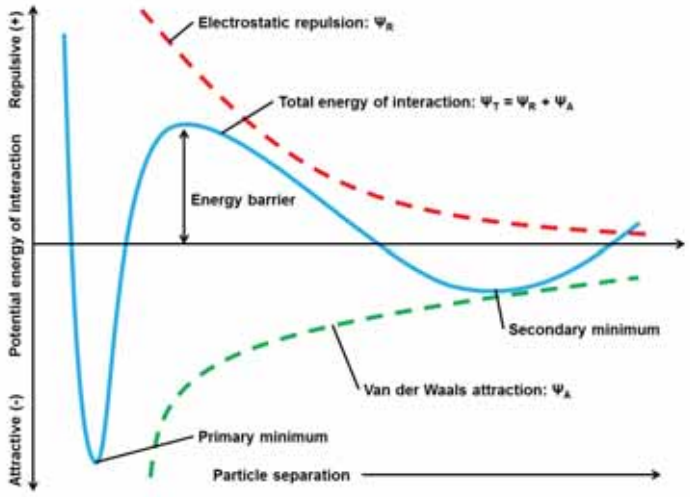

Figure 4.4: Potential interaction energy between two particles as a function of their distance.

The EDL potential is roughly exponential in distance dependence, and as mentioned earlier, its strength depends on the surface charge density, and its range depends on the ionic strength of the dispersing medium (Israelachvili & McGuiggan, 1988). According to these parameters, one of the following scenarios may occur:

- For surfaces with long Debye length (highly charged/low ionic strength) a strong long-range repulsion will peak at a distance (1 – 5 nm), known as the *energy barrier* of interaction.
- At higher ionic strength of the dispersing medium, there will be a significant *secondary minimum* (beyond 3 nm). The potential energy minimum at contact is called the *primary minimum*.
- Surfaces with low charge density will also have lower energy barrier, which leads to slow agglomeration.
- When the surface charge approaches zero, the interaction curve will approach the VDW curve (green, dashed curve in Figure 4.4).

To induce two (negatively) charged particles to adhere in a primary minimum, their surface charge must be lowered, either by decreasing the pH, increase the cation binding, or by increasing the salt concentration, which will lead to a shielding or screening of the EDL repulsion (Israelachvili, 2011).

The DLVO theory can be used to assess the forces related to fluid-fluid or fluid-solid interactions in oil reservoir water-floods, although it has its shortcomings. A lot of simplifications and assumptions have to be made, regarding surface smoothness and homogeneity, at high salinities there are deviations from the rule, and contact angles are not considered. These factors can make it difficult to interpret the interactions in an oil/brine/rock system, although it can be used as a method to model interactions (Ninham, 1999). It will not be accurate at high salinities, due to the theory being developed for single particles having a certain charge and not for complex systems (Shi et al., 2016).

4.2.3 Disjoining pressure

To describe wetting and de-wetting phenomena of immiscible liquids on solid surfaces, it very important to have a quantitative understanding of the interaction forces between the wetting and the non-wetting phase. How a solid surface prefers one fluid over another can usually be quantified by measuring the contact angle that a drop of liquid makes on a surface that is immersed in another fluid. This contact angle depends on the balance between the pressure in the non-wetting phase, which is the *capillary pressure,* P_c, and the disjoining pressure, Π, in the wetting film that separates the non-wetting

phase and the solid surface. Π starts to play an important role when the thickness of this wetting film becomes smaller than 0.1 μm. The Laplace-Young equation describes the stability of these thin separating wetting films:

$$P_c = \Pi + 2\sigma J \tag{4.17}$$

Where

P_c Capillary pressure
Π Disjoining pressure in thin film
σ Interfacial tension between phases
J Surface curvature

The value of J will be positive for concave surfaces and negative for convex surfaces. If applied P_c is larger than the net forces of disjoining pressure and curvature, the film wetting the surface will be unstable. For stable films, the thickness of the film will vary with applied P_c. The nature and magnitude of surface forces are dependent on the mineralogy of the solid surface, as well as the chemical properties of the wetting and non-wetting phases, and by alteration of pH or ionic strength (salinity) the wetting behavior of a surface can be altered (Basu & Sharma, 1996).

4.3 Wettability

An oil reservoir is a complex system, where the solid rock surface, liquids and gases interact. The effects of these interactions govern the fluid contacts and saturation distribution. It is therefore of great importance to have a certain understanding of how these forces interrelate and how this affects the properties of a reservoir.

4.3.1 Definition and classification

Wettability is the tendency for a given fluid to spread on a surface, when another immiscible fluid is present, and this is an important factor for oil displacement (Craig, 1971).

The wettability preference of a reservoir rock can be estimated by measuring the contact angle between the interface of the liquid/liquid or liquid/gas, and

the rock surface. This angle is called the *wetting angle* (θ), and is a result of the equilibrium that exists between IFT of the two fluid phases and their individual tendencies to adhere to the rock surface. The wetting angle is measured through the denser phase. If $\theta < 90°$, the denser fluid is the wetting phase, and if $\theta > 90°$, the less dense fluid is regarded as the wetting phase. The "strength" of the wettability of a particular fluid on a solid is related to the magnitude of θ, and a selection of categories for a water-oil-rock system is presented in Table 4.1 (Zolotukhin & Ursin, 2000d). An example of a water-wet and oil-wet system is shown in Figure 4.5.

Table 4.1: Contact angles for a water-oil system. Adapted from (Zolotukhin & Ursin, 2000d).

Contact angle (°)	Wettability preference
0 – 30	Strongly water-wet
30 – 90	Preferentially water-wet
90	Neutral wettability
90 – 150	Preferentially oil-wet
150 – 180	Strongly oil-wet

When two immiscible fluids, like oil and water, are present in an oil reservoir, there are three different IFT values at play, where:

σ_{os} IFT oil – solid
σ_{ws} IFT water – solid
σ_{ow} IFT oil – water

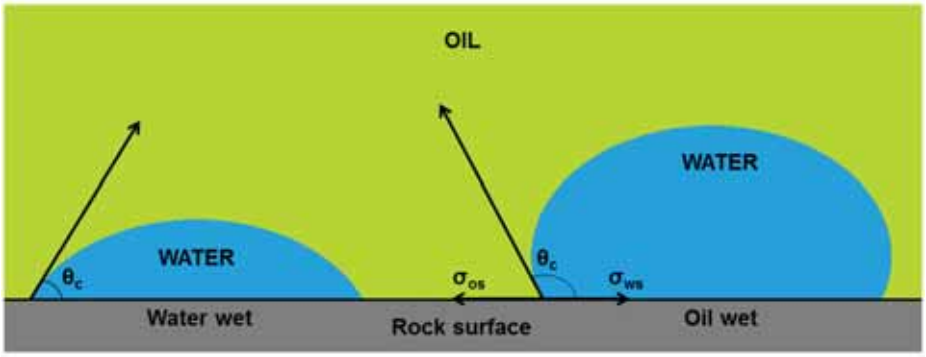

Figure 4.5: Contact angle measurement in a water-wet (left) and oil-wet (right) system. Adapted from (Craig, 1971).

The basis for a quantitative description of wetting phenomena is the Young's equation, which relates the contact angle to the interfacial tensions between the different components of the system (in this case, water-oil-solid), and is given in Equation 4.18 (Butt et al., 2006):

$$\sigma_{os} - \sigma_{ws} = \sigma_{ow} \cdot \cos\theta \tag{4.18}$$

The equation can be rearranged to show that θ reflects the equilibrium between the three involved IFTs, as shown in Equation 4.19 (Zolotukhin & Ursin, 2000d):

$$\frac{\sigma_{os} - \sigma_{ws}}{\sigma_{ow}} = \cos\theta \tag{4.19}$$

4.3.2 Evaluation of wetting in porous rock

For a water-flooding operation to be successful, it is of fundamental importance to estimate the wettability of the reservoir. Due to the complex structure of porous media, contact angle will not be representative. A better alternative is to utilise the Amott-Harvey or Amott-IFP test, which is described below.

Amott-Harvey and Amott-IFP: Broadly described, the Amott test from 1959 consists of changing the fluid saturation within a porous medium (Amott, 1959). The idea is that the wetting fluid will be able to spontaneously imbibe into the porous sample, thus expelling/displacing the non-wetting fluid. An Amott test consists of four different stages, which involves both spontaneous and forced imbibition, and drainage of oil and water, as described below:

1. *Spontaneous brine imbibition*: Brine is spontaneously imbibed into a core that initially is at irreducible water saturation (S_{wr}), before the core is placed in an Amott cell to control the amount of oil produced by the imbibing brine as a function of time.

2. *Forced brine imbibition*: Brine is forced to imbibe into the core material by using increased pressure, either by centrifugation or by

core flooding (Amott-IFP test, (N. R. Morrow, 1990)). This will lower the oil saturation to residual oil saturation (S_{or}).

3. *Spontaneous oil imbibition*: Oil is allowed to spontaneously imbibe the core sample at (S_{or}). Here, the Amott cell is placed upside-down, and the brine production is measured as a function of time.

4. *Forced oil imbibition*: Using the same pressure as for the brine in step 2, the oil is forced to imbibe the core. The process moves the saturation back towards (S_{wr}).

The Amott-Harvey wettability index (I_{AH}) relates the wetting indices of oil (I_o) and water (I_w), which are defined in Equations 4.20 and 4.21.

$$I_w = \frac{\Delta S_{ws}}{\Delta S_{ws} + \Delta S_{wf}} \tag{4.20}$$

$$I_o = \frac{\Delta S_{os}}{\Delta S_{os} + \Delta S_{of}} \tag{4.21}$$

ΔS_{ws} is the change in water saturation in the core during spontaneous imbibition of water; ΔS_{wf} is the water saturation change during forced imbibition. Also, ΔS_{os} and ΔS_{of} is the change in oil saturation during spontaneous and forced imbibition of oil, respectively. The Amott-Harvey wettability index is defined in Equation 4.22:

$$I_{AH} = I_o - I_w \tag{4.22}$$

The Amott-Harvey index will range from -1 to 1, where -1 indicates a strongly oil-wet state, and 1 a strongly water-wet state. At I_{AH} = 0, the wettability is neutral (Cuiec & Morrow, 1991).

4.3.3 Factors influencing wettability

The wettability of a system is affected by several factors, and all of them are linked to the chemical compositions properties of the system components, and

the interactions at work between them. Thus, the most important parameters are rock mineralogy, brine and crude oil composition.

Mineral type: The mineral composition of a rock governs the adsorption of polar components. A sandstone rock at standard reservoir pH will usually be negative charged, due to clays and silicates with isoelectric points in the range of 2.2 – 2.8 (Jaafar et al., 2014). The mineralogy can thus direct how the crude oil wets the porous surface (Buckley et al., 1998).

Brine composition: The properties of the brine is of great importance for the wetting behaviour of an oil reservoir, and the most dominating factors are brine salinity, chemical composition and brine pH (Anderson, 1986a). Wettability alteration in sandstone reservoir has gained a lot of attention in recent years, and the effect of brine composition on the initial wetting properties has been thoroughly investigated and validated in the laboratory (N. Morrow & Buckley, 2011; RezaeiDoust et al., 2011). Several hypotheses on the mechanism behind wettability alteration due to brine composition has been presented over the years, but lately the focus have been on the effect of pH, and how the initial wetting can be altered by use of low saline injection brines (low salinity effect, LSE) (T. Austad et al., 2010; N. Morrow & Buckley, 2011).

Crude oil composition: Large efforts have been made to understand how the crude oil composition affects reservoir wettability, due to its very complex mixture of organic compounds, also called NSO compounds, which have large varieties in molecular weight and properties. NSO compounds contain nitrogen, sulphur and oxygen, and are most commonly found in the heavier fractions of the crude oil; resins and asphaltenes (Anderson, 1986b). Asphaltenes have the highest molecular weights, but resins tend to have higher levels of NSO compounds, and are thus more polar than the asphaltenes. The NSO-rich resin fractions have higher surface activity, and may thus influence the wetting behaviour of the oil (Aksulu et al., 2012; Standnes & Austad, 2000). In contact with water, the oil-water interphase becomes charged, which exposes the electrical characteristics of the organic compounds. These vary in function dependent on type of compound and its concentration. Both positive and negative charges can be present at the interface, and the crude oil is adsorbed onto the mineral surface when

opposite charges interact, either through intermolecular or interionic forces (Buckley et al., 1998; Hirasaki, 1991). Buckley et al. (1998) lists what the main mechanisms of interaction are attributed to:

- Polar interactions predominating when the water film between the oil and solid is absent.
- Surface precipitation, depending mainly on crude oil solvent properties, with respect to the asphaltenes.
- Acid/base interactions controlling surface chare at oil-water and solid-water interfaces.
- Ion binding or specific interactions between higher valency ions and charged sites.

Other factors, like water chemistry and mineralogy must also be accounted for when determining if a crude oil is able to alter the wettability of a surface, because they impose important contributions to the interactions between the oil and the rock surface (Tor Austad, 2013; N. R. Morrow et al., 1998).

5 EOR in Sandstone using Smart Water and CNC

Today, the majority of oil reservoirs are flooded with water to improve the oil recovery, but initially, the main reasons for injecting water were:

- Provide pressure support to the reservoir to maintain the reservoir pressure, P_{res}, above the bubble point pressure, P_b, and
- Oil displacement due to viscous forces

Systematic laboratory studies the last 20 to 25 years on the wetting properties of various crude oil-brine-rock (CBR) systems, has verified that injection of brine with a different chemical composition from the initial formation water will lead to a destabilisation of the chemical equilibrium of the CBR system. The restoration of the chemical equilibrium could lead to a wettability alteration, and may also improve the oil recovery (Tor Austad, 2013).

5.1 What is a "Smart Water"?

To put it shortly, a "Smart Water" is an injection brine that is able to alter the wetting properties of a given reservoir rock and thus improve the oil recovery. It is prepared by adjusting and optimising the ion composition of the flooding fluid prior to injection. The following change in wetting of the reservoir rock has a positive effect on the capillary pressure, as well as the relative permeabilities to oil and brine. As no expensive chemicals are added, this recovery method has low application costs, and does not pose a threat to the environment. There is also no problem with injectivity, and there is no material retention in the reservoir (Tor Austad, 2013; S Strand et al., 2016).

5.2 Smart Water EOR in sandstone

As mentioned earlier, a large number of laboratory tests have established that enhanced oil recovery can be attained by performing an injection of Smart Water/low salinity (LS) brine in tertiary mode. The salinity of the brine will usually be in the range of 1000 – 2000 ppm. The foundation work has mainly

been put down by Norman R. Morrow and his research group (Tang & Morrow, 1999a, 1999b; Zhang & Morrow, 2006; Zhang et al., 2007) and researchers from BP (British Petroleum) (Lager et al., 2007; Webb, Black, & Edmonds, 2005; Webb, Black, & Tjetland, 2005).

5.2.1 Premises for Smart Water EOR

There are certain premises that must be fulfilled to observe low salinity effects from a water flood, and these have been established through thorough laboratory testing, and are listed below:

- The sandstone porous medium must contain clays (Tang & Morrow, 1999a).
- The crude oil must contain organic compounds (acids and/or bases) (Tang & Morrow, 1999a).
- Formation water must be present in the porous medium, and contain divalent cations like Ca^{2+} and Mg^{2+} (Lager et al., 2007; McGuire et al., 2005).
- The salinity of the injection brine is between 1000 and 2000 ppm, but effects have been observed up to 5000 ppm. It also seems to be sensitive to ionic composition (Ca^{2+} vs. Na^{+}) (Tang & Morrow, 1999a).
- The produced water usually shows an increase in pH (1 – 3 units) when LS brine is injected (Tang & Morrow, 1999a).

The key factor for the suggested chemical mechanism of the low salinity EOR, which is described in the next section, is the ability of the clay material to act as a cation exchange material (RezaeiDoust et al., 2011). The clay type governs the cationic exchange capacity (CEC), which for the three most common clay minerals increases in the order of: Kaolinite (3 – 15 meq/100 g) < illite (10 – 40 meq/100 g) < montmorillonite (70 – 120 meq/100 g) (Czurda, 2006). The most common clay minerals in sandstones are kaolinite and illite. Crude oil containing polar acidic and/or basic functional groups could adsorb onto the rock surface giving a mixed-wet oil reservoir (Lager et al., 2007; Tang & Morrow, 1999a). Sandstone reservoir rock is usually regarded as mixed wet (S Strand et al., 2016).

5.2.2 Smart Water EOR mechanism

A variety of mechanisms describing the EOR effect of low salinity brines have been suggested the last 10 – 15 years, and some of them are listed below:

- Migration of fines from the clay (Tang & Morrow, 1999a).
- Impact of alkaline flooding due to pH increase (McGuire et al., 2005).
- Multi-component ion exchange (MIE) at surface of clay (Lager et al., 2007).
- Microscopically diverted flow caused by migration of fines (A. Skauge, 2008).
- EDL expansion at the rock surface (Ligthelm et al., 2009).

A new mechanism was presented by Austad et al., (2010), where it was suggested that injection of low saline brine causes a desorption of surface active inorganic cations, leading to desorption of organic material (crude oil) from the clay surface due to a local increase in pH at the clay – water interface (T. Austad et al., 2010). The whole suggested mechanism is presented in Figure 5.1.

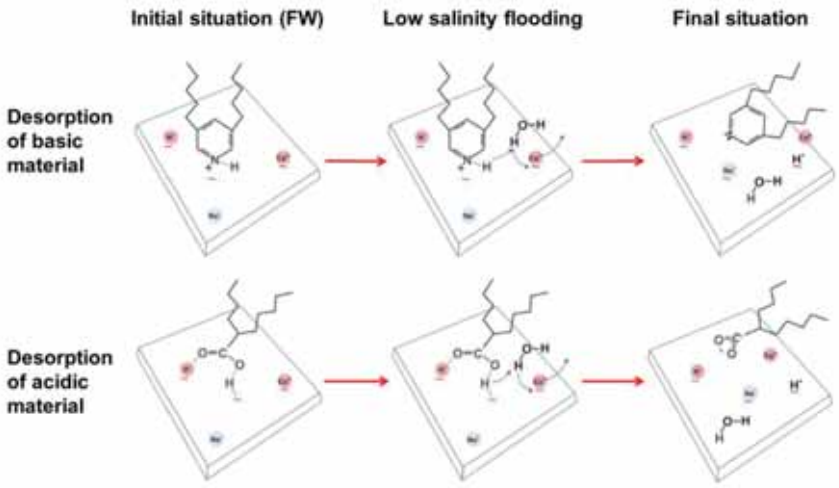

Figure 5.1: Schematic overview of the Smart Water mechanism, where low salinity flooding causes acidic and basic material adsorbed onto negatively charged clay minerals to be removed in an alkaline environment due to desorption of Ca^{2+} from the clay surface. Adapted from (T. Austad et al., 2010; S Strand et al., 2016).

As mentioned, the clay surface acts as a cation exchange material and the minerals contribute with most of the surfaces in sandstone reservoirs. In the beginning, both acidic and basic components are adsorbed onto the clay surface together with inorganic cations, particularly Ca^{2+}, from the formation water. A chemical equilibrium is established between crude oil, brine and rock over millions of years at reservoir conditions. Due to dissolved H_2S and CO_2, the initial pH of the formation water will be rather low. When low saline brine with a reduced ionic content is injected into the reservoir formation, the established equilibrium between crude oil, brine and rock is disturbed. This cause a net desorption of cations (Ca^{2+}) from the surface. To balance out the negative charges on the clay surface, H^+ from the water close to the surface is adsorbed onto the clay. This substitution causes a local increase in pH close to the clay surface. The Ca^{2+} is a slow process, and is shown in Equation 5.1.

$$\text{Clay-Ca}^{2+} + \text{H}_2\text{O} \rightleftarrows \text{Clay-H}^{+} + \text{Ca}^{2+} + \text{OH}^{-} + \text{heat} \tag{5.1}$$

The increase in pH causes the adsorbed anchor molecules to undergo ordinary acid-base H^+-transfer reactions, as shown in Eq. 5.2 for basic material and in Eq. 5.3 for acidic material.

$$\text{Clay-R}_3\text{NH}^{+} + \text{OH}^{-} \rightleftarrows \text{Clay} + \text{R}_3\text{N:} + \text{H}_2\text{O} \tag{5.2}$$

$$\text{Clay-RCOOH} + \text{OH}^{-} \rightleftarrows \text{Clay} + \text{RCOO}^{-} + \text{H}_2\text{O} \tag{5.3}$$

The pH gradient produced when the formation water is displaced from the pore matrix and exchanged with LS brine depleted of Ca^{2+} cations will cause a redistribution of the residual oil, due to the rock becoming more water-wet. The LS brine then has the ability to increase the capillary forces in the pores bypassed by the FW brine, and combined with the increase in capillary pressure due to the wettability alteration, the oil is mobilised and the microscopic sweep efficiency is increased. This effect is illustrated in Figure 5.2.

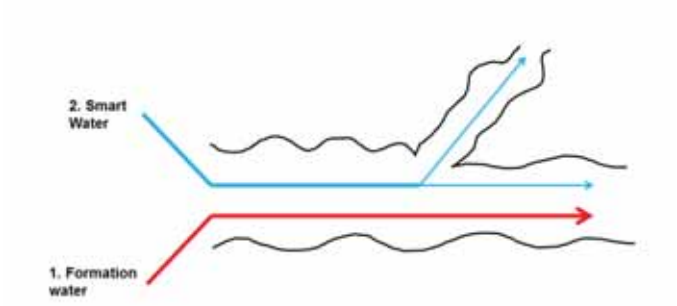

Figure 5.2: LS brine causes a wettability alteration, leading to positive capillary forces and increase in sweep efficiency. Adapted from (S Strand et al., 2016).

Some oil will also become trapped due to the increase in capillary forces, but if the amount of oil mobilised by the LS injection brine is larger than the amount of oil becoming trapped, a net EOR effect will be observed (T. Austad et al., 2010; RezaeiDoust et al., 2011; S Strand et al., 2016).

5.3 Proposed mechanism for Smart Water flooding with CNC

There are a number of executed and ongoing investigations of nanoparticles for use in enhanced oil recovery, where particles with lengths in the range of ±100 nm are being added to injection brine. Pore throats can be up to 10 μm in diameter in a reservoir rock of good quality (Nelson, 2009), and thus nanoparticles should easily be able to travel through porous matrices. These injection brines are usually called "nanofluids" (Li & Torsaeter, 2015) or "smartfluids" (Suleimanov et al., 2011), and come in several varieties, but silicon (SiO_2) derivatives are most common (Aurand et al., 2014; Ju et al., 2006; Li & Torsaeter, 2015) and use of rutile TiO_2 has also been documented (Hu et al., 2016). A number of mechanisms have also been proposed; including wettability alteration, IFT reduction, disjoining pressure, pore channel plugging ("log-jamming"), diverted flow and emulsification (Li et al., 2013; Li & Torsæter, 2014; A. Skauge, 2008).

The proposed mechanism for CNC dispersed in LS brine (CNC-LS) and used as an injection fluid for EOR, is "log-jamming", where the particles are caught in pore throats, causing blockage and microscopic flow diversion. A simplified illustration is given in Figure 5.3.

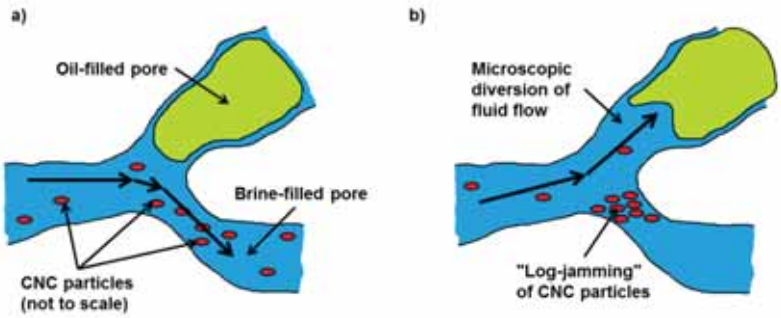

Figure 5.3: A simplified illustration of how injection of CNC together with LS brine might increase the oil recovery by log-jamming followed by microscopic flow diversion. In a) the injected fluid follows the path of least resistance. The oil has higher viscosity than the injected CNC-LS brine and avoids sweeping. In b) the CNC particles has caused a log-jam in the flow path. This is plausible if the pore throat narrows sufficiently so the particles are squeezed through. This may affect the flow path of the injected brine, and increase in pressure due to

decrease in permeability can lead to mobilisation of the oil droplet. Adapted from (Aurand et al., 2014).

The log-jamming effect can be explained by the mass difference between the particles and the dispersing medium. The pore throats are substantially smaller than the pores (Nelson, 2009), and in combination with the constant differential pressure the flow velocity will be higher in the pore throats than inside the pores. At the pore throat entrance, the water molecules will accelerate faster than the particles, due to the large mass difference between the water molecules and the particles. This leads to particle accumulation at the pore throat, which could slowly reduce the pore throat diameter, and eventually block it. The most important factors regarding log-jamming, are pore size distribution, particle concentration and effective hydrodynamic size of the injected particles, as well as the injection rate (Bolandtaba et al., 2009; T. Skauge et al., 2010). The working hypothesis with Smart Water is that injection of LS brine in secondary mode will alter the wettability of the sandstone pore matrix, redistributing immobile oil from the clay surface. This redistributed oil is then more easily accessible in EOR processes from the most available pores. Then CNC-LS injected in tertiary mode may cause log-jamming in these easily flooded pores, thus diverting the water flow into lesser available, oil-filled pores to further increase the oil recovery.

6 Materials and Methods

The materials and methods utilised for this thesis are described in the next two sections. The laboratory work was performed at two separate locations. Most of the CNC characterising work was performed at the Ugelstad Laboratory, which is a part of the Department of Chemical Engineering at the Norwegian University of Science and Technology (NTNU). Core flooding experiments were performed at the Smart Water laboratory facility at the Department of Petroleum Technology at the University of Stavanger (UiS).

6.1 Materials

In this section, the basic characteristics of the cellulose nanocrystals (CNC), brines, crude oil and core material used in the experiments.

6.1.1 Cellulose nanocrystals (CNC)

Concentrated stock dispersion of CNC (11.8 wt. %, dispersed in DI-water) was purchased from the University of Maine. The crystalline particles were produced by the US Forest Service's Cellulose Nanomaterials Pilot Plant at the Forest Products Laboratory (FPL) (Madison, Wisconsin, USA). FPL produces CNC in batches of 25 kg, and a short description of the production process is given below. It is thoroughly described in (Reiner & Rudie, 2013), and a schematic overview is given in Figure 6.1.

50 kg of Kraft wood pulp is placed under an inert N_2 atmosphere and heated to 45 °C. Sulphuric acid (64 wt. %) is also heated to 45 °C and slowly added to the pulp. The mixture is stirred at 45 °C for 90 minutes, before the hydrolysis reaction is stopped by adding the mixture to large amounts of water. 4 wt. % hypochlorite is added to remove colour, and the suspension is neutralised by diluting it with 8 wt. % NaOH. This will disperse the CNC particles in the solution. Ultrafiltration is then performed to remove salts and sugar (salts and sugars passes through the filter, CNC stays), and reverse osmosis (RO) water is added to keep the CNC concentration at 1 wt. %. Diafiltration is continued until the salt concentration is 8 μM (40 – 50 $\mu S/cm^2$). This process takes approximately 24 hours, and requires 20,000 L of

RO water. At last, the colloidal CNC particles are filtered through a 20 µm polypropylene filter to remove impurities, and ultrafiltrated to the desired concentration (wt. %).

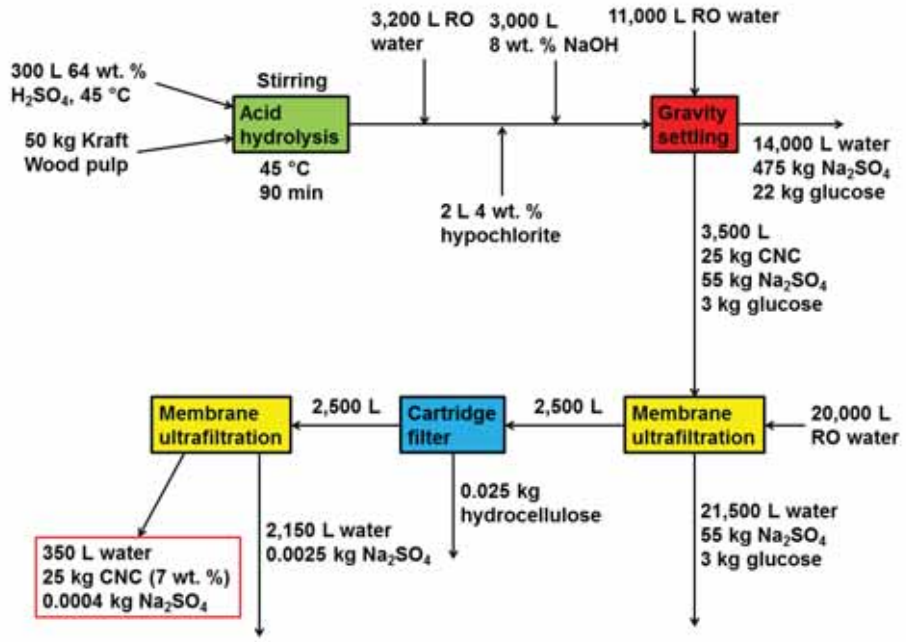

Figure 6.1: Schematic over the production procedure at FPL. For this process, the end product had a concentration of 7 wt. %, but this can be tuned via ultrafiltration. Adapted from (Reiner & Rudie, 2013).

The production procedure removes the amorphous domains of the cellulose material and leaves rod-like, crystalline particles with negative surface charge, due to sulphate half esters being produced on the surface during the hydrolysis step (Abitbol et al., 2013). Crystallites from the same batch were analysed by Heggset et al. (2013) and the dimensions of crystallites produced at the same plant (with the same method) was investigated with atomic force microscopy (AFM) by Sacui et al. These characteristics are given in Table 6.1.

Table 6.1: CNC characteristics, adapted from (Heggset et al., 2017) and (Sacui et al., 2014).

Sample	Charge density (mmol/g)	Crystallite diameter (nm)[c]	Crystallite length (nm)[c]	Functional groups
CNC	approx. 0.3[a,b]	5.9 ± 1.8	130 ± 67	-OH, $-SO_3H$

[a]Amount of sulphate ester groups
[b]Measured with inductively coupled plasma-atomic absorption (ICP-AA) (Heggset et al., 2017).
[c]Determined with atomic force microscopy (AFM) (Sacui et al., 2014).

CNC samples were prepared by dilution to the desired concentrations (in wt. %), with either de-ionized water (DI-water, resistivity = 18.2 mΩ, total organic content (TOC) < 5 ppb), or 1000 ppm NaCl brine (low salinity/LS brine). Samples were stored at 4 °C when needed, and are from now on denoted CNC-DI and CNC-LS, respectively.

6.1.2 Brines

Brines were prepared by mixing reagent grade chemicals as given in Table 6.2 with DI water (18.2 mΩ, TOC < 5 ppb). After the salts where added, the brine solutions were stirred for at least 1 hour until all the salts were dissolved. The brines were filtered prior to use by using 0.22 µm filter paper (Merck Millipore) and a vacuum pump. Formation water (FW) was diluted 5 times after preparation, and will from now on be denoted d_5FW. Brines were stored in Schott bottles at room temperature.

Table 6.2: Brine compositions. TDS = total dissolved solids, µ = viscosity

Ions	FW (mM)	d_5FW (mM)	LS (mM)
Na^+	1540	308	17
Cl^-	1720	356	17
Ca^{2+}	90	24	-
TDS (mg/L)	100 000	20 000	1000
pH	5.5	5.5	5.7
µ at 25 °C (mPa·s)	-	-	1.01
µ at 60 °C (mPa·s)	-	-	0.60

6.1.3 Core material

Two cylindrical outcrop sandstone cores were utilised in the experiments, and are denoted SM8 and SM10, respectively. The SM8 core was used for the injectivity experiments, and is shown in Figure 6.2, while the SM10 core was used in the EOR experiments. The mineralogical properties were investigated at an earlier stage, using X-ray diffraction analysis (XRD) (Piñerez Torrijos et al., 2016), and are given in Table 6.3.

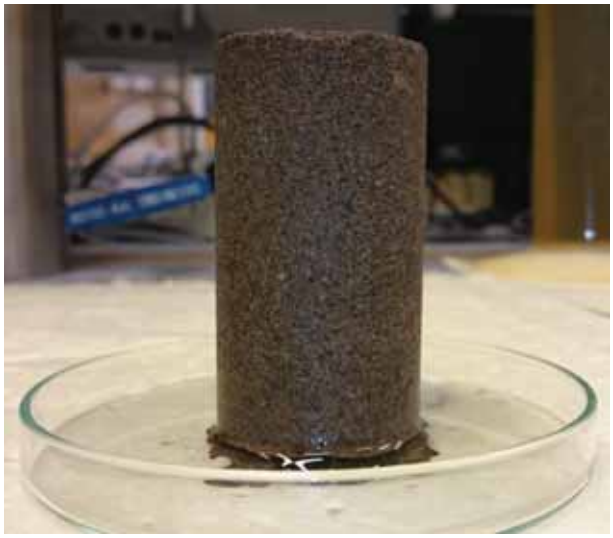

Figure 6.2: Outcrop sandstone core sample SM8.

Table 6.3: Mineralogical properties of the outcrop sandstone cores used in the experiments, given in wt. %. Adapted from (Piñerez Torrijos et al., 2016).

Albite	Quartz	Calcite	Chlorite	Illite	Clays & micas
32.0	57.0	0.3	1.9	8.6	10.5

The weight difference between a clean, dry core and a core 100 % saturated with LS brine was first used to calculate the available pore volume of the core, before the porosity was calculated, using Equation 6.1.

$$\text{Porosity} = \frac{\text{Core plug pore volume}}{\text{Core plug gross volume}} \times 100\% \quad (6.1)$$

The physical properties of the sandstone cores are listed in Table 6.4.

Table 6.4: Physical core properties.

Core #	Length (cm)	Diameter (cm)	Pore volume (mL)	Dry weight (g)	Sat. weight (g)	Porosity (%)
SM8	7.1	3.8	16.2	164.4	180.7	20.3
SM10	7.0	3.8	16.3	165.8	182.3	20.5

The same outcrop sandstone core material has been used previously in EOR and LS brine studies, with very good experimental reproducibility between individual cores (Piñerez Torrijos et al., 2016).

6.1.4 Crude oil

Stabilised crude oil was centrifuged at high rotation speed for 1 hour and filtered through 10 μm Millipore filter under vacuum to remove impurities. The process was repeated with centrifugation step and filtration through 8 μm filters, and at last centrifugation and filtration through 5 μm filters. The acid number (AN) characterises crude oil through the total concentration of strong and weak acids, and is given as the amount of potassium hydroxide (KOH) needed to neutralise the acids in one gram of oil. The base number (BN) is a measure of the alkalinity of crude oil, given in mg KOH/g crude oil. Both values were acquired by potentiometric titration based on modified versions of ASTM (American Society for Testing Materials) D2896 for BN and ASTM D664 for AN ((ASTM), 1988, 1989; Fan & Buckley, 2006). An overview of the crude oil properties is given in Table 6.5. The analyses were performed at the Smart Water EOR laboratories at UiS.

Table 6.5: Crude oil properties.

Acid number (AN) mg KOH/g	Base number (BN) mg KOH/g	Density at 20 °C	Viscosity at 20 °C
0.1	1.8	0.8459 g/cm^3	17.6 cP

6.2 Methods

6.2.1 Rheology

Rotational rheometers were used to assess the dispersion viscosities under varying conditions. Two different models were used, due to the experimental work being performed in two different locations. Both rheometers were delivered by Anton Paar GmbH (Graz, Austria). At the Ugelstad laboratory (NTNU), the Physica MCR 301(Rheoplus v.3.40 software) model was used, and at the Smart Water EOR facility (UiS) the Physica MCR 302 (Rheoplus v.3.62 software) model was used.

Concentration dependency: CNC-LS brines with increasing concentration of CNC (0.5 – 4.0 wt. %) were prepared for core-flooding experiments. A stock dispersion of 500 mL 4 wt. % CNC-LS was prepared in 1000 ppm LS brine, and dispersions for experiments were prepared by dilution to 2, 1 and 0.5 wt. % CNC. The viscosity of the dispersions was tested using a cone-and-plate geometry, with a cone diameter of 50 mm and a 1° cone angle. Shear rates were set from 10 – 1000 s^{-1}, set up with logarithmic ramp, and the measurements were performed at 20 °C.

Ionic strength dependency: CNC-LS brines with increasing concentration of NaCl were prepared to investigate how the brine salinity influenced the rheological properties of the dispersion. Concentrations of 0, 0.1, 1.0 10 and 17 mM (1000 ppm) NaCl were prepared with CNC to a concentration of 1 wt. %. The viscosity of the dispersions was tested using a cone-and-plate geometry, with a cone diameter of 50 mm and a 2° cone angle. Shear rates were set from 10 – 1000 s^{-1}, set up with logarithmic ramp, and the measurements were performed at 20 °C.

pH dependency: Samples with 0.5 wt. % CNC were prepared in DI water and LS brine. Dispersion pH was adjusted by titration with either 50 mM NaOH or 50 mM HCl to the desired value. Both titrants were prepared with laboratory grade reagents and DI water. The pH effect on the viscosity of the dispersions was tested using a cone-and-plate geometry, with a cone diameter of 50 mm and a 1° cone angle. Shear rates were set from 10 – 1000 s^{-1}, set up with logarithmic ramp, and the measurements were performed at 20 °C.

Heat aging 120 °C: The effect of heat aging on dispersion viscosity was investigated by using 2.0 wt. % CNC dispersions in both DI water and LS brine. Four 2.0 wt. % CNC-DI and four with 2.0 wt. % CNC-LS samples equipped with heat-resistant lids were prepared. 3 CNC-DI and 3 CNC-LS were placed in a heating cabinet at 120 °C. The shear viscosity of the non-aged dispersions was measured at 20 °C using a cone-and-plate geometry, with a cone diameter of 50 mm and a 2° cone angle. Shear rates were set from 10 – 1000 s^{-1}. The heat aged samples were left in the heating cabinet for 24, 48 and 168 hours, respectively. After cooling down to room temperature, the samples were subjected to the exact same viscosity measurement regime as the non-aged dispersions. Two samples were also heat aged at 90 °C for 168 hours for comparison.

Dynamic heat aging 90 °C: Continuous viscosity measurements during heat aging were also performed, and for this procedure a CC27 cylinder-and-cup geometry was utilised. 0.5 and 2.0 wt. % CNC dispersions were added to the sample cup, with a thin layer of low viscosity silicon oil (Brookfield Viscosity Standard 9.4 cP, Marlboro, MA, USA) deposited on top of the samples, to prevent water evaporation during aging and measurements. The CNC samples were heat aged at a constant temperature of 90 °C in the rheometer geometry at static conditions. Every 2 hours, the sample viscosity was measured, and measurement points were taken out during the shear measurements. The first 6 experiments were performed in three parallels each, for a total of 50 hours. These experiments were performed on 2.0 wt. % CNC-DI and CNC-LS. For the two last measurements, the total measuring time was extended to 175 hours. These tests were performed using 0.5 and 2.0 wt. % CNC-LS samples.

6.2.2 Zeta potential

Zeta potential measurements were performed on CNC dispersions. The measurements were performed using a Malvern Zetasizer Nano ZS (Malvern Instruments Ltd., Malvern Worcestershire, UK) at the Ugelstad Laboratory (NTNU). The Zetasizer applies a known electrical field to the electrolytic sample, and charged particles dispersed in the electrolyte will move towards the oppositely charged electrode. Viscous forces opposes this movement, and when these two forces are in equilibrium, the particle will move with a

constant velocity (v), also known as the electrophoretic mobility, which is dependent on the strength of the electric field (E), the dielectric constant of the medium (ε), viscosity of the medium (η) and the zeta potential (ζ). The electrophoretic mobility (μ_E) is given in Equation 6.2.

$$\mu_E = \frac{v}{E} \tag{6.2}$$

μ_E is measured with laser Doppler velocimetry (LDV). The zeta potential cannot be measured directly, but by using theoretical model and an experimentally determined electrophoretic mobility it can be calculated by using the Smoluchowski equation (6.3) (Smoluchowski, 1903):

$$\mu_E = \frac{\varepsilon_r \varepsilon_0 \zeta}{\eta} \tag{6.3}$$

Where ε_r is the dielectric constant of the dispersing medium (here it is water), ε_0 is the permittivity of free space ($C^2\ N^{-1}\ m^{-2}$), η is the dynamic viscosity of the dispersing medium (Pa·s), and ζ is the zeta potential (mV). The Smoluchowski equation is valid for thin double layers (radius smaller than the particle radius), and can be applied to most aqueous systems, due to the EDL being only a few nm in water.

The CNC concentration was 0.5 wt. % in all the prepared samples. Prior to measurements, the samples were sonicated for 5 minutes using an ultrasonic bath (VWR Ultrasonic Cleaner), and the pH was measured using a Mettler Toledo SevenEasy S20 pH-meter (Sigma-Aldrich). All reported values are an average of 15 measurements.

Ionic strength dependency: The experiments investigating the effect of ionic strength on the zeta potential were performed at 20 °C. Samples were prepared with 0, 0.1, 1.0, 10 and 17 mM (1000 ppm) LS brine. The standard DTS1060 folded capillary cell (Malvern Instruments Ltd., Malvern Worcestershire, UK) (old model) was used for these measurements.

pH dependency: A Malvern MPT-2 autotitrator (Malvern Instruments Ltd., Malvern Worcestershire, UK), equipped with a pH probe and 50 mM NaOH and HCl titrants was used in the pH dependency measurements. Samples were

prepared with either DI water or 1000 ppm LS brine. The titrants were prepared by using reagent grade chemicals and DI water. The experiment was performed at 20 °C, and therefore the standard folded capillary cell (DTS1070) (Malvern Instruments Ltd., Malvern Worcestershire, UK) (new model) was used.

Temperature dependency: For the experiments using temperatures from 50 – 90 °C, the Universal 'dip' cell kit (ZEN1002, Malvern Instruments Ltd., Malvern Worcestershire, UK) equipped with a quartz cuvette was used, as the DTS1070 would be damaged at higher temperatures. The samples were prepared with either DI water or LS brine.

6.2.3 Atomic force microscopy

Morphology of native and heat aged CNC dispersions was qualitatively investigated by atomic force microscopy (AFM), using a Bruker Multimode V AFM equipped with a Nanoscope V Controller (Veeco Instruments Inc., Santa Barbara, CA, USA). The instrument was located at the NorFab facility NTNU NanoLab in Trondheim. Images were acquired by Scan Asyst mode in air at ambient temperature. Scan Asyst-Air AFM tips were provided by Bruker AFM Probes (Bruker Nano Inc., Camarillo, CA, USA). These probes have a silicon tip on a nitride lever, and a spring constant of 0.4 N/m. Scans were analysed using the NanoScope Analysis v.1.40 software and modified with the ImageJ v.1.50i program. An image of the AFM is shown in Figure 6.3.

Figure 6.3: AFM with tip holder, laser and mirrors

AFM samples were prepared according to the method used by (Lahiji et al., 2010). A drop of 0.5 wt. % CNC dispersion (-DI or -LS) was placed on freshly cleaved 10 mm mica (Agar Scientific Ltd., Essex, UK). Mica is easily cleaved to reveal large atomically smooth surfaces (Drummond & Israelachvili, 2002). The mica discs were glued to magnetic sample holders. The drop was left on the mica for ~1 minute, before rinsing with DI water and dried using compressed N_2 gas. The rinsing and drying method is used for two reasons; First, to lower the concentration of CNC particles so they are more easy to distinguish and second, the CNC particles that remain on the surface will be thoroughly adhered to the mica substrate (Lahiji et al., 2010).

6.2.4 Core restoration

A core restoration procedure was performed prior to core flooding and EOR experiments.

Core cleaning: A mild core cleaning procedure was applied to remove initial fluids. First, the core was flooded with kerosene, to displace any residual crude oil from the pores. The kerosene flooding was continued until clear effluent. This was followed by heptane to displace the kerosene. At last the core was flooded with LS brine to displace brine and easily dissolvable salts. An injection rate of 0.15 mL/min was used during core cleaning. After cleaning, the core was dried at 90 °C to a constant weight.

Initial water saturation: The sandstone core used in injectivity experiments was saturated 100 % with LS brine under vacuum and mounted in the core holder.

The core used in the EOR experiments was restored to initial FW saturation by using the desiccator technique, as described by (Springer et al., 2003). The core was evacuated and 100 % saturated with 5 times diluted FW (d_5FW). 20 % initial water saturation (S_{wi}) was established by water evaporation using silica gel in a desiccator. When the desired S_{wi} was reached, the core was placed in a sealed container and matured for 3 days to achieve a more homogeneous water and ion distribution.

Crude oil saturation: The core with 20 % S_{wi} was mounted in a core holder and saturated with crude oil under vacuum at 50 °C. 2 PV of filtrated crude oil was injected, first in one direction and second in the opposite direction. After crude oil saturation, the core was wrapped in Teflon and put in a steel aging cell, and aged at the temperatures designated for the EOR experiments (60 and 90 °C).

6.2.5 Core flooding

All core flooding and EOR experiments were performed in a computer controlled core flooding setup, which consisted of a Gilson HPLC 307 pump, stainless steel piston cells for the individual injection fluids, either LS brine or CNC-LS brine dispersion, and a Hassler core holder (Figure 6.4), placed in a heating cabinet, gauges for monitoring the inlet and differential (dP) pressure, as well as the temperature. The core flooding was performed with a confining pressure of 20 Bar and a back pressure of 10 Bar to secure fluid flow through the porous core and avoid pressures below the liquids' boiling points.

Figure 6.4: Hassler core holder used in the experiments.

Produced water and oil was collected using a glass burette separator and a Gilson GX-271 Liquid Sampler (Gilson Inc., Middleton, WI, USA. An overview of the setup can be seen in Figure 6.5.

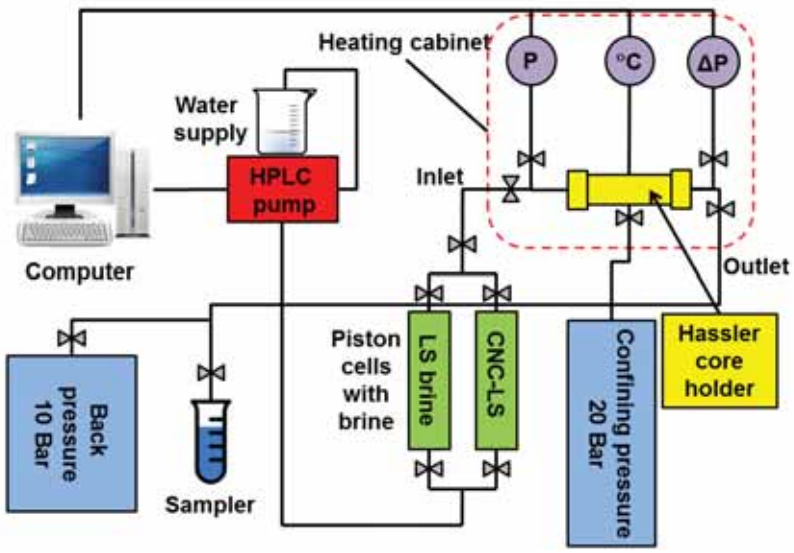

Figure 6.5: Schematic of the core flooding setup used in water flood and EOR experiments. Line valves are shown in grey, and were used to regulate line flow.

The restored core was placed in the core holder. The setup was equilibrated overnight with bypass flow (no fluid flooded through the core) to ensure stable temperature and pressure as well as air tight flood lines prior to testing. Core flooding experiments were performed in series at given temperature with LS brine and CNC-LS dispersion flooded in successive order at a rate of 4 PV/day (0.045 mL/min). The oil recovery experiments were performed in the same core flooding setup at 60 and 90 °C, and flooded consecutively with the different brines at a constant injection rate of 4 PV/day.

The permeability was evaluated by flooding a 100 % LS-brine saturated core with LS brine to acquire stable and accurate differential pressure (dP) measurements. This was performed prior to the CNC-LS injection at every temperature step. The CNC-LS dispersion was injected at constant rate (4 PV/day) and the dP was monitored during the injection. Effluent CNC-LS samples were collected and liquid analyses were performed. After the experiment was terminated, the core was regenerated by flooding LS brine in the opposite direction. Any plugging of CNC particles on the core inlet surface would be displaced. Permeability measurements prior to the next CNC-LS injection were performed to detect any changes in core properties.

Permeability is calculated using the Darcy equation (Eq. 2.1) and given in milliDarcy (mD) (Zolotukhin & Ursin, 2000c):

$$k = \frac{\mu \Delta x}{A} \frac{u}{\Delta P} \tag{2.1}$$

Where

μ	Viscosity of the injected fluid (for water at 60 °C = 0.47 mPa·s)
Δx	Length of sandstone core sample (cm)
A	Cross sectional area of sandstone core sample (cm^2)
u	Flow rate of the injected fluid (mL/min)
ΔP	Differential pressure over the sandstone core sample (mBar)

An overview of the experimental sequence is given below:

Concentration effect:

1. Flooding LS brine – permeability measurement, 20 °C, 16 PV/day until stable dP.
2. Injection of CNC-LS dispersion, 0.5 wt., 1.0 wt. % and 2.0 wt. %, 4 PV/day at 20 °C.
3. Flooding LS brine, 4 PV/day until no increase in dP was observed.
4. Flooding LS brine, reverse direction, 16 PV/day at 20 °C.
5. Repeat from Step 1.

Temperature effect:

1. Flooding LS brine – permeability measurement, 60 °C, 16 PV/day until stable dP.
2. Increase temperature (water flooding were performed at 60, 90, and 120 °C), while flooding LS brine.
3. Injection of CNC-LS dispersion, 4 PV/day.
4. Decrease temperature to 60 °C.
5. Flooding LS brine, 4 PV/day until no increase in dP was observed.
6. Flooding LS brine, reverse direction, 16 PV/day at 60 °C.
7. Repeat from Step 1.

7 Results and Discussion

The aim of this thesis was to shed light on a possible new application for the cellulosic nanomaterial cellulose nanocrystals (CNC), and the main focus has been on characterising CNC dispersed in low saline Smart Water brine to assess its potential for use in sandstone enhanced oil recovery (EOR).

The work performed can be roughly divided into two parts: First a characterisation part, where the CNC particles were subjected to a variety of conditions to mimic the strains the particles will approach in an actual oil reservoir and how they respond to these, and to optimise the parameters for use of CNC particles as a potential EOR chemical.

The second part deals with how well the particles perform in laboratory scale core floods, both with and without crude oil, by using outcrop sandstone cores with reproducible core properties, and at conditions where temperature, mineralogy, pore distribution, injection rates, salinity and particle concentration are in a range expected for oil reservoirs

From this experimental work, three journal articles were produced. These are appended at the end of the thesis. The work performed in the articles is the same that is presented here, but the sequence of the results is changed to draw a better picture of the evaluation process.

7.1 Zeta potential

Zeta potential measurements were performed to investigate the colloidal stability of CNC dispersions at various NaCl concentrations, temperatures and pH values. These stability parameters are important when assessing new nanoparticles for water flooding purposes, as flocculation and aggregation of dispersed particles may lead to injectivity loss into a porous medium like sandstone.

7.1.1 Stability with increasing salinity

0.5 wt. % CNC was dispersed in brines with salinities from 0 – 17 mM NaCl. 17 mM NaCl equals 1000 ppm NaCl per litre of DI water, which is the brine salinity used for all the core flooding experiments. The pH of the dispersions was not fixed during measurements, but determined for each NaCl concentration prior to measurements, and it was observed that the pH of the CNC dispersions decreased when the NaCl concentration was increased. For CNC in DI-water, the pH was 6.8, and when the concentration of NaCl was increased, the pH was reduced down to 5.8 for a 17 mM NaCl solution. All pH values are given in Table 7.1 and indicated in Figure 7.1.

Table 7.1: pH values of prepared CNC dispersions

CNC concentration (wt.%)	NaCl concentration (mM)	pH
0.5	0.0	6.8
‘’	0.1	6.7
‘’	1.0	6.4
‘’	10.0	6.0
‘’	17.0	5.8

When dispersed in water, the natural counterion to CNC prepared through sulfuric acid hydrolysis will be H^+ (Beck et al., 2012). Addition of small amounts of neutral salts (like NaCl) leads to an increase in the concentration of free H^+ (Robinson, 1929) in the water phase of the dispersion. The reduction in pH is probably due to a counterion exchange in the electric double layer (EDL) surrounding the CNC, where Na^+ enters the EDL of CNC and H^+ is substituted into the bulk phase.

Figure 7.1 shows the measured zeta potentials at increasing NaCl concentrations in a 0.5 wt. % CNC dispersion.

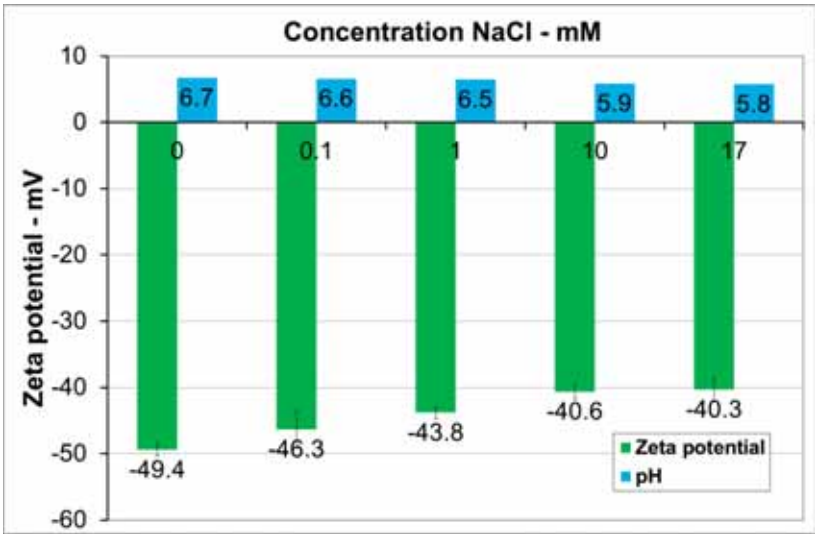

Figure 7.1: Zeta potential and pH of 0.5 wt. % CNC dispersions, as a function of increasing NaCl concentration.

The results confirm that the CNC particles carry a significant negative surface charge. The zeta potential for CNC in DI-water was measured to -49.4 mV. As observed in Figure 7.1, the zeta potential decreased with increasing NaCl concentration. At 17 mM NaCl, the zeta potential was reduced to -40.3 mV. According to (Zhong et al., 2012), dispersed CNC with a negative zeta potential larger than -30 mV, will be dominated by repulsive forces. If the absolute zeta potential of a dispersion moves closer to zero than ± 30 mV, for example by increasing the electrolyte concentration, the attractive van der Waals force will dominate over the repulsive force. This effect is caused by the negative charges on the surface of CNC particles being shielded by the increasing concentration of counter-ions. At such conditions, charged colloidal particles tend to aggregate because of a decreased repulsion barrier (Zhong et al., 2012). The zeta potential for a 0.5 wt. % CNC dispersion was never lower than -40 mV, which indicates that the dispersions remain stable even when the electrolyte concentration is increased above 17 mM NaCl.

7.1.2 pH effects

When injection brines are flooded through a sandstone medium, the pH in the brine might fluctuate between ~5 and ~9, depending on the brine composition

and interaction with surface minerals. It is therefore of great interest to investigate the colloidal stability of the CNC dispersions within this pH range. Zeta potential measurements were performed at 20 °C on 0.5 wt. % CNC dispersed in both DI water and 1000 ppm NaCl. The pH of the dispersions was adjusted between 5 and 9 using an autotitrator, and the results are shown in Figure 7.2.

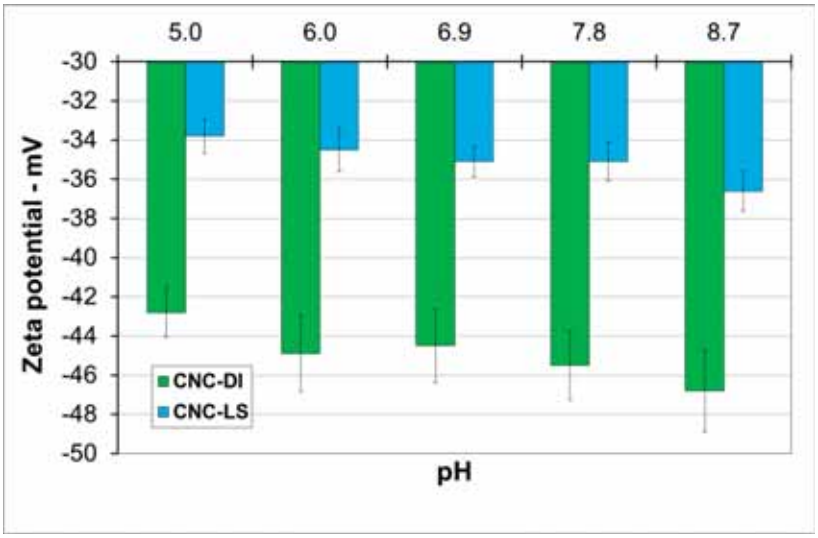

Figure 7.2: Zeta potential of a 0.5 wt. % CNC dispersion as an effect of dispersion pH, measured at 20 °C.

The zeta potential for the CNC dispersion in LS brine varied between -33.8 ± 0.9 mV at pH 5 to -36.6 ± 1.0 at pH 9, which was higher than that of the CNC dispersed with DI water, which varied between -42.8 ± 1.3 mV and -46.8 ± 2.1 mV at the same pH values. These results are in line with the previous observations made in Figure 7.1. The measured zeta potential confirmed that the dispersion should be regarded as stable above 30 mV in absolute value, Salopek et al., 1992. At all pH values tested, in both DI and LS brine, the negativity remained almost constant in the pH range from 5 – 9, indicating that the isoelectric point (IEP) of the sulphate half ester groups may be lower than pH 5. From this it can be deduced that no significant effect of pH was observed within the tested range, and aqueous dispersions of CNC will remain stable within the pH values that will be encountered in lab scale sandstone core flooding experiments.

7.1.3 Temperature influence

The zeta potential of dispersed CNC was also investigated at increasing temperatures, ranging from 50 – 90 °C, to assess how the dispersion stability could be affected at reservoir temperature. Dispersion pH was measured before the experiments, and it was 6.3 for the CNC-DI dispersion, and 5.5 for the CNC-LS dispersion. The results are presented in Figure 7.3 and confirms that there are no significant differences in the zeta potential for the different temperatures, neither in CNC-DI nor CNC-LS dispersions. Both dispersions remained within the stable limits for all tested temperatures.

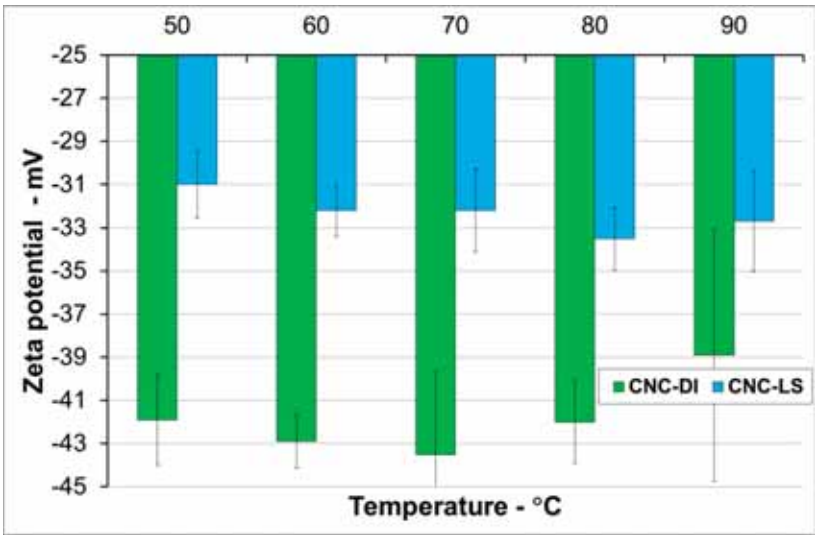

Figure 7.3: Zeta potential as a function of increasing the testing temperature from 50 – 90 °C.

7.2 Rheology

The viscosity of a CNC dispersion is first and foremost dependent on two parameters; the concentration of the dispersed particles and the ionic strength of the dispersing medium. Other parameters that have been investigated are heat aging and the effect of reservoir pH conditions.

7.2.1 Effect of CNC concentration

When CNC is dispersed in an aqueous medium, it increases the shear viscosity of the dispersing phase. This viscosifying effect is due to the electrostatic repulsion between the negatively charged CNC rods, creating an electric double layer. Water structuring can also account for some of the increase in viscosity of the dispersion. Hydrogen bonding can be a powerful structuring force, especially for carbohydrates. The hydroxyl groups attached to glucose molecules on the CNC surface, that did not undergo sulphation during the hydrolysis step in the production process, are capable of donating and accepting hydrogen bonds with the solvent fluid (Astley et al., 1996).

The rheological behaviour of 0.5, 1.0, 2.0 and 4.0 wt. % CNC dispersed in 1000 ppm (17 mM) NaCl LS brine is shown in Figure 7.4.

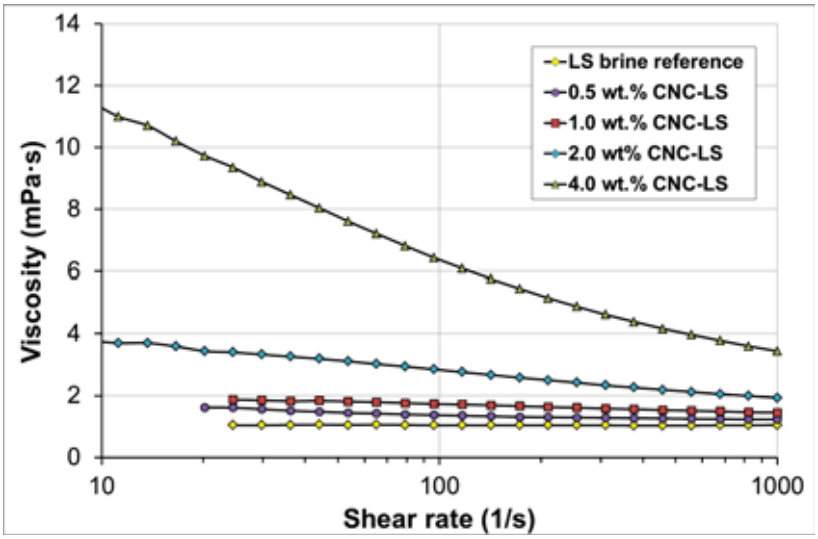

Figure 7.4: Viscosity of CNC-LS dispersions at increasing shear rates from 10 – 1000 1/s. Measurements were performed at 20 °C.

The minimum overlap concentration (φ_c), which defines the lowest particle/polymer concentration where the dispersed material is affected by the repulsive forces of the EDL is defined by Equation 7.1 (Bercea & Navard, 2000).

$$\varphi_c = \frac{d^2 L}{L^3} \times 100 \tag{7.1}$$

Where φ_c is the critical concentration (volume fraction), d is the diameter (or height) of the particles, while L is the length. φ_c for the CNC particles measured by (Sacui et al., 2014) (L = 130 nm, d = 5.9 nm) is therefore 0.206 %. This value was multiplied with the weight density of CNC, which was measured to be 1.46 g/cm3 by (Sun, 2005), giving a weight fraction of 0.30 wt.%. The dispersion concentration is thus above the critical overlap concentration for the EDL, for all concentrations used in this study, and it is therefore reason to believe that inter-particle interactions exists in the system.

As observed in Figure 7.4, the shear viscosity of the dispersions increases with increasing CNC concentration. The viscosity of LS brine is given as a baseline reference, and at room temperature the viscosity of LS brine is approximately the same as for DI water (1 mPa·s). The dispersions with higher concentrations of CNC (2.0 and 4.0 wt. %) showed shear dependent behaviour, with the highest effect seen for 4.0 wt. % CNC. The lowest concentrations (0.5 and 1.0 wt. %) exhibited Newtonian behaviour, as their viscosity was independent of the shear rate. The typical three region viscosity profile was difficult to observe for the shear rates used, although the higher concentrations exhibited the third region plateau, where the high shear stress destroys the liquid crystalline domains, making the rod align individually with the flow direction. These results are in accordance with the observations made by (Shafiei Sabet, 2013), although in that study the CNC particles were dispersed in DI water without electrolytes. Increasing the ionic strength of the dispersing medium will affect the shear viscosity of a dispersion, and is investigated in the next section.

7.2.2 Effect of salinity

The effect of increasing dispersion salinity was investigated by subjecting 1.0 wt. % CNC dispersions with increasing amount of NaCl to steady state shear viscosity measurements, as described in the Methods section. The salt concentrations ranged from 0 to 17 mM. The highest salt concentration is

equal to 1000 ppm NaCl, and is the concentration used in all core flood experiments. The salinity effect on CNC dispersions is shown in Figure 7.5.

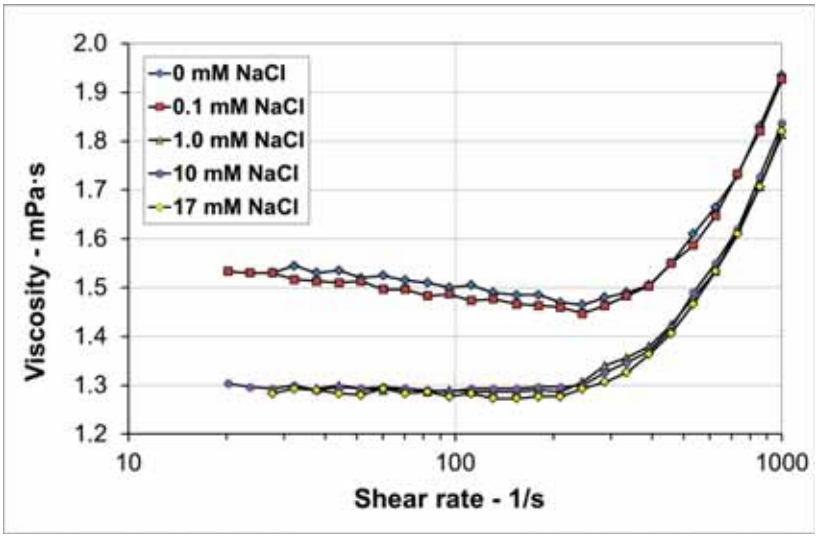

Figure 7.5: Viscosity measurements performed on CNC-LS dispersions at shear rates from 10 – 1000 1/s. All dispersions had a CNC concentration of 1.0 wt. %, with an increasing amount of NaCl. Measurements were performed at 20 °C.

As observed in Figure 7.5, all the dispersions behaved as Newtonian fluids and were thus independent of the shear rate at low shear rates. The effect observed at higher shear rates are most likely caused by turbulent flow in the dispersion.

A slight decrease in viscosity is observed when the salt concentration is increased from 0.1 to 1.0 mM. As mentioned, the sulphuric acid hydrolysis step during production leaves the CNC particles with a net negative electric charge; due to produced sulphate half ester groups on the surface of the particles. When exposed to NaCl solutions with salinity above 1 mM, the EDL of the particles is compressed, due to Na^+ counterions shielding negative charges on the CNC surface, leading to a lower repulsion between the particles due to shrinkage of the EDL, and thus a reduction in shear viscosity. The shielding leads to a reduction in overlapping of electric double layers and also fewer interactions between the CNC particles, which again could lead to a reduction in viscosity.

7.2.3 Effect of pH

Shear viscosity tests were performed on 0.5 wt. % dispersions with pH ranging from 5 to 9, to investigate if the dispersion viscosity could be affected by the sandstone reservoir pH conditions. Dispersion pH was adjusted by titration, but the volumes added were so small that it did not affect the CNC concentration in the dispersions significantly. The amounts added are given in Table 7.2.

Table 7.2: pH values in 0.5 wt. % CNC samples dispersed in DI water and LS brine, before and after titration with either 50 mM NaOH or 50 mM HCl.

Sample type	Initial pH	Desired pH	Testing pH
CNC-DI	6.9	5	5.1
CNC-DI	7.1	6	6.1
CNC-DI	7.1	7	6.9
CNC-DI	7.3	8	7.9
CNC-DI	7.0	9	8.9
CNC-LS	5.6	5	5.2
CNC-LS	5.7	6	6.0
CNC-LS	5.7	7	7.0
CNC-LS	5.7	8	8.1
CNC-LS	5.7	9	9.0

The results are shown in Figure 7.6 and Figure 7.7, and revealed that the pH did not affect the dispersion viscosity. The viscosity of the CNC-LS samples was somewhat lower than that of the CNC-DI samples. At a shear rate of 20 1/s, the viscosity was ~1.2 mPa·s for CNC-LS and ~1.5 mPa·s for CNC-DI. This is caused by the same shielding effect mentioned earlier, where the shielding of negative charges causes shrinkage of the EDL around the CNC rods, which reduces the viscosity. In general CNC is not very sensitive to fluctuations in pH, which is also a well-known property of the parent cellulose polymer. For CNC, this may be due to the relatively low charge density on the particles, with only 0.3 mmol/g of sulphate half ester groups on the surface. The particles would probably be more pH sensitive if the charge density was higher. At higher charge densities the rheological behaviour would also be different, and the dispersions would be more susceptible to agglomeration in response to fluctuation in electrolyte concentration.

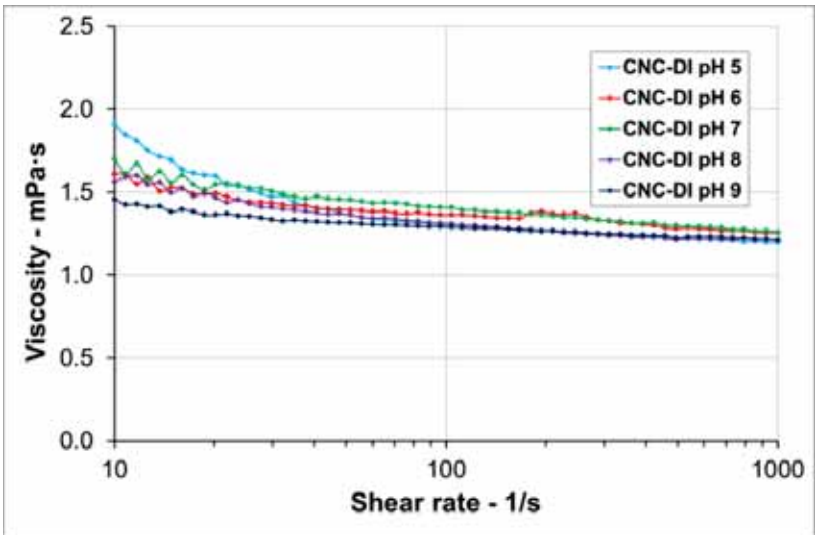

Figure 7.6: Viscosity of CNC-DI dispersions vs. shear rate, measured at 20 °C.

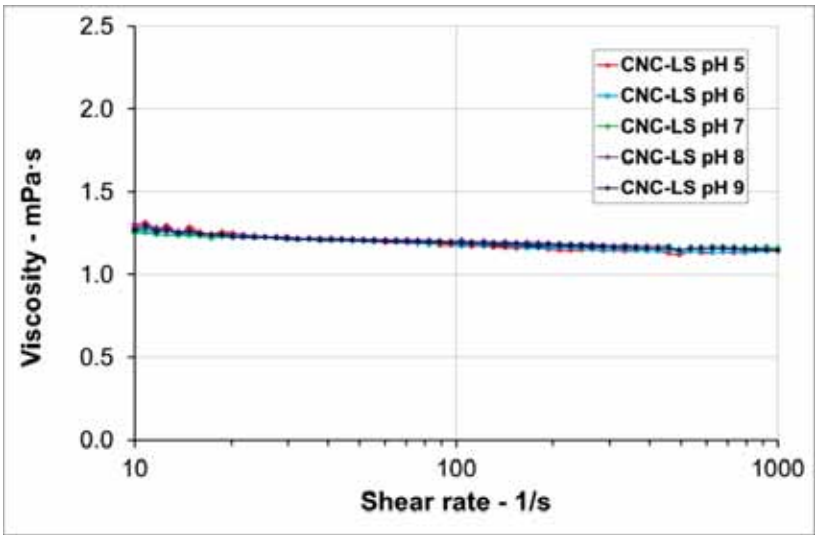

Figure 7.7: Viscosity of CNC-LS dispersions vs. shear rate, measured at 20 °C.

7.2.4 Heat aging

Introduction

Which characteristics do CNC particles exhibit when exposed to elevated temperatures? Extensive research has been performed on the temperature stability of CNC, and it has been observed that CNC is being degraded when subjected to temperatures above 220 °C (Chen et al., 2016). It should be noted that these values for CNC are acquired through thermogravimetric analysis (TGA), which is performed on dried CNC in an inert atmosphere of N_2 gas (N. Wang et al., 2007). For aqueous dispersions, the situation, as well as degradation temperature, will be different.

When applied in an oil reservoir, dispersed CNC will be subject to elevated temperatures. Reservoir temperature rises with increasing depth, or closeness to the Earth's mantle. This varies with the geothermal gradient, but a general rule of thumb is that the temperature is increased with 3 °C per 100 m depth, with temperatures reaching above 150 °C (Beal, 1946; Jahn et al., 2008a). The reservoir mineralogy affects the flooding brine chemistry, and it has been experimentally observed in core experiments at reservoir conditions that a slightly acidic CNC dispersion increased its pH after being flooded through a sandstone core (Molnes et al., 2016). At acidic conditions, cellulose may be cleaved through a hydrolysis reaction at the 1-4 glycosidic bond (Battista, 1950), but as the pH values in sandstone reservoirs typically varies between 6 and 9, acid hydrolysis will most likely not be the major pathway of CNC degradation. Cellulose derivatives have been shown to degrade very slowly under alkali conditions, but for this situation to occur, the temperatures should exceed 170 °C (Wellington, 1983). Thus, the most likely pathway for CNC degradation below 150 °C in an oil reservoir would be through radical, oxidative/reductive depolymerisation (ORD). In such reactions, a free radical containing one or more unpaired electrons can attack polymers, causing depolymerisation. Biopolymers are especially vulnerable to autoxidation, where H_2O_2 radicals are formed, leading to propagating chain reactions (Heggset et al., 2017; Wellington, 1983).

Several experiments were performed to investigate the effect of prolonged exposure to elevated temperature. The tests were divided into static heat aging using a heating cabinet for given periods of time, and dynamic heat aging,

where the particles were subjected to shear forces at given intervals during heat aging.

Aging at 120 °C for 24, 48 and 168 hours

Dispersions of 2.0 wt. % CNC-DI and CNC-LS were poured into Schott bottles. One set of bottles were tested right away, without temperature exposure, using pH and viscosity measurements, as well as visual inspection. The aged dispersions were rheologically tested at 20 °C after 24 hours, 48 hours and 168 hours. A set of samples of both CNC-DI and CNC-LS were also heat aged at 90 °C for 168 hours. Shown in Figure 7.8 is the colour development of the 120 °C heat aged dispersions.

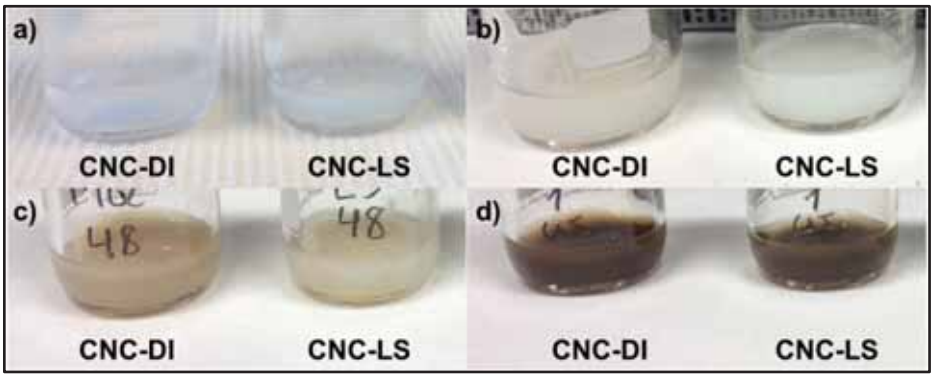

Figure 7.8: Visual evaluation of CNC samples after aging at 120 °C. a) Shows CNC-DI and CNC-LS dispersions right after sample preparation (t = 0). b) Samples after 24 hours. CNC-DI is slightly darker than CNC-LS. c) Samples after 48 hoursThe CNC-DI sample is still more miscoloured than the CNC-LS sample. d) Samples after168 hours. It was not possible to distinguish between the samples, due to heavy discolouration in both samples.

As observed in Figure 7.8, the dispersions exhibited discolouration with time, and the CNC-DI samples were discoloured slightly faster than the CNC-LS samples. The samples aged at 90 °C did not show any significant colour change. Change in colour is a sign of carbohydrate degradation, and is an important parameter to include when assessing carbohydrate stability. The degradation mechanism leading to the colour change has not been thoroughly clarified yet (Matsuo et al., 2012), but a likely candidate is thermal oxidation, which occurs due to presence of oxygen. This reaction forms both aldehyde and carboxyl groups, and formation of carbonyl groups within the cellulose chains might be the cause of the very clear colour change with time and

temperature (Łojewska et al., 2007; Yatagai & Zeronian, 1994). As CNC is derived from wood, the material might contain small amounts of pentose in addition to hexose monomers. These are known to degrade through hydrolysis into furfural and hydroxymethylfurural (HMF) respectively, when being subjected to heat and acids (Dunlop, 1948). The concentration of HMF/furfural can be determined through UV-vis spectroscopy, as they both have an absorbance spectrum of 277 nm. UV-vis was performed by Heggset et al. (2017) on CNC from the same production batch as the ones used for this thesis work, heat aged at 140 °C for three days. They found a HMF/furfural concentration of 1 mg/L, which was substantially lower than the values for the other carbohydrate polymers tested in the article. The low HMF/furfural value was connected to the crystalline nature of CNC, making it degradation resistant (Heggset et al., 2017).

The pH of the samples was also measured for each given period of time, and is given in Table 7.3 and Table 7.4.

Table 7.3: pH change over time for 2.0 wt. % CNC dispersions samples aged at 120 °C**.**

Sample	pH t = 0 h	pH t = 24 h	pH t = 48 h	pH t = 168 h	Δ pH (168 h)	H^+ formed in ‰ of glucose units, (120 °C, 24 h)
CNC-DI	6.2	2.0	2.1	2.0	4.2	83
CNC-LS	5.3	2.1	2.1	2.0	3.3	83

Table 7.4: pH change for 2.0 wt. % CNC dispersions aged 168 hours at 90 °C**.**

Sample	pH t = 0 h	pH t = 168 h	Δ pH (168 h)	H^+ formed in ‰ of glucose units (90 °C, 168 hrs)
CNC-DI	6.6	2.7	3.9	17
CNC-LS	5.8	3.1	2.7	7

The pH of the CNC-LS samples started out lower than the CNC-DI samples. This effect has been observed earlier, and a hypothesis is that it is caused by sodium ions exchanging hydrogen ions as co-ions to the sulphate ester groups, so the pH in the dispersion decreases as H^+-ions are being released into the

dispersing medium (Molnes et al., 2016). All samples experienced a decrease in pH, and calculated as the amount of H^+ released per 1000 glucose units, this number was the same for both samples aged at 120 °C, but substantially lower for the samples aged at 90 °C as expected. For the samples aged at 120 °C, this effect was observed already after 24 hours, and there were almost no changes during the rest of the testing period. As mentioned, during the degradation process carboxyl groups are formed through both oxidation and hydrolysis reactions on the material, and this is probably the cause of the reduction in pH. Change in pH can thus also be used as an indicator for temperature degradation of CNC. Similar results for both pH and colour change was obtained in an earlier study (Heggset et al., 2017), and thus supports this view. In the Heggset et al. article, the number of H^+ units formed in ‰ of glucose units at 140 °C was estimated to be 400. The release of H^+ can be caused by desulphation of the CNC. Released sulphuric acid can act in two different ways to catalyse the removal of ring hydroxyl groups; either by directly catalyse the removal of water, or by esterification of the surface hydroxyl groups of the CNC, which again will remove more sulphuric acid (Julien et al., 1993; Roman & Winter, 2004).

Further on, the samples were tested rheologically at 20 °C by using increasing shear rates and a 2° cone-and-plate setup. These results are shown in Figure 7.9 and Figure 7.10. As observed in the figures, the shear viscosity profile of both CNC in LS brine and DI water increased radically after only 24 hours of aging at 120 °C. The viscosity profile remained stable after aging for 168 hours at high temperature. The CNC-LS sample that was aged for the longest time at 120 °C was also the one that showed the highest viscosity. The increase in viscosity may be caused by a type of delamination of the CNC crystallites, which causes an increase in the surface area of the particles, and exposes more hydroxyl groups to the surrounding medium, causing an increase in viscosity. The heat aged dispersions also showed the typical rheological behaviour for liquid crystalline polymers in dispersion, with viscosity profiles displaying three distinct regions of flow. These flow regions have been investigated earlier using small angle neutron scattering (SANS) (Orts et al., 1998). The first region is seen at very low shear rate, where a shear thinning is observed due to flow of particle domains. At intermediate shear, these domains are broken up and the flow curve exhibits a plateau.

When the shear rate is increased further the individual rods in the dispersion are aligned and start to flow, leading to a secondary shear thinning behaviour.

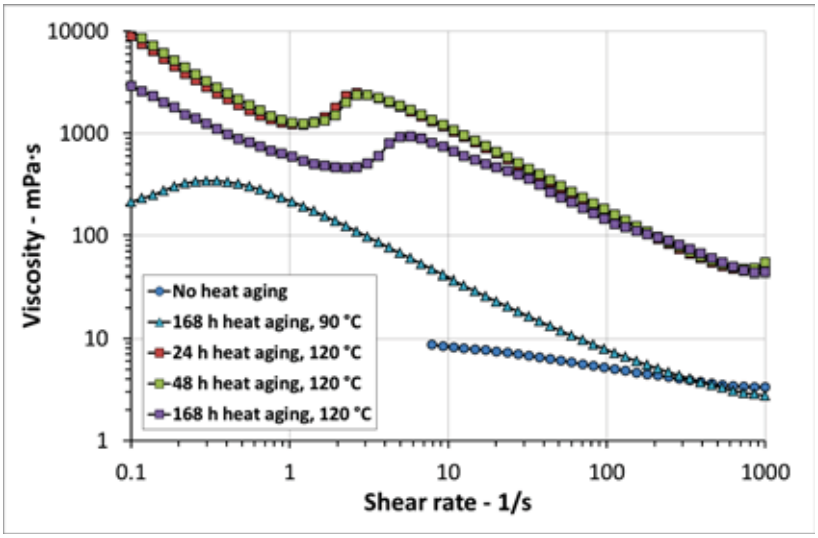

Figure 7.9: Viscosity measurements of CNC-DI, performed at 20 °C on 2.0 wt. % samples after heat aging at different temperatures.

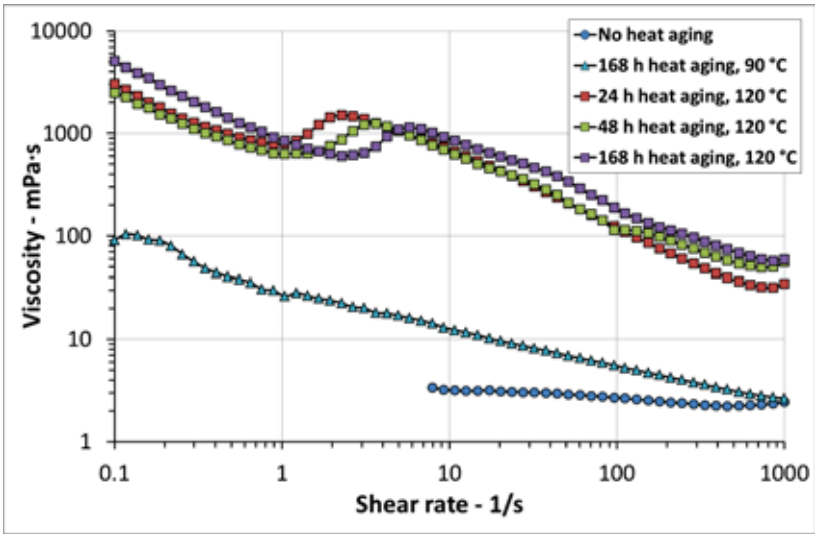

Figure 7.10: Viscosity measurements of CNC-LS, performed at 20 °C on 2.0 wt. % samples after heat aging at different temperatures.

For the measurements shown in Figure 7.9 and Figure 7.10, the first region is observed at shear rates from 0.1 to 1.0 1/s, before the plateau region forms between 1.0 and 10 1/s. The last shear thinning region is observed from 10 to 1000 1/s, in accordance with earlier observations (de Souza Lima & Borsali, 2004; Marchessault et al., 1961). The viscosity profiles for the samples aged at 90 °C for 168 hours (also shown in Figure 7.9 and Figure 7.10) showed a generally lower viscosity, and did not distinctly display the three before mentioned shear regions, although the overall profile was shear thinning. These results indicate that a certain temperature and aging period is required to obtain this dramatic increase in shear viscosity. This effect might be beneficial in an EOR perspective, as increased temperature and particle retention in the oil reservoir may lead to the same viscosity increase in the dispersions. This can reduce viscous fingering of the waterfront, as well as promote microscopic flow diversions through a log-jamming mechanism in the pore throats (T. Skauge et al., 2010), and thus lead to better tertiary oil recovery. A more detailed understanding of the observed temperature effects is thus needed before CNC particles can be approved for reservoir injection.

Dynamic time and temperature

To further investigate the effect of using LS brine as a dispersing medium, as well as the observed increase in viscosity with time and temperature, the samples were subjected to a shear-rest regimen combined with heat aging, using the rotational rheometer as described in Section 6.2.1. First, both CNC-DI and CNC-LS samples were tested for 50 hours at 90 °C, and the results are shown in Figure 7.11 and Figure 7.12. As observed for the CNC-DI in Figure 7.11, the viscosity increases quite rapidly for approximately 10 hours, before declining gradually when approaching 50 hours of run-time. A decrease in viscosity may be a sign of polymer degradation, where the chains are hydrolysed into single molecules, due to the mechanisms mentioned earlier. An interesting effect was seen for the CNC-LS dispersions in Figure 7.12. It can be observed from the figure that the viscosity continued to increase right up to the 50 hours mark. The measurements were also much more coherent, and the samples displayed a thixotropic behaviour while under shear. The increase in viscosity is probably a side effect of a gradual degradation of the crystallites, or breaking of agglomerates due to shear, leading to an increase in surface area, which is compatible with increase in viscosity.

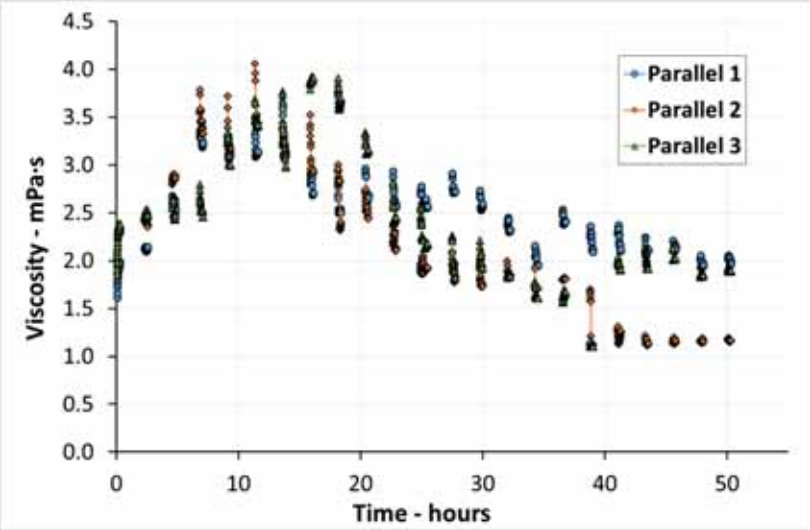

Figure 7.11: Viscosity development for a 2.0 wt. % CNC-DI dispersion, tested at 90 °C. Each point is one viscosity measurement and was performed for 15 minutes at 50 1/s, and between each such measurement the sample was rested for 120 minutes.

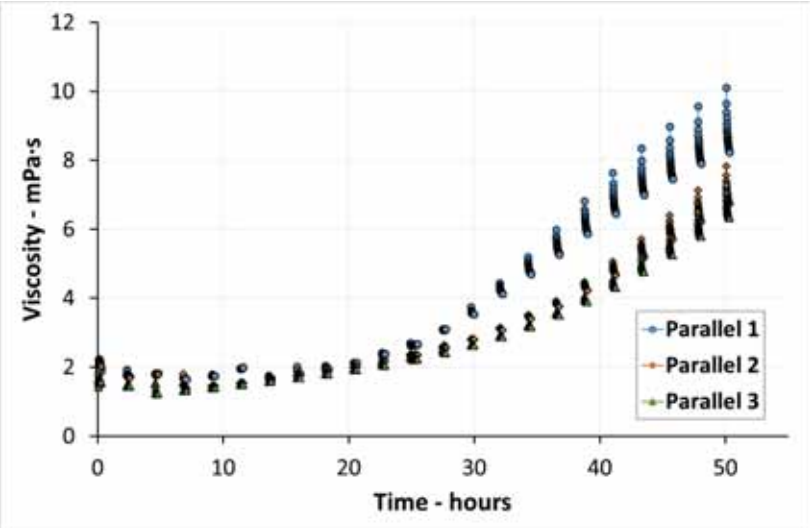

Figure 7.12: Viscosity development for a 2.0 wt. % CNC-LS dispersion, tested at 90 °C. Each point is one viscosity measurement and was performed for 15 minutes at 50 1/s, and between each such measurement the sample was rested for 120 minutes.

The pH also decreased (shown in Table 7.5), which might be an indication of elimination of sulphate groups from the particle surfaces, which can further lead to crystallite degradation. The amount of H^+ released per 1000 glucose monomers was low and relatively similar for the two samples.

Table 7.5: The in pH in 2.0 wt. % CNC-DI and CNC-LS before and after dynamic heat aging at 90 °C.

Sample	pH t = 0 h	pH t = 50 h	Δ pH	H^+ formed in ‰ of glucose units (90 °C)
CNC-DI	6.4	5.0	1.4	0.1
CNC-LS	5.4	4.7	0.7	0.1

When comparing the formed H^+ per 1000 glucose units for the samples tested at 90 °C and 120 °C, it is interesting to observe that there is such a large difference in released hydrogen ions. At 90 °C, only ~0.1 H^+ is formed per 1000 glucose monomers, while at 120 °C, the number is 83. When the temperature is increased to 140 °C, 400 ‰ H^+ is formed (Heggset et al., 2017). According to these results, the lower temperature limit for sulphate half ester cleavage would be in the 90 – 120 °C range. The relatively high temperature is probably the main cause leading to the before mentioned degradation processes, as the shear rate used in the experiment (50 1/s) was rather low. The shear rate in a core flooding with a standard flow rate of 4 PV/day would be even lower, so shear degradation should generally not be a problem for the crystallites in question.

In the next step, two experiments were performed to investigate how long time it would take to bring the CNC-LS samples towards viscosity equilibrium, as was observed for the CNC-DI samples already after 50 hours at 90 °C (Figure 7.11). 0.5 and 2.0 wt. % samples of CNC-LS were subjected to 175 hours of the dynamic aging regime, with alternating 15 minutes of shear at 50 1/s and 120 minutes of no shear. The results are shown in Figure 7.13. The viscosity increased steadily with time for both tested concentrations, and the results were in line with the experiment performed for 50 hours. The viscosity of the 2.0 wt. % sample increased until the top viscosity peak at around 130 hours, before the viscosity started to decline and stabilise. The viscosity development of the 0.5 wt. % sample was slightly lower, due to the

lower CNC concentration. The viscosity increased until 150 before it stabilised.

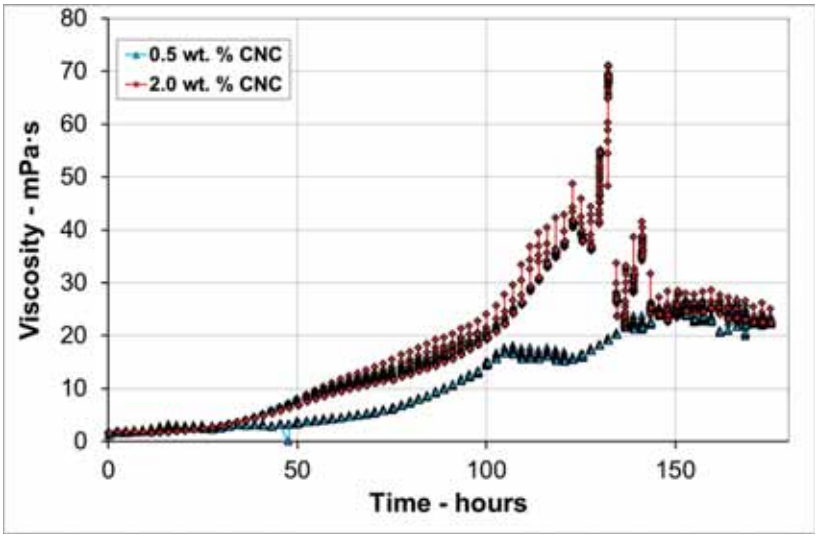

Figure 7.13: Long time heat aging experiment at 90 °C for 0.5 and 2.0 wt. % CNC-LS.

In both samples there was observed a small pH decrease, as shown in Table 7.6.

Table 7.6: The pH in 0.5 and 2.0 wt. % CNC samples before and after the long-term shear-rest measurements.

Sample	pH t = 0 h	pH t = 175 h	Δ pH	H^+ formed in ‰ of glucose units (90 °C)
0.5 wt. % CNC-LS	5.4	4.7	0.6	0.5
2.0 wt. % CNC-LS	5.5	4.4	1.1	0.3

The decrease in pH is, as mentioned, probably due to sulphuric acid released from the surface of the CNC at elevated temperatures, leading to self-catalysed depolymerisation (Roman & Winter, 2004). When the CNC particles starts to delaminate, the surface area of the dispersed particles will increase, thus leading to an increase in viscosity up to a certain point were the material is broken down to such an extent that the viscosity building effect is lost.

The reason why the brines containing NaCl shows better long term temperature stability than the brines with DI water can be caused by the existence of chloride anions (Cl^-) in the dispersion. Cl^--anions are known to create competition between hydroxyl radicals and organic matter, as shown in Equations 7.2 and 7.3. This leads to inhibition of oxidation reactions, which is one of the proposed degradation routes for CNC.

$$\bullet OH + Cl^- \leftrightarrow HOCl^{-}\bullet \tag{7.2}$$

$$HOCl^{-}\bullet + H^+ \rightarrow Cl\bullet + H_2O \tag{7.3}$$

The chloride ions may also interact with the hydroxyl radicals, and in that way compete with the organic material for the radical compounds, and in that way slow down the oxidation rate of the dispersed CNC. Chloride ions are thus preventing CNC degradation both through complexion and radical scavenging (Liao et al., 2001; Lu et al., 2005).

7.3 Atomic force microscopy

To further investigate the effects of heat aging, atomic force microscopy (AFM) was used to image the CNC crystallites, both before and after heat aging at 90 and 120 °C. Figure 7.14, shows diluted, non-aged CNC particles dispersed in DI water (as a reference point to the images of aged sample dispersions). The crystallites are slightly rounded and intact, although they show some aggregation behaviour. It is difficult to decide whether this effect has been caused by the drying method (compressed N_2) used during sample preparation, or if the crystallites are partly aggregated in dispersion.

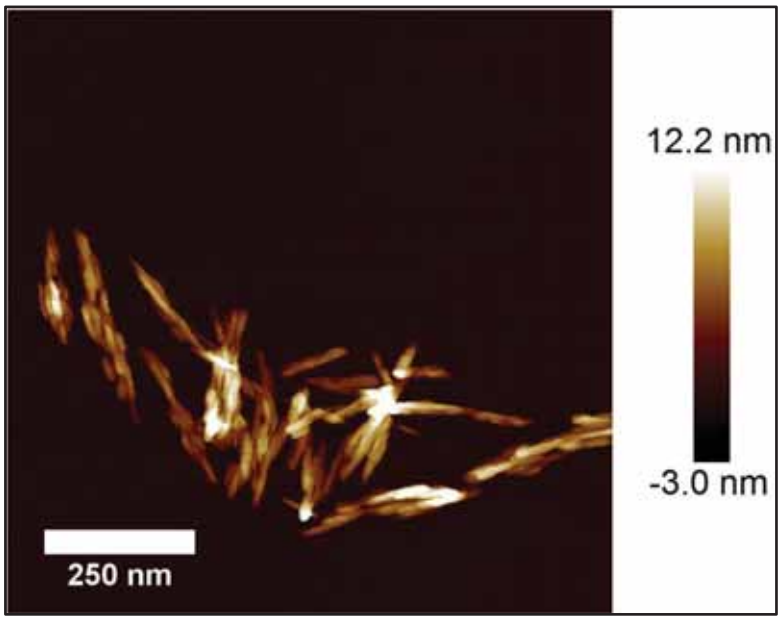

Figure 7.14: CNC crystallites dispersed in DI water and deposited onto a mica disc before rinsing with DI water to dilute the sample. The bar shown on the right indicates the height of the particles.

In Figure 7.15 – Figure 20, CNC dispersions before and after heat aging at 90 and 120 °C are shown. Prior to heat aging, in Figure 7.15 and Figure 7.16, the crystallites looks quite like the non-aged crystallites in Figure 7.14, although

the sample in Figure 7.14 was dispersed in DI-water and the samples in Figure 7.15 and Figure 7.16 were dispersed in LS-brine. It is difficult to determine anything about eventual agglomeration, due to the crystallite concentration on the mica being too high. Figure 7.17 and Figure 7.18 shows CNC-LS dispersions after one week of heat aging at 90 °C. Here the crystallites appear changed, or spiky, which may be an indication of beginning polymer degradation. This is in agreement with the large increase in viscosity observed for the same dispersions during viscosity measurements. When diluted, the crystalline particles seem to be agglomerated, as can be seen in Figure 7.18. A CNC-LS dispersion sample was also subjected to heat aging for one week at 120 °C, shown in Figure 7.19 and Figure 7.20. Here it is clear that the particles agglomerate, and this can clearly be seen in Figure 7.19, where the agglomerates form ribbon-like structures. When diluted and magnified, as seen in Figure 7.20, large particle aggregates was observed. These observations are in accordance with the flow regime seen in Figure 7.9 and Figure 7**.10**, where the crystallites are shown to flow in domains or agglomerates at low shear, before breaking up at higher shear rates. These results confirm that CNC particles do not degrade into glucose monomers, but keeps their crystalline form within the time frame and temperatures investigated. If the viscosifying and dispersing effects observed in this section and in the earlier experiments could be controlled, CNC could also be used as a viscosifying additive for LS brine.

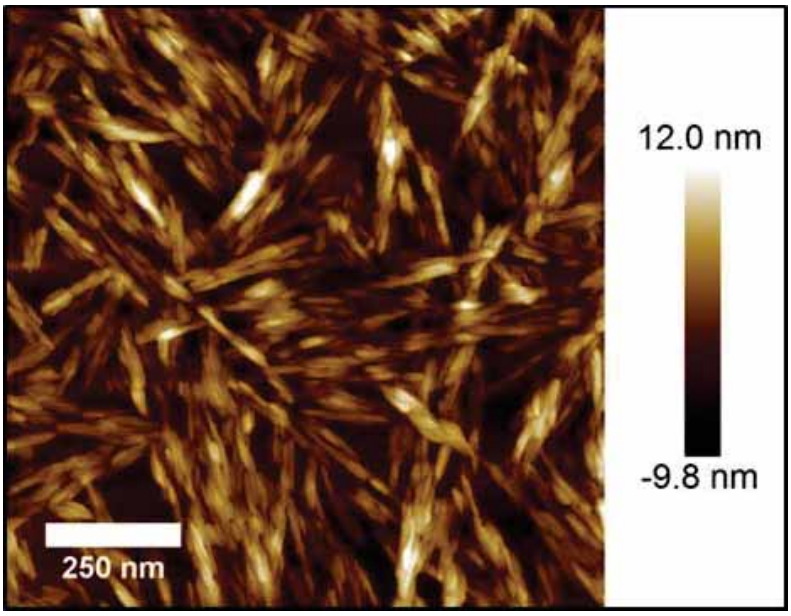

Figure 7.15: CNC dispersion in LS brine, prior to heat aging.

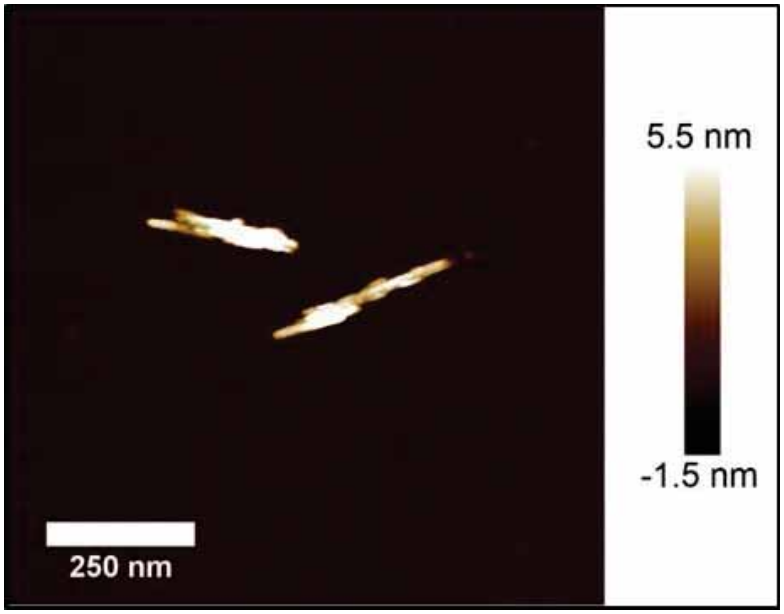

Figure 7.16: CNC particle agglomerates in LS brine prior to heat aging, diluted onto mica disc.

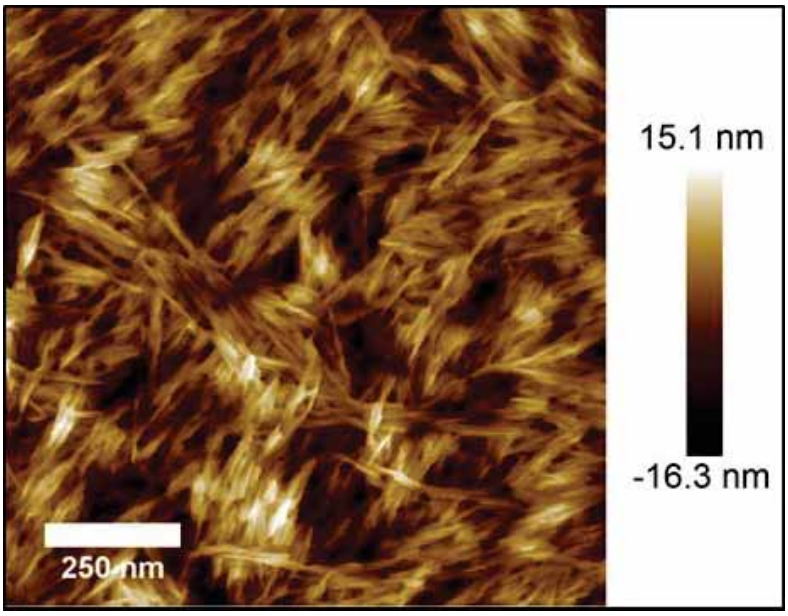

Figure 7.17: CNC dispersion in LS brine, after one week of heat aging at 90 °C.

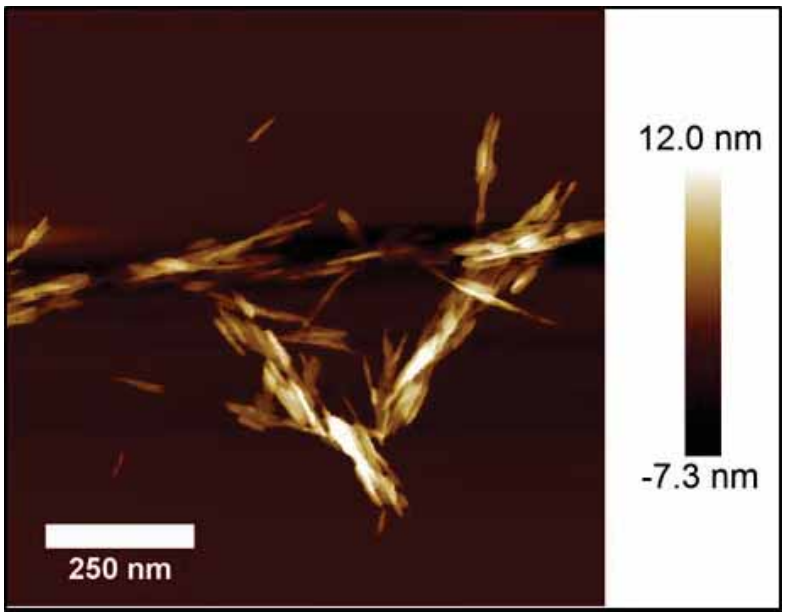

Figure 7.18: Diluted CNC agglomerates in LS brine, after one week of heat aging at 90 °C.

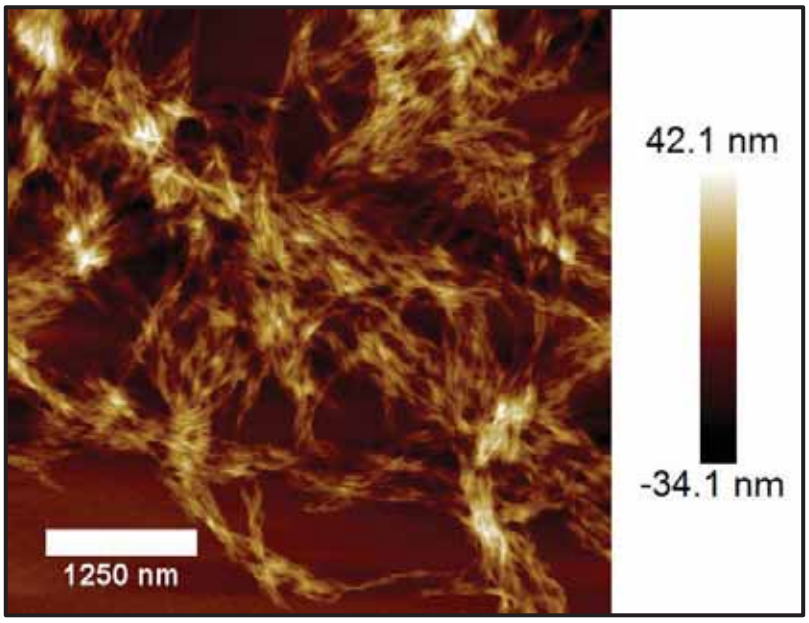

Figure 7.19: CNC dispersion in LS brine, heat aged at 120 °C for one week. Ribbon-like structures can be observed.

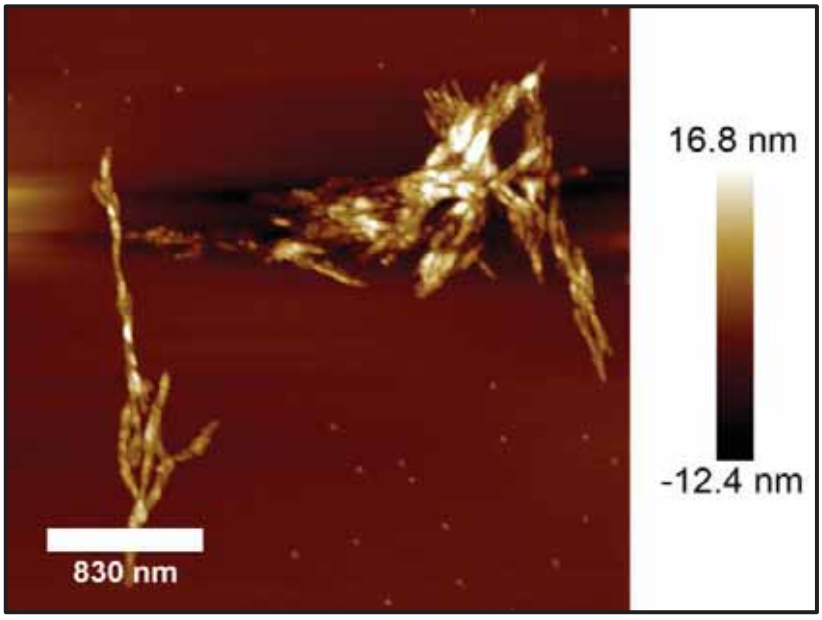

Figure 7.20: Diluted CNC agglomerates in LS brine, after one week of heat aging at 120 °C.

7.4 Core flooding

A number of different core flooding experiments were performed on outcrop sandstone cores, both with and without crude oil. The first focus was to investigate the injectivity of CNC dispersed in LS brine, and to assess the effects of increasing the weight concentration of dispersed nanoparticles, and how an increase in temperature affected the injectivity and pressure drop over the core during injection. The experiences made during the water flooding experiments were then used to tailor the parameters used in the oil recovery tests.

7.4.1 Injectivity studies and effect of increasing CNC concentration

Injectivity investigation was performed by consecutive flooding of a 100 % LS saturated outcrop sandstone core (SM8) with 0.5, 1.0 and 2.0 wt. % CNC dispersed in LS brine. The experiments were performed at ambient temperature, and effluent samples were collected and assessed throughout the entire testing. Both LS brine and CNC-LS brine with increasing CNC concentration was injected with at constant rate of 4 PV/day (0.045 mL/min). The inlet and differential pressure (dP) over the core was monitored during the entire experiment, and is shown for all CNC concentrations in Figure 7.21. Between each flooding test with CNC-LS brine, the core was cleaned and regenerated by injecting LS brine in the opposite of the testing until stable differential pressure was achieved.

The flooding experiments confirm a steady increase in differential pressure for all the CNC concentrations tested. The rise in dP was dependent on CNC concentrations, as observed in Figure 7.21, where the 0.5 wt. % CNC had the lowest dP increase, starting out at 3 mBar and ending at 7 mBar after 9.5 PV injected. As expected, the largest increase was observed for the 2.0 wt. % CNC-LS brine, with an increase from 8 – 155 mBar after 9.5 injected PV. Shear viscosity measurements were performed on effluent samples and on bulk CNC-LS samples and the results were compared. As expected, the viscosity increased with increasing CNC concentration, and the results are shown in Figure 7.22.

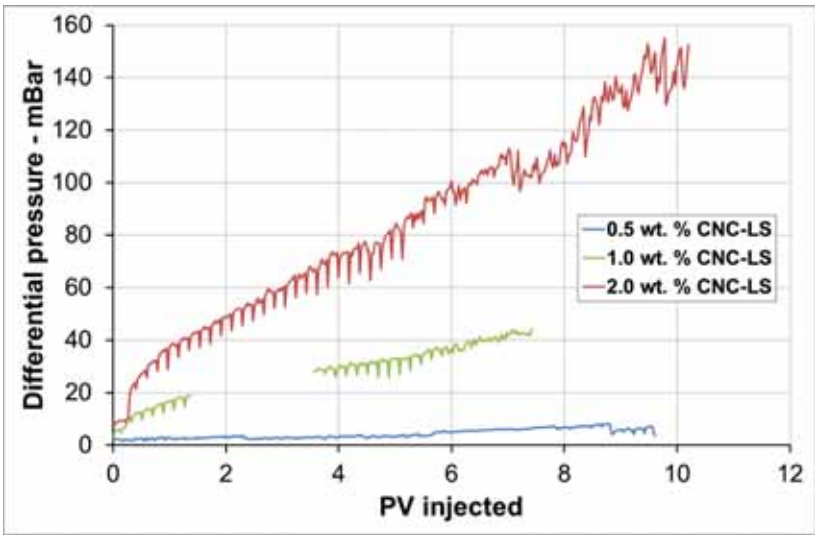

Figure 7.21: Differential pressure development as a function of injected CNC-LS brines at ambient temperature. Injection rate was 4 PV/day (0.045 mL/min). The gap in the 1.0 wt. % CNC-LS measurement was caused by computer failure, leading to 13.5 hours of differential pressure measurements being lost.

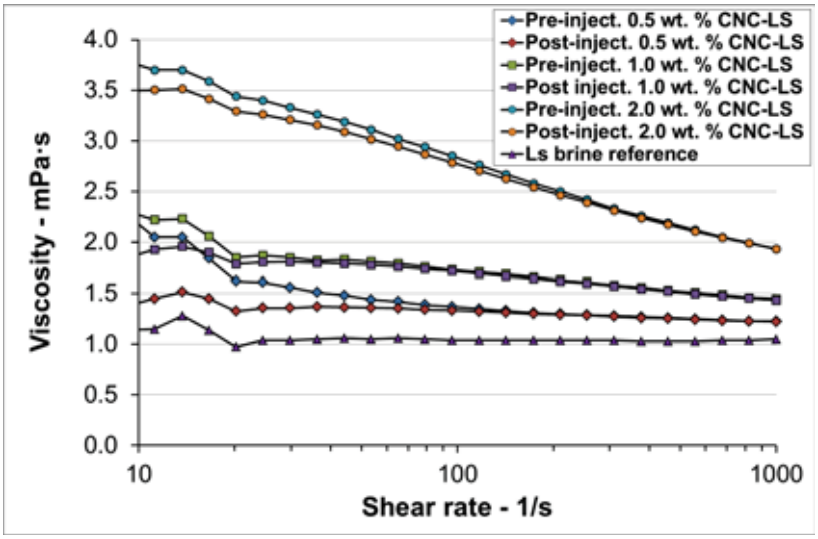

Figure 7.22: Shear viscosity of bulk samples compared to the respective effluent samples of the injected CNC-LS brines. An LS brine reference is also shown.

These results also give a good indication of the injectivity of dilute CNC dispersions. Although viscosity in effluent samples remained relatively unchanged compared to the viscosity of the bulk CNC-LS dispersion for all the injected CNC-LS concentrations, the increase in dP indicates that some of the CNC crystallites becomes at the inlet surface of the core sample, or to a lower extent inside the core. To investigate this further, permeability (K, mD) measurements were performed before and after each flooding experiment with LS brine at a flow rate of 2 mL/min. After 1.0 wt. % CNC and 2.0 wt. % CNC the flow was also reversed to test if larger CNC particles were filtered on the core inlet surface. The results are shown in Table 7.7.

Table 7.7: Overview of core permeabilities after forward and reverse flooding of LS brine with elevated injection rate (2 mL/min) and stabler differential pressure

Core permeability (mD) after	Initial LS brine	0.5 wt. % CNC-LS	1 wt. % CNC-LS	2 wt.% CNC-LS
$K_{forward}$	210	161	106	73
$K_{reverse}$			139	96

The initial permeability of the core was 210 mD. After flooding with 0.5 wt. % CNC-LS brine the permeability was reduced to 161 mD. After the 1.0 wt. % CNC-LS injection the permeability was further reduced to 106 mD. Injection of LS brine in reversed direction removed trapped CNC crystallites from the inlet surface and caused the permeability to increase to 139 mD. Flooding with 2.0 wt. % CNC-LS brine reduced the permeability further to 73 mD. Again, reverse injection of LS brine improved the permeability, this time to 96 mD. These results confirm that some sort of filtration of CNC particles occurs at the inlet surface of the core. Although some of the permeability is restored after reverse injection, the initial permeability is not completely restored, implying that some CNC crystallites is retained inside the core, or is still caught on the core inlet.

Flooding activity also had an impact on the pH of the CNC-LS effluent samples. When CNC is dispersed in DI water, the pH remains in the neutral region, but when electrolyte, like NaCl, is added, the pH drops. This may be due to H^+ release into the dispersion as sodium ions excludes it as counterion to the sulphate half ester groups on the CNC-particles. This effect was

observed when the pH of the CNC-LS brine was measured before the injectivity testing. However, after being flooded through the core, the dispersion brine showed an increase in pH, for all the CNC-LS concentrations used, as shown in Figure 7.23.

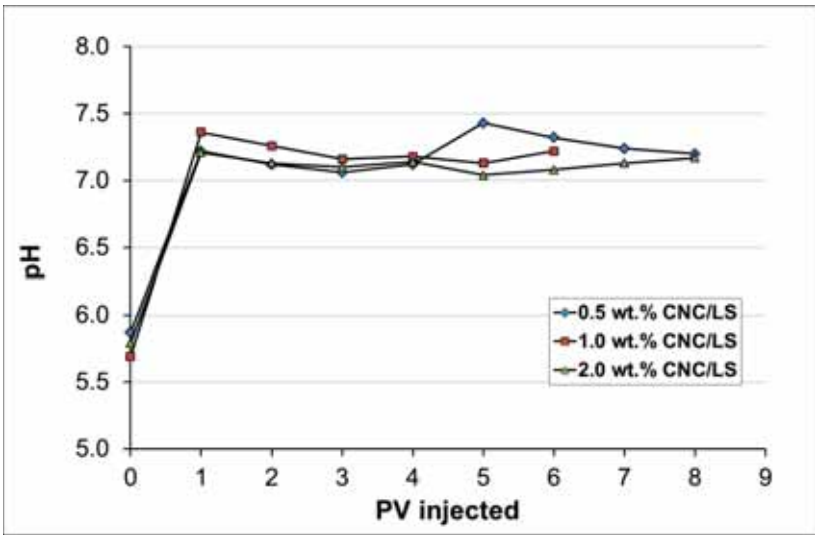

Figure 7.23: pH change in CNC-LS measured for each injected pore volume. The bulk CNC-LS pH was 5.9, 5.7 and 5.9 for 0.5, 1.0 and 2.0 wt. % CNC, respectively.

An increase in effluent pH of around 1.5 pH units was observed for all the tested CNC-LS concentrations. The increase was immediate, and remained relatively stable throughout the experiments. This is a known effect when flooding LS brines through sandstone, and is caused by formation of excess OH^-, which is due to ion exchange with the clay or feldspar mineral surfaces in the core material (T. Austad et al., 2010).

It was possible to visually verify some changes in the CNC-LS effluent samples. As observed in Figure 7.24, the effluents became somewhat more "opaque" as the LS brine was displaced by the CNC-LS brine dispersion. At low concentrations, CNC exhibits a "mother of pearl"-like appearance that is very easy to recognize, and this was observed in the effluent.

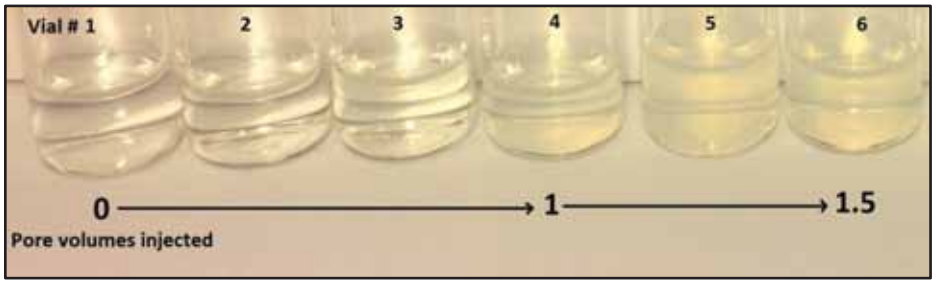

Figure 7.24: Visual inspection of the effluent of 1.0 wt. % CNC-LS brine.

As observed in Figure 7.24, vial 1 shows the first effluent collected after changing injection fluid from LS brine to 1.0 wt.% CNC-LS. As each vial originally contained 4 mL effluent and the PV of the core was 16.2 mL, vial number 4 is the effluent collected after ~1 PV, and vial number 6 equals ~1.5 PV. The breakthrough of CNC from the core can be observed after flooding approximately 1 PV CNC-LS brine.

The conformity of the measured effluent viscosities confirms that the CNC-LS brine is injectable into the sandstone core, and that most of the material travels through the core. The visual inspection of the effluents was a further verification of the injectivity of dilute CNC-LS dispersions.

7.4.2 Effect of increasing temperature

Based on the differential pressure observations in the core injectivity tests, it was decided to continue using a 0.5 wt. % CNC-LS brine dispersion in the further investigations. At this CNC concentration, the increase in differential pressure was low, and the particles still had a sufficient viscosifying effect to separate it from LS brine and DI water through simple viscosity measurements.

To investigate the temperature effect on the injectivity, CNC-LS brine dispersion was injected at constant temperatures into a 100 % LS saturated outcrop sandstone core SM8 with an injection rate of 4 PV/day. The inlet pressure and differential pressure over the core was monitored throughout the whole experiment and effluent samples were collected. In between each experiment, the core was cleaned by injection of LS brine in the opposite

direction, until stable pressure drop. Experiments were performed at increasing temperature steps, namely 60, 90 and 120 °C.

The core flooding at 60 °C had an initial dP of 6 mBar (100 % LS brine saturation), and the pressure drop gradually increased to 15 mBar after 1 PV injected, as observed in Figure 7.25. After 7 PV the dP had increased to 60 mBar.

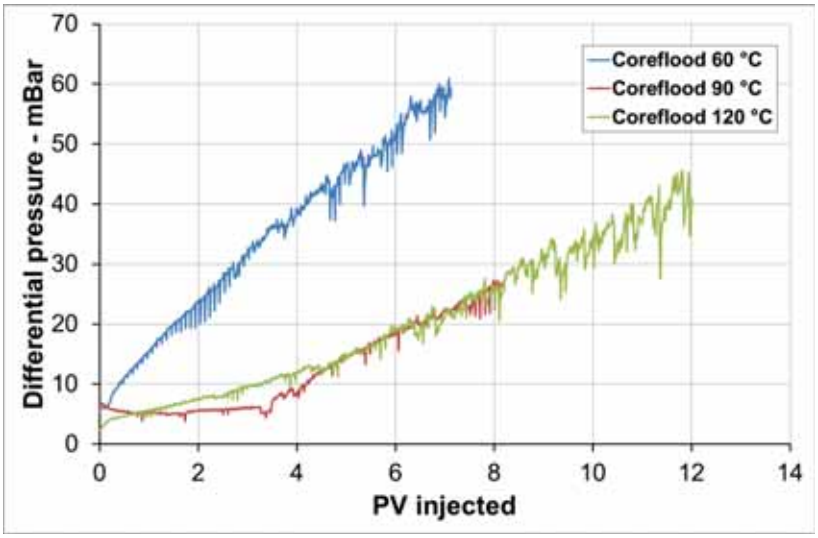

Figure 7.25: Differential pressure as a function of injected pore volumes (PV) during injection of 0.5 wt. % CNC in LS brine into a 100 % LS saturated sandstone core. Injection rate was 0.045 mL/min (4 PV/day).

Viscosity measurement on effluent samples exhibited only a very small reduction in the viscosity of the CNC-LS dispersion, confirming that mostly all CNC particles are being transported through the porous media, and the main part of the pressure build-up can be linked to the filtration of the largest fraction of CNC particles at the inlet surface. The effluent viscosity measurements are shown in Figure 7.26.

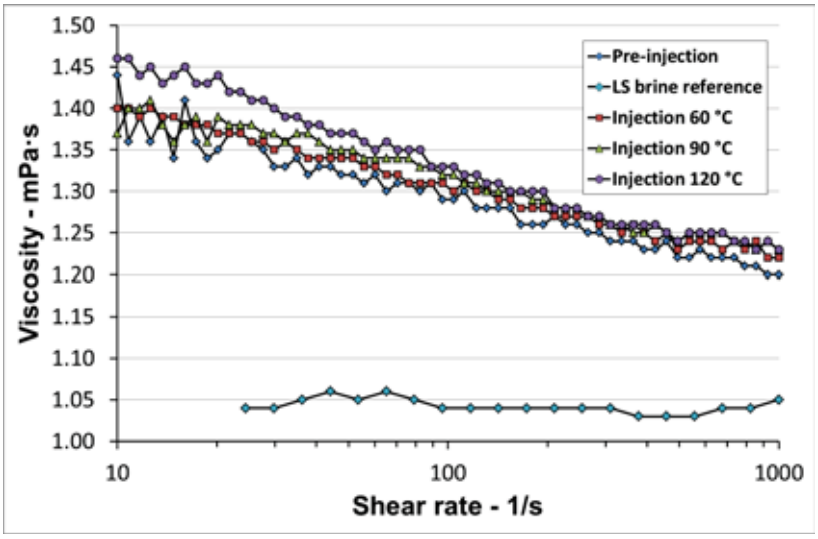

Figure 7.26: Viscosity at 20 °C of 0.5 wt. % CNC in LS brine samples before injection and in effluent samples after injection into core SM8 at 60, 90 and 120 °C.

The sandstone core sample (SM8) was regenerated for the next test by flooding the core with LS brine in reversed direction, to remove CNC particles from inside the core and from the inlet surface. LS brine flooding confirmed only small changes in core permeability on the regenerated core. The CNC-LS flooding test was repeated at both 90 and 120 °C, and the pressure build-up effects are presented in Figure 7.25.

Less pressure build-up is observed at 90 and 120 °C, compared to 60 °C. The viscosity of effluent samples at 90 and 120 °C are also in line with the effluent viscosity at 60 °C, confirming that the major part of the viscosity-contributing CNC particles are transported through the porous media at all tested temperatures, indicated in Figure 7.26. At a shear rate of 10 1/s, the effluent viscosity at 60, 90 and 120 °C is close to 1.40 mPa·s, while the viscosity of the bulk dispersion is 1.45 mPa·s. There was no increase in viscosity after exposure to elevated temperatures during core flooding, which is an effect that has been observed earlier on heat aged CNC-LS dispersions (Molnes et al., 2017). A possible explanation for this is that the particles are not trapped in the pore matrix long enough for the earlier observed viscosity increase to take place. At an injection rate of 4 PV/day, a CNC particle will use approximately 6 hours to travel through the length of the core. Earlier heat aging experiments

have revealed that this increase in viscosity is not observed before the dispersion has been aged for at least 20 hours (Molnes et al., 2017). On lab scale, the time frame is thus too short to observe these changes, but on oil reservoir scale, there is a possibility that this heat viscosifying effect may support the oil recovery process. The low initial viscosity of the CNC-LS brine dispersion gives a better injectivity than for higher viscosity polymer injection fluids. Thus, if the size distribution of the particles can be controlled, this time/temperature dependent viscosifying effect may offer an advantage over conventional flooding polymers like HPAM.

The core permeability in the different experiments is given in Table 7.8. Permeability values in mD were calculated by using the Darcy equation (Eq. 2.1) in Section 6.2.5.

Table 7.8: Core permeability (SM8) after core cleaning/core regeneration, and prior to injectivity tests (1) at 60, 90 and 120 °C. Permeability 2 indicates the calculated values between measurements, after regeneration.

Temperature, °C	Permeability 1, mD	Permeability 2, mD
60	62.7	43.9
90	43.9	75.3
120	75.3	68.3

As was observed after the 90 °C CNC-LS injection, the permeability of the core sample was increased. This was not expected, as earlier injection studies with CNC-LS generally exhibited a decrease in permeability, due to particles trapped inside the porous medium and on the inlet surface of the core (Molnes et al., 2016). The reason for this effect may be a beginning degradation of CNC trapped in the porous media. Prolonged exposure to high temperatures can change the surface chemistry of the CNC (Molnes et al., 2017), and this change may lead to desorption/un-jamming of trapped CNC. Combined with an elevated injection rate between the measurements, the CNC particles are probably expelled from the core sample.

The increase in differential pressure over the core SM8 is mainly caused by filtering at the core inlet, but some adsorption on pore surfaces or jamming in pore throats cannot be excluded. As earlier mentioned, the CNC particles are negatively charged, due to the sulphate half esters substitutions on their

surfaces through the production process. Silicate minerals at the pore surfaces are also negatively charged in this pH range, which excludes electrostatic adsorption.

The pH values in the effluent samples were also tested. It is known that brine pH of non-buffered systems can increase when flooded through sandstone, due to a cation exchange reaction with pore surface minerals, where H^+ exchange with cations at mineral surfaces (T. Austad et al., 2010). The bulk pH of the CNC-LS brine was 5.7, as shown in **Table 7.9**. The pH value observed in CNC-LS effluent samples at 60, 90 and 120 °C confirmed a Δ pH of 1.7, 1.5 and 1.1 respectively. The results are in agreement with reduced pH changes during LS brine injection in sandstone cores at increasing temperatures (Piñerez Torrijos et al., 2016).

Table 7.9: pH development in 0.5 wt. % CNC in bulk LS brine before, and effluent samples after core flooding at 60, 90 and 120 °C.

Initial bulk pH	pH after 60 °C	pH after 90 °C	pH after 120 °C
5.7	7.4	7.2	6.8

As observed in the table, the effluent pH still increases compared to bulk dispersion due to the reactions described previously, but the magnitude of the pH increase becomes lower with increasing temperature. This effect may be caused by formation of carboxyl groups on the surface of the CNC particles during heat degradation (Heggset et al., 2017; Molnes et al., 2017). Carboxyl groups may act as weak buffers against the released hydroxyl ions and in this way keep the effluent pH at a lower level. This observation also confirms that the CNC particles added to LS brine do not have a large effect on pH development during LS brine injection compared to earlier observations (Piñerez Torrijos et al., 2016).

7.4.3 Oil recovery experiments

The last remaining step was to investigate the potential of using CNC particles in enhanced oil recovery. It was decided to perform two EOR experiments, one at 60 °C, and one at 90 °C. These temperatures were chosen based on earlier experimental experience, from using LS brine in Smart Water

EOR experiments (Piñerez Torrijos et al., 2016), and characterisation and injectivity tests performed on CNC-LS brine dispersions.

The enhanced oil recovery experiments were performed on an outcrop sandstone core SM10. The core was restored with S_{wi} = 20 %, and saturated and aged for 14 days in crude oil at the respective test temperatures. The oil recovery tests were performed by first injecting LS brine (secondary mode) until ultimate oil recovery plateau was reached, before a CNC-LS brine dispersion was injected in tertiary mode, targeting the residual oil inside the pore system. The results from the oil recovery test performed at 90 °C are shown in Figure 7.27.

During secondary LS brine injection, the oil recovery steadily increased, during the first 8 PV of injection, before levelling off at an ultimate recovery of 66 % OOIP. The dP gradually decreased as the water saturation in the core increased. A fluctuation in dP was observed during LS injection, which is an indication that mobile oil is moving through the pore throats. The dP fluctuation decreased when the ultimate recovery plateau was reached. 19 PV of LS brine was injected to ensure that all mobile oil was produced. When the CNC-LS brine dispersion was injected, an increase in differential pressure was observed. During the next 11 PV, 3.4 % OOIP extra oil was produced. In the same period there was also observed an increase in the dP fluctuation, which could be an indication of increased mobilisation of oil in the pore space due to the introduction of CNC particles. At the end, the injection rate was increased 4 times to 16 PV/day. Differential pressure increased significantly with increased injection rate and an extra oil production of 5.4 % OOIP was obtained.

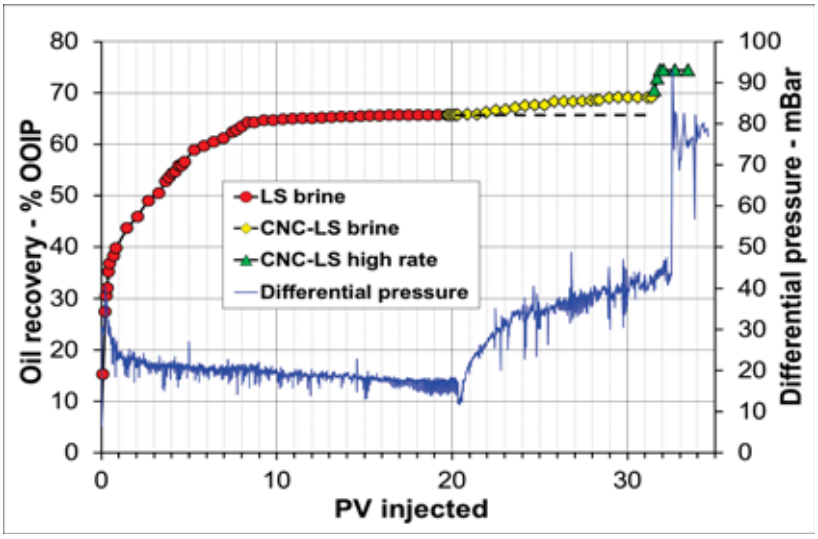

Figure 7.27: Oil recovery in % OOIP of LS brine and CNC-LS brine, injected first with a rate of 4 PV/day, and at last at 12 PV/day, all at 90 °C. The results are shown as a function of injected pore volumes (time). The differential pressure for the whole measurement is also included.

The pH of the bulk CNC-LS dispersion was 5.7, and the pH measured in sampled CNC-LS effluent was 7.4.

The increase in dP fluctuations was more pronounced in the oil recovery experiment performed at 60 °C. LS brine was injected in secondary mode, and CNC-LS brine dispersion was injected in tertiary mode. The results are shown in Figure 7.28. The oil recovery reached 40 % OOIP after 4 PV LS brine injection and continued to steadily increase to 45 % OOIP after 11 PV. Larger fluctuation in dP was observed during the whole period of LS brine injection. After 5 PV injected, the differential pressure started to stabilise and only minor amounts of oil was produced. After 11 PV, injection brine was changed to CNC-LS. At the changing point, 45.8 % OOIP was produced by LS brine injection.

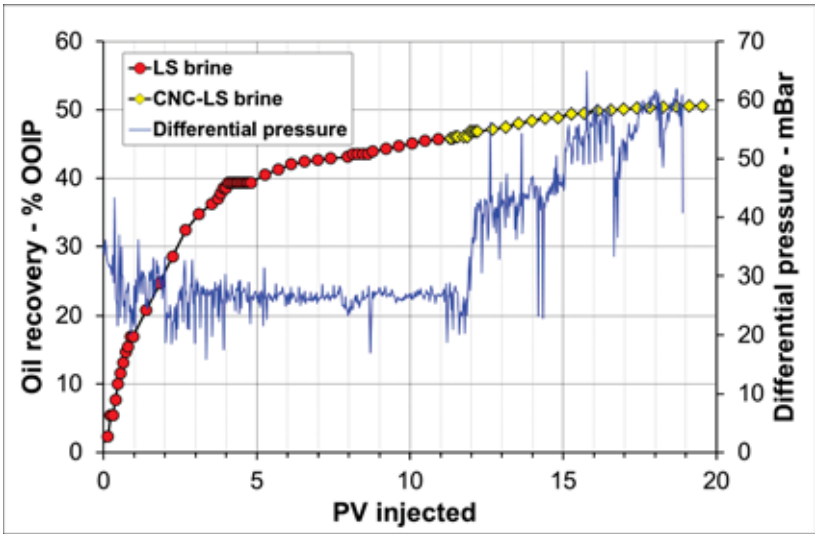

Figure 7.28: Oil recovery in % OOIP of LS brine and CNC-LS brine, injected with a rate of 4 PV/day at 60 °C, as a function of injected pore volumes (time). The differential pressure is shown as a function of injected pore volumes.

As the CNC-LS brine dispersion was injected, the differential pressure increased, and at the same time the dP fluctuation increased, as observed in the jagged line in Figure 7.27. The introduction of CNC particles into the pores space definitely affects the fluid flow in the pores, and the increased dP fluctuation could indicate log jamming of CNC particles in pore throats or remobilisation of oil. The experiment was terminated after 20 PV injected, with an ultimate oil recovery of 51 % OOIP. Table 7.10 shows the measured pH values for the bulk LS brine and CNC-LS dispersion prior to injection, and pH values of the sampled effluent.

Table 7.10: Measured pH in bulk and effluent when injected at 60 °C.

Sample	Bulk pH	Effluent pH	Δ pH
LS brine	5.8	7.6	1.8
CNC-LS	5.6	6.4	0.8

An increase in oil production was observed at both temperatures, but for the recovery experiment performed at 60 °C, it was difficult to determine if the extra oil produced was due to the CNC-LS brine dispersion or the LS brine

alone. For both experiments, an increased fluctuation in differential pressure over the core was observed in tertiary mode, which may be a sign of oil mobilisation. The increased dP fluctuation could be an indication of mobilisation of oil droplets passing through pore throats. This mobile oil will not be produced before a larger continuous oil bank is created and could be pushed out from the pore network of larger and smaller pores and pore throats.

An increase in pH was seen for the CNC-LS brine dispersion at both test temperatures, with the largest increase observed at 90 °C, with a Δ pH of 1.7. At 60 °C, the Δ pH was 0.8. The larger increase in pH at 90 °C is can be caused by the temperature catalysing mineral dissolution and ion exchange.

As discussed, the CNC particles could cause water diversion by jamming up in easily flooded pore throats (log-jamming), which could lead the water flow diversion into less available pores. The CNC particles did probably not affect the core wettability more after the secondary LS brine injection, indicated by the low pH effect compared to LS brine injection, and because the surface charges of the CNC particles and sandstone clay minerals are the same (anionic).

8 Concluding remarks and future work

In this work, cellulose nanocrystals have been thoroughly investigated for use in enhanced oil recovery in sandstones, in combination with low saline Smart Water brines. The properties of CNC particles in DI water and low salinity brine has been examined by investigating rheological properties, salt and pH stability, and effects of heat aging, to be able to prepare brine dispersions with optimal properties for sandstone core sample injection.

Injectivity studies were performed on outcrop sandstone core samples, and the effects of increasing the CNC concentration and injection temperatures were investigated.

8.1 Characterisation and temperature stability

8.1.1 Dispersion stability

- **Salt stability:** When electrolytes are added to an aqueous CNC dispersion, it causes a lowering of the zeta-potential and viscosity, due to shielding of sulphate ester groups on the surface of the nanocellulose particles. The shear viscosity of cellulose nanocrystal dispersions decreases when exposed to counterions like Na^+. Sodium ions shield the negatively charged sulphate half ester groups on the surface of the particles, leading to shrinkage of the EDL. This lowers the viscosifying effect of the charged particles due to increased interaction between the particles. The electrolyte concentrations used in this study did not cause the CNC particles in question to aggregate, as the absolute zeta-potential value remained larger than ± 30 mV throughout the study. This is above the critical value for the colloidal stability of dispersions, and the particles will be dominated by repulsive forces and thus remain dispersed. It is important to avoid particle aggregation, to preserve the injectivity of the CNC dispersions.

- **Effect of pH:** Measurements performed with Zetasizer showed that the CNC dispersion stability was not affected by changes in pH. It should be mentioned though, that the pH values tested were from slightly acidic (~5) to the basic range (~9), for which the crystallites remained stable in dispersion. The pH values were chosen due of the intended application of the dispersions, which is enhanced oil recovery. The pH in oil reservoirs will never reach extreme values, and are typically in the range of 5 – 9. It should thus be expected that reservoir pH will not affect a CNC-LS dispersion. A very acidic or basic environment would probably destabilise the dispersions.
- **Temperature tolerance:** For the temperature-dependent experiments, nothing definite could be concluded from the Zetasizer measurements. The zeta potential values acquired showed that the dispersions were stable for all the temperatures investigated.

8.1.2 Viscosity

Viscosity measurements confirmed that the viscosity of a CNC dispersion is dependent on CNC concentration and the salinity of the dispersing medium. For the CNC concentrations studied, the dispersed CNC particles had very low effect on the brine viscosity. In the EOR experiments, the CNC particles were thus used as nanoparticles purposed for log-jamming in pore throats and flow diversion.

8.1.3 Effects of heat aging on CNC dispersions

Using CNC particles as additives in injection fluids for reservoirs will expose the dispersions to long-term heat aging processes. The temperature and time stability of CNC-LS dispersions was evaluated. Both the viscosity measurements performed on CNC dispersions heat aged at 120 °C, and the dynamic shear-rest heat aging measurements performed at 90 °C confirmed that dispersions subjected to heat aging would exhibit a large viscosity increase up to a certain time point. Dispersions in LS brine showed the largest temperature-dependent viscosity increase, and became stable even at a concentration as low as 0.5 wt. %. Heat aging of CNC particles increases the surface area of the particles, which again increases the number of interacting

species in the dispersion. This explains the observed increase in viscosity. The viscosity increase with time and temperature might be an important asset for the applicability of CNC for EOR.

The AFM images of heat aged and non-aged CNC-LS samples revealed that the crystallites becomes more dispersed when exposed to heat, although some agglomeration behaviour was observed, and this tendency increases with duration and temperature of heat aging. The AFM images of the heat aged particles also confirms that the CNC does not degrade into glucose monomers but remains crystalline within the time frame and temperatures investigated in this work.

The experiments confirm that a CNC-LS brine dispersion initially build very little dispersion viscosity. This is favourable during fluid injection because a very low increase in pressure build up will be observed in the injection well. As the dispersion propagates into the reservoir, heat aging could increase viscosity and contribute to an improved mobility ratio between oil and water, which is the main approach when using polymers in EOR. Polymer fluids have high viscosities, which dramatically reduces the injectivity, which could be avoided by using an optimised CNC-LS brine dispersion design.

8.2 Core-flooding experiments

8.2.1 Injectivity

Injection of CNC-LS brine dispersions with increasing concentration of CNC (0.5 – 2.0 wt. %) gave effluent viscosities that remained stable and similar to the bulk dispersion throughout the entire flooding experiment, at all the tested concentrations This is confirms the injectivity of the CNC-LS brine dispersion into sandstone cores at relatively low permeabilities. Using reverse flow direction with LS brine confirmed that CNC filtration occurs at the inlet surface of the core, but only minor permanent permeability reduction was observed and a partial restoration of core permeability was achieved after reverse flow with LS brine. The partial permeability reduction, together with the increase in pressure drop when increasing solid content of CNC, may indicate that some of the CNC particles became trapped in the pore matrix.

Effluent pH increased during core flooding, mostly caused by a cation exchange effect with pore surface minerals. The 0.5 wt. % CNC-LS brine exhibited the lowest increase in differential pressure, and it was decided to use this brine concentration for the rest of the flooding experiments.

The injectivity of CNC-LS brines was also investigated at temperatures increasing from 60 to 120 °C, and revealed that the CNC dispersions were injectable at all the tested temperatures. The increase in differential pressure was substantially lower at 90 and 120 °C, compared to the results obtained at 60 °C. The pH of the effluent increased, as expected, but the increase in pH was smallest for the highest temperatures. Rheological measurements confirmed that the viscosity generating CNC particles were able to travel through the core material, although some retention in the pore matrix due to log-jamming in pore throats cannot be excluded. Core regeneration by injecting low saline brine in reversed direction confirmed that most of the retained particles responsible for pressure build up were filtered on the inlet of the core, and that only small changes in core permeability was observed after core regeneration. The observed CNC filtration at the core inlet could be dramatically reduced by paying attention to the size distribution of the CNC particles during the production process.

8.2.2 Enhanced oil recovery experiments

The CNC-LS brine dispersions were used in oil recovery experiments at 60 and 90 °C. The amount of time the particles spent inside the pore system of the core was too short for any temperature dependent viscosity increase to take place. The CNC-LS brine dispersions were used in tertiary mode and the results confirmed that the biopolymer dispersion could affect fluid flow in the pores after a secondary flooding with LS brine. As the CNC dispersion was injected, increased fluctuation in the differential pressure over the core was observed. The mechanism behind the extra oil production observed at 90 °C was most likely linked to log-jamming of CNC particles and agglomerates in pore throats, an effect which could cause water diversion into less available pores. The particles will probably not affect the core wettability any further after the secondary LS brine injection, due to no observed extra pH effect

compared to LS brine, and because the surface charges of the CNC particles and sandstone minerals are the same (anionic).

Combining all observations during the screening of CNC properties and experimental results from using CNC-LS brine dispersions in combination with porous sandstone material, the overall results indicate a potential for using low saline CNC dispersions as a flooding fluid in enhanced oil recovery purposes. CNC particles are relatively salt stable and exhibit good temperature stabilities, and they are injectable into sandstone cores at all tested concentrations and temperatures. They were also able to increase ultimate oil recovery in tertiary mode after LS brine injection.

8.3 Future work

Even though the tests and experiments performed in this work are promising regarding the use of CNC in oil recovery applications, there is a lot more work and investigation that needs to be done.

- **Cationisation:** The CNC material is anionic, due to the acid hydrolysis step during the production process, which leaves negatively charged sulphate half ester groups on the particle surface. This property does not promote particle adsorption onto the clay minerals in the sandstone, as these also are anionic in nature. Surface functionalisation of the CNC to leave the surface with a net positive charge could improve the performance of the nanoparticles for diverted flow purposes.
- **Size optimisation:** The size distribution of the CNC particles should be looked into. Smaller particle sizes and more uniform size distribution could reduce the filtration on the inlet surface of the core and improve injectivity. Ultracentrifugation could be used to separate out the largest particle fractions. Another method to reduce the size (length) of the particles could be to alter the production parameters, either by using higher temperatures, longer acid hydrolysis time**,** as well as stronger acids. Sonication and high pressure homogenisation could be other possible methods.
- **Production process upscaling:** Although it is a bit on the side of the scope of this thesis, an issue that cannot be overlooked is the

production process efficiency. If the material is to be used in the field, vast amounts of material is needed if the injection brine concentration is going to be 0.5 wt. %. In the process described in the methods section, the production yield is 50 %, and the process requires large amounts of water and acid. The process must be optimised to be as efficient and environmentally friendly as possible. Water recycling loops could be used, and a recycling of the acid used should also be looked into to minimalize discharge to the environment. The method is also energy demanding, and the source of this energy should be renewable, e.g. solar, wind or hydroelectric power.

- **Increase water flood temperature:** Due to the increase in viscosity with heat aging, EOR experiments where the earlier observed heat aging effects could be produced would be very interesting to perform. Increased viscosity in the injected fluid can create a stable mobilisation front and thus reduce viscous fingering and divert flow of water in the reservoir. CNC-LS brine dispersions are easily injectable, environmentally friendly and could be a game changer compared to synthetic polymers used as EOR fluids.

References

(ASTM), A. S. f. T. M. (1988). Standard test method for base number of petroleum products by potentiometric perchloric acid titration. *Annual Book of ASTM Standards* (Vol. ASTM D2896-88). West Conshohocken, PA, USA: ASTM International.

(ASTM), A. S. f. T. M. (1989). Standard test method for acid number of petroleum products by potentiometric titration. *Annual Book of ASTM Standards* (Vol. ASTM D664-89). West Conshohocken, PA, USA: ASTM International.

Aadland, R. C., Aurand, K. R., Torsæter, O., Heggset, E. B., & Syverud, K. (2016). INJECTIVITY AND RETENTION OF NANOCELLULOSE DISPERSIONS IN BEREA SANDSTONE.

Abitbol, T., Kloser, E., & Gray, D. (2013). Estimation of the surface sulfur content of cellulose nanocrystals prepared by sulfuric acid hydrolysis. *Cellulose, 20*(2), 785-794. doi:10.1007/s10570-013-9871-0

Ahmed, T. (2010a). Fundamentals of Rock Properties *Reservoir Engineering Handbook (Fourth Edition)* (pp. 189-287). Boston: Gulf Professional Publishing.

Ahmed, T. (2010b). Oil Recovery Mechanisms and the Material Balance Equation *Reservoir Engineering Handbook (Fourth Edition)* (pp. 733-809). Boston: Gulf Professional Publishing.

Ahmed, T. (2010c). Principles of Waterflooding *Reservoir Engineering Handbook (Fourth Edition)* (pp. 909-1095). Boston: Gulf Professional Publishing.

Ahmed, T., & McKinney, P. D. (2005). 4 - Performance of Oil Reservoirs *Advanced Reservoir Engineering* (pp. 291-325). Burlington: Gulf Professional Publishing.

Aksulu, H., Håmsø, D., Strand, S., Puntervold, T., & Austad, T. (2012). Evaluation of Low-Salinity Enhanced Oil Recovery Effects in Sandstone: Effects of the Temperature and pH Gradient. *Energy & Fuels, 26*(6), 3497-3503. doi:10.1021/ef300162n

Ali, M. F., Perzanowski, H., Bukhari, A., & Al-Haji, A. A. (1993). Nickel and vanadyl porphyrins in Saudi Arabian crude oils. *Energy and Fuels, 7*, 179-179.

Amott, E. (1959). Observations relating to the wettability of porous rock.

Anderson, W. G. (1986a). Wettability Literature Survey - Part 1: Rock/Oil/Brine Interactions and the Effects of Core Handling on Wettability. *Journal of Petroleum Technology, 38*(10), 1125-1144. doi:10.2118/13932-PA

Anderson, W. G. (1986b). Wettability Literature Survey - Part 2: Wettability Measurement. *Journal of Petroleum Technology, 38*(11), 1246-1262. doi:10.2118/13933-PA

Anderson, W. G. (1987). Wettability Literature Survey - Part 4: Effects of Wettability on Capillary Pressure. *Journal of Petroleum Technology, 39*(10), 1283-1300. doi:10.2118/15271-PA

Araki, J., Wada, M., Kuga, S., & Okano, T. (1998). Flow properties of microcrystalline cellulose suspension prepared by acid treatment of native cellulose. *Colloids and Surfaces A: Physicochemical and Engineering Aspects, 142*(1), 75-82.

Astley, T., Birch, G. G., Drew, M. G., Rodger, P. M., & Wilden, G. R. (1996). Computer modelling studies of the water-structuring properties of carbohydrates and the sweetness response. *Food chemistry, 56*(3), 231-240.

Aurand, K. R., Dahle, G. S., & Torsæter, O. (2014). *Comparison of oil recovery for six nanofluids in Berea sandstone cores.* Paper presented at the International Symposium of the Society of Core Analysts, September.

Austad, T. (2013). Water-based EOR in Carbonates and Sandstones: New Chemical Understanding of the EOR Potential Using" Smart Water". In J. J. Sheng (Ed.), *Enhanced Oil Recovery Field Case Studies* (pp. 301-355). Boston: Gulf Professional Publishing.

Austad, T., & Milter, J. (1997). *Spontaneous imbibition of water into low permeable chalk at different wettabilities using surfactants.* Paper presented at the International Symposium on Oilfield Chemistry.

Austad, T., RezaeiDoust, A., & Puntervold, T. (2010). *Chemical mechanism of low salinity water flooding in sandstone reservoirs.* Paper presented at the SPE improved oil recovery symposium.

Basu, S., & Sharma, M. M. (1996). Measurement of Critical Disjoining Pressure for Dewetting of Solid Surfaces. *Journal of Colloid and Interface Science, 181*(2), 443-455. doi:http://dx.doi.org/10.1006/jcis.1996.0401

Battista, O. A. (1950). Hydrolysis and crystallization of cellulose. *Industrial & Engineering Chemistry, 42*(3), 502-507.

Bavière, M. (1991). *Basic concepts in enhanced oil recovery processes* (Vol. 33): Springer.

Beal, C. (1946). The Viscosity of Air, Water, Natural Gas, Crude Oil and Its Associated Gases at Oil Field Temperatures and Pressures. *Transactions of the AIME 165*(1), 94-115. doi:10.2118/946094-G

Beck-Candanedo, S., Roman, M., & Gray, D. G. (2005). Effect of Reaction Conditions on the Properties and Behavior of Wood Cellulose

Nanocrystal Suspensions. *Biomacromolecules, 6*(2), 1048-1054. doi:10.1021/bm049300p

Beck, S., Bouchard, J., & Berry, R. (2012). Dispersibility in water of dried nanocrystalline cellulose. *Biomacromolecules, 13*(5), 1486-1494.

Bercea, M., & Navard, P. (2000). Shear Dynamics of Aqueous Suspensions of Cellulose Whiskers. *Macromolecules, 33*(16), 6011-6016. doi:10.1021/ma000417p

Bergaya, F., Lagaly, G., & Vayer, M. (2006). Chapter 12.10 Cation and Anion Exchange. In B. K. G. T. Faïza Bergaya & L. Gerhard (Eds.), *Developments in Clay Science* (Vol. Volume 1, pp. 979-1001): Elsevier.

Bolandtaba, S. F., Skauge, A., & Mackay, E. (2009). *Pore scale modelling of linked polymer solution (LPS)–A new EOR process.* Paper presented at the IOR 2009-15th European Symposium on Improved Oil Recovery.

Boluk, Y., Lahiji, R., Zhao, L., & McDermott, M. T. (2011). Suspension viscosities and shape parameter of cellulose nanocrystals (CNC). *Colloids and Surfaces A: Physicochemical and Engineering Aspects, 377*(1–3), 297-303. doi:http://dx.doi.org/10.1016/j.colsurfa.2011.01.003

Brown Jr, R. M., & Saxena, I. M. (2000). Cellulose biosynthesis: A model for understanding the assembly of biopolymers. *Plant Physiology and Biochemistry, 38*(1–2), 57-67. doi:http://dx.doi.org/10.1016/S0981-9428(00)00168-6

Buckley, J., Liu, Y., & Monsterleet, S. (1998). Mechanisms of Wetting Alteration by Crude Oils. *SPE Journal, 3*(01), 54-61.

Butt, H.-J., Graf, K., & Kappl, M. (2006). Contact angle phenomena and wetting *Physics and Chemistry of Interfaces* (2nd ed., pp. 125-152). Weinheim, Germany: Wiley-VCH.

Chapman, D. L. (1913). LI. A contribution to the theory of electrocapillarity. *The London, Edinburgh, and Dublin philosophical magazine and journal of science, 25*(148), 475-481.

Chatzis, I., & Morrow, N. R. (1984). Correlation of capillary number relationships for sandstone. *Society of petroleum engineers journal, 24*(05), 555-562.

Chen, L., Zhu, J., Baez, C., Kitin, P., & Elder, T. (2016). Highly thermal-stable and functional cellulose nanocrystals and nanofibrils produced using fully recyclable organic acids. *Green Chemistry*.

Conway, B., & Dobry-Duclaux, A. (1960). Viscosity of suspensions of electrically charged particles and solutions of polymeric electrolytes. *Rheology: Theory and Applications, 3*.

Craig, F. F. (1971). Basic Water-Oil Flow Properties of Reservoir Rock. In S. o. P. E. o. AIME (Ed.), *The Reservoir Engineering Aspects of Waterflooding* (pp. 12-28). Dallas, TX, USA: Henry L. Doherty Memorial Fund of AIME.

Crundwell, F. (2015). The mechanism of dissolution of the feldspars: Part I. Dissolution at conditions far from equilibrium. *Hydrometallurgy, 151*, 151-162.

Cuiec, L., & Morrow, N. (1991). Interfacial phenomena in petroleum recovery. *Surfactant science series*, 319-375.

Czurda, K. (2006). Clay Liners and Waste Disposal. *Developments in Clay Science, 1*, 693-701.

Darcy, H. (1856). *Les fontaines publiques de la ville de Dijon: exposition et application*: Victor Dalmont.

de Souza Lima, M. M., & Borsali, R. (2004). Rodlike cellulose microcrystals: structure, properties, and applications. *Macromolecular Rapid Communications, 25*(7), 771-787.

de Vries, H. (1951). Rotatory power and other optical properties of certain liquid crystals. *Acta Crystallographica, 4*(3), 219-226.

Derjaguin, B., & Landau, L. (1941). The theory of stability of highly charged lyophobic sols and coalescence of highly charged particles in electrolyte solutions. *Acta Physicochim. URSS, 14*(633-52), 58.

Dolz, M., Jiménez, J., Hernández, M. J., Delegido, J., & Casanovas, A. (2007). Flow and thixotropy of non-contaminating oil drilling fluids formulated with bentonite and sodium carboxymethyl cellulose. *Journal of Petroleum Science and Engineering, 57*(3–4), 294-302. doi:http://dx.doi.org/10.1016/j.petrol.2006.10.008

Dong, X., Revol, J.-F., & Gray, D. (1998). Effect of microcrystallite preparation conditions on the formation of colloid crystals of cellulose. *Cellulose, 5*(1), 19-32. doi:10.1023/a:1009260511939

Dong, X. M., Kimura, T., Revol, J.-F., & Gray, D. G. (1996). Effects of ionic strength on the isotropic-chiral nematic phase transition of suspensions of cellulose crystallites. *Langmuir, 12*(8), 2076-2082. Retrieved from http://pubs.acs.org/doi/pdfplus/10.1021/la950133b

Dott Jr, R. H. (1964). Wacke, Graywacke and Matrix--What Approach to Immature Sandstone Classification? *Journal of Sedimentary Research, 34*(3).

Drummond, C., & Israelachvili, J. (2002). Surface forces and wettability. *Journal of Petroleum Science and Engineering, 33*(1), 123-133.

Dufresne, A. (2013a). Cellulose and potential reinforcement *Nanocellulose: From nature to high performance tailored materials* (pp. 1-35). Berlin: Walter de Gruyter.

Dufresne, A. (2013b). Preparation of cellulose nanocrystals *Nanocellulose: From nature to high performance tailored materials* (pp. 83-118): Walter de Gruyter.

Dunlop, A. (1948). Furfural formation and behavior. *Industrial & Engineering Chemistry, 40*(2), 204-209.

Eastman, J. (2010). Colloid Stability. In T. Cosgrove (Ed.), *Colloid Science: Principles, Methods and Applications* (pp. 36-49). Bristol, UK: John Wiley & Sons.

Ernest, L., James, J., Moran, D., & Robert, D. (1959). Measurement problems in the instrument and laboratory apparatus fields. *Systems of Units, National and International Aspects, American association for the advancement of science*.

Fan, T., & Buckley, J. S. (2006). *Acid number measurements revisited.* Paper presented at the SPE/DOE Symposium on Improved Oil Recovery.

French, A. D., Miller, D. P., & Aabloo, A. (1993). Miniature crystal models of cellulose polymorphs and other carbohydrates. *International Journal of Biological Macromolecules, 15*(1), 30-36.

Gary, J. H., Handwerk, G. E., & Kaiser, M. J. (2007). *Petroleum refining: Technology and Economics*: CRC press.

Gouy, M. (1910). Sur la constitution de la charge électrique à la surface d'un électrolyte. *J. Phys. Theor. Appl., 9*(1), 457-468.

Green, D. W., & Willhite, G. P. (1998a). *Enhanced Oil Recovery* (4th ed.): Henry L. Doherty Memorial Fund of AIME, Society of Petroleum Engineers.

Green, D. W., & Willhite, G. P. (1998b). Introduction to EOR Processes *Enhanced Oil Recovery* (4th ed., pp. 1-11). Richardson, TX, USA: Henry L. Doherty Memorial Fund of AIME, Society of Petroleum Engineers.

Green, D. W., & Willhite, G. P. (1998c). Macroscopic Displacement of Fluids in a Reservoir. In F. Poettmann & F. Stalkup (Eds.), *Enhanced Oil Recovery* (4th ed., pp. 79-99). Richardson, TX, USA: Henry L. Doherty Memorial Fund of AIME, Society of Petroleum Engineers.

Green, D. W., & Willhite, G. P. (1998d). Microscopic Displacement of Fluids in a Reservoir. In F. Poettmann & F. Stalkup (Eds.), *Enhanced Oil Recovery* (4th ed., pp. 12-35). Richardson, TX, USA: Henry L. Doherty Memorial Fund of AIME, Society of Petroleum Engineers.

Hanaor, D., Michelazzi, M., Leonelli, C., & Sorrell, C. C. (2012). The effects of carboxylic acids on the aqueous dispersion and electrophoretic deposition of ZrO 2. *Journal of the European Ceramic Society, 32*(1), 235-244.

Heggset, E. B., Chinga-Carrasco, G., & Syverud, K. (2017). Temperature stability of nanocellulose dispersions. *Carbohydrate Polymers, 157*, 114-121. doi:http://dx.doi.org/10.1016/j.carbpol.2016.09.077

Hirasaki, G. (1991). Wettability: fundamentals and surface forces. *SPE Formation Evaluation, 6*(02), 217-226.

Hu, Z., Azmi, S. M., Raza, G., Glover, P. W. J., & Wen, D. (2016). Nanoparticle-Assisted Water-Flooding in Berea Sandstones. *Energy & Fuels*. doi:10.1021/acs.energyfuels.6b00051

Hunter, R. J. (1981). Electroviscous and Viscoelectric Effects. In R. H. Ottewill & R. L. Rowell (Eds.), *Zeta Potential in Colloid Science: Principles and Applications* (pp. 179-218). London: Academic Press.

Israelachvili, J. N. (2011). Electrostatic Forces Between Surfaces in Liquids *Intermolecular and Surface Forces* (3rd ed., pp. 291-340): Academic Press.

Israelachvili, J. N., & McGuiggan, P. M. (1988). Forces between surfaces in liquids. *Science, 241*(4867), 795.

Jaafar, M., Nasir, A. M., & Hamid, M. (2014). Measurement of Isoelectric Point of Sandstone and Carbonate Rock for Monitoring Water Encroachment. *Journal of Applied Sciences, 14*(23), 3349-3353.

Jahn, F., Cook, M., & Graham, M. (2008a). Exploration *Hydrocarbon Exploration and Production* (2nd ed., pp. 21-22). Amsterdam: Elsevier.

Jahn, F., Cook, M., & Graham, M. (2008b). The Field Life Cycle *Hydrocarbon Exploration and Production* (2nd ed., pp. 1-6). Amsterdam: Elsevier.

Jahn, F., Cook, M., & Graham, M. (2008c). Reservoir Description *Hydrocarbon Exploration and Production* (2nd ed., pp. 95-171). Amsterdam: Elsevier.

Ju, B., Fan, T., & Ma, M. (2006). Enhanced oil recovery by flooding with hydrophilic nanoparticles. *China Particuology, 4*(01), 41-46.

Julien, S., Chornet, E., & Overend, R. P. (1993). Influence of acid pretreatment (H2SO4, HCl, HNO3) on reaction selectivity in the vacuum pyrolysis of cellulose. *Journal of Analytical and Applied Pyrolysis, 27*(1), 25-43. doi:http://dx.doi.org/10.1016/0165-2370(93)80020-Z

Kjøniksen, A.-L., Beheshti, N., Kotlar, H. K., Zhu, K., & Nyström, B. (2008). Modified polysaccharides for use in enhanced oil recovery applications. *European Polymer Journal, 44*(4), 959-967.

Klemm, D., Heublein, B., Fink, H. P., & Bohn, A. (2005). Cellulose: fascinating biopolymer and sustainable raw material. *Angewandte Chemie International Edition, 44*(22), 3358-3393.

Klemm, D., Kramer, F., Moritz, S., Lindström, T., Ankerfors, M., Gray, D., & Dorris, A. (2011). Nanocelluloses: A New Family of Nature-Based Materials. *Angewandte Chemie International Edition, 50*(24), 5438-5466. doi:10.1002/anie.201001273

Kopp, V. I., Fan, B., Vithana, H. K. M., & Genack, A. Z. (1998). Low-threshold lasing at the edge of a photonic stop band in cholesteric liquid crystals. *Optics Letters, 23*(21), 1707-1709. doi:10.1364/OL.23.001707

Lager, A., Webb, K. J., & Black, C. J. J. (2007). *Impact of brine chemistry on oil recovery*. Paper presented at the IOR 2007-14th European Symposium on Improved Oil Recovery.

Lahiji, R. R., Xu, X., Reifenberger, R., Raman, A., Rudie, A., & Moon, R. J. (2010). Atomic Force Microscopy Characterization of Cellulose Nanocrystals. *Langmuir, 26*(6), 4480-4488. doi:10.1021/la903111j

Leong, Y., & Ong, B. (2003). Critical zeta potential and the Hamaker constant of oxides in water. *Powder Technology, 134*(3), 249-254. Retrieved from http://ac.els-cdn.com/S0032591003002432/1-s2.0-S0032591003002432-main.pdf?_tid=afae66ec-8b03-11e6-8f5c-00000aab0f01&acdnat=1475676043_834735e07e8225ab1aa692e5cd33ed98

Li, S., Hendraningrat, L., & Torsaeter, O. (2013). *Improved Oil Recovery by Hydrophilic Silica Nanoparticles Suspension: 2 Phase Flow Experimental Studies.* Paper presented at the IPTC 2013: International Petroleum Technology Conference.

Li, S., & Torsaeter, O. (2015). *The impact of nanoparticles adsorption and transport on wettability alteration of intermediate wet berea sandstone.* Paper presented at the SPE Middle East Unconventional Resources Conference and Exhibition.

Li, S., & Torsæter, O. (2014). *An experimental investigation of EOR mechanisms for nanoparticles fluid in glass micromodel.* Paper presented at the Paper SCA2014-022 was prepared for presentation at the International Symposium of the Society of Core Analysts held in Avignon, France.

Liao, C.-H., Kang, S.-F., & Wu, F.-A. (2001). Hydroxyl radical scavenging role of chloride and bicarbonate ions in the H2O2/UV process. *Chemosphere, 44*(5), 1193-1200. doi:http://dx.doi.org/10.1016/S0045-6535(00)00278-2

Ligthelm, D. J., Gronsveld, J., Hofman, J., Brussee, N., Marcelis, F., & van der Linde, H. (2009). *Novel Waterflooding Strategy By Manipulation Of Injection Brine Composition.* Paper presented at the EUROPEC/EAGE Conference and Exhibition.

Łojewska, J., Missori, M., Lubańska, A., Grimaldi, P., Zięba, K., Proniewicz, L., & Castellano, A. C. (2007). Carbonyl groups development on degraded cellulose. Correlation between spectroscopic and chemical results. *Applied Physics A, 89*(4), 883-887.

Lu, M.-C., Chang, Y.-F., Chen, I. M., & Huang, Y.-Y. (2005). Effect of chloride ions on the oxidation of aniline by Fenton's reagent. *Journal of Environmental Management, 75*(2), 177-182. doi:http://dx.doi.org/10.1016/j.jenvman.2004.12.003

Mahto, V., & Sharma, V. (2004). Rheological study of a water based oil well drilling fluid. *Journal of Petroleum Science and Engineering, 45*(1), 123-128.

Marchessault, R., Morehead, F., & Koch, M. J. (1961). Some hydrodynamic properties of neutral suspensions of cellulose crystallites as related to size and shape. *Journal of Colloid Science, 16*(4), 327-344.

Marchessault, R., Morehead, F., & Walter, N. (1959). Liquid crystal systems from fibrillar polysaccharides. *Nature, 184*(4686), 632-633.

Matsuo, M., Umemura, K., & Kawai, S. (2012). Kinetic analysis of color changes in cellulose during heat treatment. *Journal of wood science, 58*(2), 113-119.

McGuire, P., Chatham, J., Paskvan, F., Sommer, D., & Carini, F. (2005). *Low salinity oil recovery: An exciting new EOR opportunity for Alaska's North Slope.* Paper presented at the SPE Western Regional Meeting.

Molnes, S., Paso, K., Strand, S., & Syverud, K. (2017). *The effects of pH, time and temperature on the stability and viscosity of a cellulose nanocrystal (CNC) dispersions – Implications for use in enhanced oil recovery*. Unpublished journal article. University of Stavanger.

Molnes, S., Torrijos, I. P., Strand, S., Paso, K. G., & Syverud, K. (2016). Sandstone injectivity and salt stability of cellulose nanocrystals (CNC) dispersions—Premises for use of CNC in enhanced oil recovery. *Industrial Crops and Products, 93*, 152-160. doi:http://dx.doi.org/10.1016/j.indcrop.2016.03.019

Morrow, N., & Buckley, J. (2011). Improved Oil Recovery by Low - Salinity Waterflooding. *Journal of Petroleum Technology, 63*(5), 106-112. doi:10.2118/129421-JPT

Morrow, N. R. (1990). Wettability and its effect on oil recovery. *Journal of Petroleum Technology, 42*(12), 1,476-471,484.

Morrow, N. R., Tang, G.-q., Valat, M., & Xie, X. (1998). Prospects of improved oil recovery related to wettability and brine composition. *Journal of Petroleum Science and Engineering, 20*(3), 267-276.

Muggeridge, A., Cockin, A., Webb, K., Frampton, H., Collins, I., Moulds, T., & Salino, P. (2014). Recovery rates, enhanced oil recovery and

technological limits. *Philosophical Transactions of the Royal Society A: Mathematical, Physical and Engineering Sciences, 372*(2006). doi:10.1098/rsta.2012.0320

Nelson, P. H. (2009). Pore-throat sizes in sandstones, tight sandstones, and shales. *AAPG bulletin, 93*(3), 329-340.

Nichols, G. (2009). Terrigenous Clastic Sediments: Gravel, Sand and Mud *Sedimentology and Stratigraphy* (2nd ed., pp. 5-27). West Sussex, UK: Wiley-Blackwell.

Nickerson, R., & Habrle, J. (1947). Cellulose intercrystalline structure. *Industrial & Engineering Chemistry, 39*(11), 1507-1512.

Ninham, B. (1999). On progress in forces since the DLVO theory. *Advances in Colloid and Interface Science, 83*(1), 1-17.

Onogi, S., & Asada, T. (1980). Rheology and rheo-optics of polymer liquid crystals *Rheology* (pp. 127-147): Springer.

Orts, W., Godbout, L., Marchessault, R., & Revol, J.-F. (1998). Enhanced ordering of liquid crystalline suspensions of cellulose microfibrils: A small angle neutron scattering study. *Macromolecules, 31*(17), 5717-5725.

OSPAR. (2016). OSPAR List of Substances Used and Discharged Offshore which Are Considered to Pose Little or No Risk to the Environment (PLONOR) – Update 2016. Retrieved from http://www.ospar.org/work-areas/oic/chemicals

Payen, A. (1838). Mémoire sur la composition du tissu propre des plantes et du ligneux. *Comptes rendus, 7*, 1052-1056.

Petroleum Resources: Norwegian Continental Shelf. (1993). Stavanger.

Pettijohn, F. (1975). *Sedimentary Rocks*. New York: Harper & Row Ltd.

Pettijohn, F., Potter, P. E., & Siever, R. (1987). *Sand and Sandstone*: Springer Science & Business Media.

Piñerez Torrijos, I. D., Puntervold, T., Strand, S., Austad, T., Abdullah, H. I., & Olsen, K. (2016). Experimental Study of the Response Time of the Low-Salinity Enhanced Oil Recovery Effect during Secondary and Tertiary Low-Salinity Waterflooding. *Energy & Fuels, 30*(6), 4733-4739. doi:10.1021/acs.energyfuels.6b00641

Rae, P., & Johnston, N. (1996). Storable liquid cementitious slurries for cementing oil and gas wells: Google Patents.

Ravikiran, Y. T., Kotresh, S., Vijayakumari, S. C., & Thomas, S. (2014). Liquid petroleum gas sensing performance of polyaniline-carboxymethyl cellulose composite at room temperature. *Current Applied Physics, 14*(7), 960-964. doi:http://dx.doi.org/10.1016/j.cap.2014.04.015

Reiner, R. S., & Rudie, A. W. (2013). Process Scale-Up of Cellulose Nanocrystal Production to 25 kg per Batch at the Forest Products Laboratory. In M. T. Postek, R. J. Moon, A. W. Rudie, & M. A. Bilodeau (Eds.), *Production and Applications of Cellulose Nanomaterials* (pp. 21-24). Peachtree Corners, GA, USA: TAPPI Press.

Revol, J.-F., Bradford, H., Giasson, J., Marchessault, R., & Gray, D. (1992). Helicoidal self-ordering of cellulose microfibrils in aqueous suspension. *International Journal of Biological Macromolecules, 14*(3), 170-172.

Revol, J.-F., Godbout, L., Dong, X.-M., Gray, D. G., Chanzy, H., & Maret, G. (1994). Chiral nematic suspensions of cellulose crystallites; phase separation and magnetic field orientation. *Liquid Crystals, 16*(1), 127-134.

RezaeiDoust, A. (2011). *Low Salinity Water Flooding in Sandstone Reservoirs: A Chemical Wettability Alteration Mechanism.* (Ph.D.), University of Stavanger, Stavanger.

RezaeiDoust, A., Puntervold, T., & Austad, T. (2011). Chemical Verification of the EOR Mechanism by Using Low Saline/Smart Water in Sandstone. *Energy & Fuels, 25*(5), 2151-2162. doi:10.1021/ef200215y

Riley, J. (2010). Charge in Colloidal Systems. In T. Cosgrove (Ed.), *Colloid Science: Principles, Methods and Applications* (pp. 14-35). Bristol, UK: John Wiley & Sons.

Rincon-Torres, M. T., & Hall, L. J. (2015). Cellulose nanowhiskers in well services: Google Patents.

Robinson, H. W. (1929). The influence of neutral salts on the pH of phosphate buffer mixtures. *Journal of Biological Chemistry, 82*(3), 775-802.

Roman, M., & Winter, W. T. (2004). Effect of Sulfate Groups from Sulfuric Acid Hydrolysis on the Thermal Degradation Behavior of Bacterial Cellulose. *Biomacromolecules, 5*(5), 1671-1677. doi:10.1021/bm034519+

Russel, W. B. (1978). The rheology of suspensions of charged rigid spheres. *Journal of Fluid Mechanics, 85*(02), 209-232.

Rånby, B. G. (1949). Aqueous colloidal solutions of cellulose micelles. *Acta Chemica Scandinavia, 3*(5), 649-650. doi:DOI number: 10.3891/acta.chem.scand.03-0649

Rånby, B. G. (1951). Fibrous macromolecular systems. Cellulose and muscle. The colloidal properties of cellulose micelles. *Discussions of the Faraday Society, 11*, 158-164.

Rånby, B. G. (1952). The cellulose micelles. *Tappi, 35*(2), 53-58.

Sacui, I. A., Nieuwendaal, R. C., Burnett, D. J., Stranick, S. J., Jorfi, M., Weder, C., . . . Gilman, J. W. (2014). Comparison of the properties of cellulose nanocrystals and cellulose nanofibrils isolated from bacteria, tunicate, and wood processed using acid, enzymatic, mechanical, and oxidative methods. *ACS applied materials & interfaces, 6*(9), 6127-6138.

Salopek, B., Krasić, D., & Filipović, S. (1992). *Measurement and application of zeta-potential*: Rudarsko-geološko-naftni fakultet.

Sarkar, P., & Nicholson, P. S. (1996). Electrophoretic deposition (EPD): mechanisms, kinetics, and application to ceramics. *Journal of the American Ceramic Society, 79*(8), 1987-2002.

Selley, R. C., & Morill, D. C. (Writers). (1991). GL 101: Basic Concepts of Petroleum Geology. Boston: IHRDC Video Library for Exploration and Production Specialists.

Shafiei Sabet, S. (2013). Shear rheology of cellulose nanocrystal (CNC) aqueous suspensions.

Shi, L., Olsson, M. H. M., Hassenkam, T., & Stipp, S. L. S. (2016). A pH-Resolved View of the Low Salinity Effect in Sandstone Reservoirs. *Energy & Fuels, 30*(7), 5346-5354.

Sjöström, E. (1981). *Wood chemistry: Fundamentals and applications*. New York: Academic Press, Inc.

Skauge, A. (2008). *Microscopic diversion-A new EOR technique.* Paper presented at the The 29th IEA Workshop & Symposium, Beijing, China.

Skauge, T., Spildo, K., & Skauge, A. (2010). *Nano-sized particles for EOR.* Paper presented at the SPE Improved Oil Recovery Symposium.

Skinner, B. J., Porter, S. C., & Park, J. (2013). *Dynamic Earth: An Introduction to Physical Geology* (5th ed.). Hoboken: Wiley.

Smoluchowski, M. v. (1903). Contribution to the theory of electro-osmosis and related phenomena. *Bull Int Acad Sci Cracovie, 3*, 184-199.

Song, K., Wu, Q., Li, M.-C., Wojtanowicz, A. K., Dong, L., Zhang, X., . . . Lei, T. (2016). Performance of low solid bentonite drilling fluids modified by cellulose nanoparticles. *Journal of Natural Gas Science and Engineering, 34*, 1403-1411.

Speight, J. G. (2014). *The Chemistry and Technology of Petroleum*: CRC Press.

Springer, N., Korsbech, U., & Aage, H. (2003). *Resistivity index measurement without the porous plate: A desaturation technique based on evaporation produces uniform water saturation profiles and more reliable results for tight North Sea chalk.* Paper presented at the

Proceedings of the International Symposium of the Society of Core Analysts.

Standnes, D. C., & Austad, T. (2000). Wettability alteration in chalk: 1. Preparation of core material and oil properties. *Journal of Petroleum Science and Engineering, 28*(3), 111-121.

Standnes, D. C., & Austad, T. (2003). Wettability alteration in carbonates: Interaction between cationic surfactant and carboxylates as a key factor in wettability alteration from oil-wet to water-wet conditions. *Colloids and Surfaces A: Physicochemical and Engineering Aspects, 216*(1), 243-259.

Stern, O. (1924). The theory of the electrolytic double-layer. *Z. Elektrochem, 30*(508), 1014-1020.

Stosur, G. J., Hite, J. R., Carnahan, N. F., & Miller, K. *The Alphabet Soup of IOR, EOR and AOR: Effective Communication Requires a Definition of Terms*. https://www.onepetro.org:443/download/conference-paper/SPE-84908-MS?id=conference-paper%2FSPE-84908-MS

Strand, S., Puntervold, T., & Austad, T. (2016). Water based EOR from clastic oil reservoirs by wettability alteration: A review of chemical aspects. *Journal of Petroleum Science and Engineering, 146*, 1079-1091.

Strand, S., Standnes, D. C., & Austad, T. (2003). Spontaneous imbibition of aqueous surfactant solutions into neutral to oil-wet carbonate cores: Effects of brine salinity and composition. *Energy & Fuels, 17*(5), 1133-1144.

Suleimanov, B., Ismailov, F., & Veliyev, E. (2011). Nanofluid for enhanced oil recovery. *Journal of Petroleum Science and Engineering, 78*(2), 431-437.

Sun, C. C. (2005). True density of microcrystalline cellulose. *Journal of pharmaceutical sciences, 94*(10), 2132-2134. Retrieved from http://ac.els-cdn.com/S0022354916318676/1-s2.0-S0022354916318676-main.pdf?_tid=ae42feea-f64c-11e5-9818-00000aab0f01&acdnat=1459324670_afdc617f94a5f30bb06bd3e20030fed1

Tang, G.-Q., & Morrow, N. R. (1999a). Influence of brine composition and fines migration on crude oil/brine/rock interactions and oil recovery. *Journal of Petroleum Science and Engineering, 24*(2), 99-111.

Tang, G.-q., & Morrow, N. R. (1999b). Oil recovery by waterflooding and imbibition—invading brine cation valency and salinity. *Paper SCA9911*.

Technical Manual for Drilling, Completion and Workover Fluids. (1982). International Drilling Fluids.

Terry, R. E. (2001). Enhanced Oil Recovery. In R. A. Meyers (Ed.), *Encyclopedia of physical science and technology* (3rd ed., Vol. 18, pp. 503-518). Tarzana, CA, USA: Academic Press.

Thomas, S. (2008). Enhanced Oil Recovery - An Overview. *Oil & Gas Science and Technology - Revue de l'IFP, 63*(1), 9-19.

Tucker, M. E. (2013). *Sedimentary Petrology: An Introduction to the Origin of Sedimentary Rocks*: John Wiley & Sons.

Udden, J. A. (1914). Mechanical composition of clastic sediments. *Geological Society of America Bulletin, 25*(1), 655-744.

Velde, B., & Meunier, A. (2008). The Origin of Clay Minerals in Soils and Weathered Rocks. *The Origin of Clay Minerals in Soils and Weathered Rocks, by B. Velde and A. Meunier. Berlin: Springer, 2008. ISBN: 978-3-540-75633-0*.

Verwey, E., & Overbeek, J. T. G. (1955). Theory of the stability of lyophobic colloids. *Journal of Colloid Science, 10*(2), 224-225.

Wang, N., Ding, E., & Cheng, R. (2007). Thermal degradation behaviors of spherical cellulose nanocrystals with sulfate groups. *Polymer, 48*(12), 3486-3493. doi:http://dx.doi.org/10.1016/j.polymer.2007.03.062

Wang, S. C., & Wei, W. C. J. (2001). Electrokinetic properties of nanosized SiC particles in highly concentrated electrolyte solutions. *Journal of the American Ceramic Society, 84*(7), 1411-1414.

Webb, K. J., Black, C. J. J., & Edmonds, I. J. (2005). *Low salinity oil recovery–The role of reservoir condition corefloods.* Paper presented at the IOR 2005-13th European Symposium on Improved Oil Recovery.

Webb, K. J., Black, C. J. J., & Tjetland, G. (2005). *A laboratory study investigating methods for improving oil recovery in carbonates.* Paper presented at the International Petroleum Technology Conference.

Wei, B., Li, Q., Jin, F., Li, H., & Wang, C. (2016). The Potential of a Novel Nanofluid in Enhancing Oil Recovery. *Energy & Fuels, 30*(4), 2882-2891.

Wellington, S. L. (1983). Biopolymer solution viscosity stabilization-polymer degradation and antioxidant use. *Society of petroleum engineers journal, 23*(06), 901-912.

Wentworth, C. K. (1922). A scale of grade and class terms for clastic sediments. *The Journal of Geology, 30*(5), 377-392.

Wever, D. A. Z., Picchioni, F., & Broekhuis, A. A. (2011). Polymers for enhanced oil recovery: A paradigm for structure–property relationship in aqueous solution. *Progress in Polymer Science, 36*(11), 1558-1628. doi:http://dx.doi.org/10.1016/j.progpolymsci.2011.05.006

Wierenga, A. M., & Philipse, A. P. (1997). Low-shear viscosities of (semi-) dilute, aqueous dispersions of charged boehmite rods: dynamic scaling of double layer effects. *Langmuir, 13*(17), 4574-4582.

Will, J., Hruschka, M. K., Gubler, L., & Gauckler, L. J. (2001). Electrophoretic deposition of zirconia on porous anodic substrates. *Journal of the American Ceramic Society, 84*(2), 328-332.

Willstätter, R., & Zechmeister, L. (1913). Zur kenntnis der hydrolyse von cellulose I. *Berichte der deutschen chemischen Gesellschaft, 46*(2), 2401-2412.

Wintershall. (2017). The "Life Cycle" of Oil and Gas Fields. Retrieved from https://www.wintershall.com/company/about-us/value-chain.html

Wise, L., Murphy, M., & d'Addieco, A. (1946). Chlorite holocellulose, its fractionation and bearing on summative wood analysis and on studies on hemicelluloses. *Paper Trade J., 122*(2), 35-43.

Worden, R. H., & Morad, S. (2003). *Clay mineral cements in sandstones*: Blackwell Pub.

Yatagai, M., & Zeronian, S. (1994). Effect of ultraviolet light and heat on the properties of cotton cellulose. *Cellulose, 1*(3), 205-214.

Yong, R. N., Nakano, M., & Pusch, R. (2012). Nature of Soils *Environmental Soil Properties and Behaviour* (pp. 25-79). Boca Raton, Fla, USA: CRC Press.

Zhang, Y., & Morrow, N. R. (2006). *Comparison of secondary and tertiary recovery with change in injection brine composition for crude-oil/sandstone combinations.* Paper presented at the SPE/DOE Symposium on Improved Oil Recovery.

Zhang, Y., Xie, X., & Morrow, N. R. (2007). *Waterflood performance by injection of brine with different salinity for reservoir cores.* Paper presented at the SPE Annual Technical Conference and Exhibition.

Zhong, L., Fu, S., Peng, X., Zhan, H., & Sun, R. (2012). Colloidal stability of negatively charged cellulose nanocrystalline in aqueous systems. *Carbohydrate Polymers, 90*(1), 644-649. Retrieved from http://ac.els-cdn.com/S0144861712005504/1-s2.0-S0144861712005504-main.pdf?_tid=d3e3feb0-096f-11e7-ac64-00000aacb35e&acdnat=1489576336_c4e87273f5bff5b682a551633cf89293

Zolotukhin, A. B., & Ursin, J.-R. (2000a). Basic Concepts of Petroleum Geology *Introduction to Petroleum Reservoir Engineering* (pp. 17-29). Kristiansand: Høyskoleforlaget (Norwegian Academic Press).

Zolotukhin, A. B., & Ursin, J.-R. (2000b). Classification of EOR Methods *Introduction to Petroleum Reservoir Engineering* (pp. 299-305). Kristiansand: Norwegian Academic Press (HøyskoleForlaget).

Zolotukhin, A. B., & Ursin, J.-R. (2000c). Permeability *Introduction to Petroleum Reservoir Engineering* (pp. 63-82). Kristiansand: Norwegian Academic Press (HøyskoleForlaget).

Zolotukhin, A. B., & Ursin, J.-R. (2000d). Wettability and Capillary Pressure *Introduction to Petroleum Reservoir Engineering* (pp. 113-144). Kristiansand: Høyskoleforlaget (Norwegian Academic Press).

Åm, K., Al-Kasim, F., Bjerkedal, N., Gjerdseth, A., Kindem, S., Skauge, A., . . . Wiborg, R. (2010). Økt utvinning på norsk kontinentalsokkel. *Oslo: Olje-og Energidepartmentet*.

Appendix

A.1 Calculation of desired core weight at S_{wi} = 20 %

Below are the calculations used to estimate the desired SM10 core weight at S_{wi} = 20 %, by use of the desiccator technique, for the EOR test at 90 °C.

Densities of the FW and d_5FW brines were measured by using a DMA4500 density meter (Anton Paar, Graz, Austria):

Density FW = 1.066 g/cm^3
Density d_5FW = 1.012 g/cm^3

Weight dry core = 165.67 g
Weight 100 % saturated core (d_5FW) = 182.18 g

First, the pore volume (PV) is calculated:

$$PV = \frac{m_{sat}100\ \% - m_{dry}}{\rho_{d_5FW}} = \frac{182.18\ g - 165.67\ g}{1.012\ g/cm^3}$$

The desired weight (g) after desiccation can then be calculated:

$$\begin{aligned} \text{Core weight } S_{wi}\ 20\ \% &= m_{dry} + \rho_{FW} \times PV \times 0.2 \\ &= 165.67\ g + 1.066\ g/cm^3 \times 16.31\ cm^3 \times 0.2 \\ &= 169.14\ g \end{aligned}$$

The desired SM10 core weight at S_{wi} = 20 % , before crude oil saturation is thus **169.14 g**.

A.2 Calculation of H^+ formed from pH reduction

To calculate the amount of H^+ released from the CNC during pH reduction, the molecular weight of glucose in polymer form is used (anhydroglucose unit, AGU), which equals 162 g/mole.

In the calculations shown here , a 2.0 wt. % CNC dispersion with starting pH at 6.2 and ending pH of 2.0 is used as example.

2.0 wt. % equals 20 g/L. This amount can be used to determine the number of moles AGU in the dispersion:

$$\frac{20 \text{ g/L}}{162 \text{ g/mole}} = 0.124 \text{ moles AGU}$$

The amount of H^+ released when the pH is reduced can be found by rewriting this formula:

$$\text{pH} = - \log \left[H^+ \right]$$

to

$$10^{-2.0} - 10^{-6.2} = 9.999 \times 10^{-3} \ H^+$$

The amount of released H^+ can then be used to calculate the amount of H^+ released per 1000 glucose units:

$$\frac{9.999 \times 10^{-3}}{0.124} = 0.083 \times 1000 = \sim 83 \ H^+ \text{ per 1000 glucose units}$$

Paper I

Sandstone Injectivity and Salt Stability of Cellulose Nanocrystals (CNC) Dispersions - Premises for use of CNC in Enhanced Oil Recovery

Silje N. Molnes, Ivan P. Torrijos, Skule Strand, Kristofer G. Paso, Kristin Syverud

Industrial Crops and Products, 2016. Vol. 93, 152 – 160.

Paper I

Not available in UiS Brage due to copyright

Paper II

The effects of pH, time and temperature on the stability and viscosity of cellulose nanocrystal (CNC) dispersions – Implications for use in enhanced oil recovery

Silje Nedland Molnes, Kristofer G. Paso, Skule Strand, Kristin Syverud

Submitted to Cellulose 03.02.2017

Paper II

Not available in UiS Brage due to copyright

Paper III

Investigation of a new application for cellulose nanocrystals – A study of the enhanced oil recovery potential from sandstone by use of a green additive

Silje Nedland Molnes, Aleksandr Mamonov, Kristofer G. Paso, Skule Strand, Kristin Syverud

Submitted to Cellulose 21.03.2017

Paper III

Not available in UiS Brage due to copyright